Aalto-yliopisto

Université Grenoble Alpes

THÈSE

Pour obtenir le grade de

DOCTEUR DE L'UNIVERSITÉ GRENOBLE ALPES
et de l'AALTO UNIVERSITY

École doctorale : STEP - Sciences de la Terre de l'Environnement et des Planètes
Spécialité : Sciences de la Terre et de l'Environnement
Unité de recherche : UMR 5275 - Institut des Sciences de la Terre

Physique statistique de la rupture par fluage des matériaux hétérogènes

Statistical physics of creep rupture of heterogeneous materials

Présentée par :

Juan Carlos VERANO ESPITIA

Direction de thèse :

Jérôme WEISS DIRECTEUR DE RECHERCHE, CNRS Délégation Alpes	Directeur de thèse
Mikko ALAVA FULL PROFESSOR, Aalto Yliopisto	Co-Directeur de thèse

Rapporteurs :

Ferenc KUN
FULL PROFESSOR, Debreceni Egyetem
Ludovic BERTHIER
DIRECTEUR DE RECHERCHE, CNRS Délégation Paris Centre

Thèse soutenue publiquement le **09/06/2026** , devant le jury composé de :

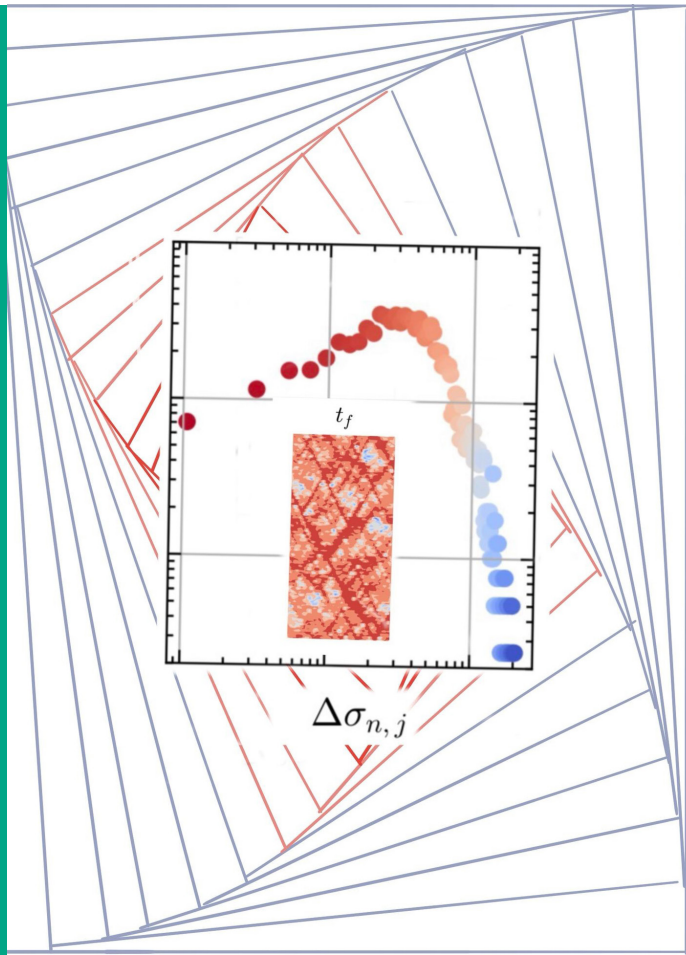
Ludovic BERTHIER DIRECTEUR DE RECHERCHE, CNRS Délégation Paris Centre	Rapporteur et Président du jury
Ferenc KUN FULL PROFESSOR, Debreceni Egyetem	Rapporteur du jury
Jean-Louis BARRAT PROFESSEUR DES UNIVERSITES, Université Grenoble Alpes	Examinateur
Péter Dusán ISPÁNOVITY ASSOCIATE PROFESSOR, Eötvös Lorand Tudomanyegyetem	Examinateur
Jérôme WEISS DIRECTEUR DE RECHERCHE, CNRS Délégation Alpes	Directeur de thèse
Mikko ALAVA FULL PROFESSOR, Aalto Yliopisto	Co-Directeur de thèse

Invités :

Tero MÄKINEN
POSTDOCTORAL RESEARCHER, Aalto Yliopisto

Statistical physics of creep rupture of heterogeneous materials

Juan Carlos Verano Espitia



Aalto University

Aalto University publication series
Doctoral Theses 151/2026

Statistical physics of creep rupture of heterogeneous materials

Juan Carlos Verano Espitia

A doctoral thesis completed for the degree of Doctor of Science (Technology) to be defended, with the permission of the Aalto University School of Science, at a public examination held at the lecture hall A2 (A215) of the school on 09 June 2026 at 11.

This doctoral thesis is conducted under a convention for the joint supervision of thesis at Aalto University (Finland) and Université Grenoble Alpes (France).

Aalto University
School of Science
Department of Applied Physics
Complex Systems and Materials

Université Grenoble Alpes
École doctorale STEP - Sciences de la Terre de l'Environnement et des Planètes
Institut des Sciences de la Terre
Mechanics of Faults and Instabilities

Supervising professor
Professor Mikko J. Alava, Aalto University, Finland
CNRS Research Director Jérôme Weiss, Université Grenoble Alpes, France

Thesis advisors
Dr. Tero Mäkinen, Aalto University, Finland

Preliminary examiners
Professor Ferenc Kun, University of Debrecen, Hungary
Associate Professor Péter Dusán Ispánovity, Eötvös University, Hungary
CNRS Research Director Ludovic Berthier, ESPCI Paris PSL, France

Opponent
Associate Professor Péter Dusán Ispánovity, Eötvös University, Hungary
Professor Jean-Louis Barrat, Université Grenoble Alpes, France (Examiner UGA)

Aalto University publication series
Doctoral Theses 151/2026

© 2026 Juan Carlos Verano Espitia
Image on the cover: Luz Andrea Silva Torres

ISBN 978-952-64-3231-1 (paperback)
ISBN 978-952-64-3230-4 (PDF)
ISSN 1799-4934 (print)
ISSN 1799-4942 (online)

https://urn.fi/URN:ISBN:978-952-64-3230-4

PunaMusta Oy
Helsinki 2026

Aalto-yliopisto

Université Grenoble Alpes

THÈSE

Pour obtenir le grade de

DOCTEUR DE L'UNIVERSITÉ GRENOBLE ALPES
et de l'AALTO UNIVERSITY

École doctorale : STEP - Sciences de la Terre de l'Environnement et des Planètes
Spécialité : Sciences de la Terre et de l'Environnement
Unité de recherche : UMR 5275 - Institut des Sciences de la Terre

Physique statistique de la rupture par fluage des matériaux hétérogènes

Statistical physics of creep rupture of heterogeneous materials

Présentée par :

Juan Carlos VERANO ESPITIA

Direction de thèse :

Jérôme WEISS DIRECTEUR DE RECHERCHE, CNRS Délégation Alpes	Directeur de thèse
Mikko ALAVA FULL PROFESSOR, Aalto Yliopisto	Co-Directeur de thèse
Tero MÄKINEN POSTDOCTORAL RESEARCHER, Aalto Yliopisto	Co-Encadrant de thèse

Rapporteurs :

Ferenc KUN
FULL PROFESSOR, Debreceni Egyetem
Ludovic BERTHIER
DIRECTEUR DE RECHERCHE, CNRS Délégation Paris Centre
Péter Dusán ISPÁNOVITY
ASSOCIATE PROFESSOR, Eötvös Lorand Tudomanyegyetem

Thèse soutenue publiquement le « **09/06/2026** », devant le jury composé de :

Jérôme WEISS DIRECTEUR DE RECHERCHE, CNRS Délégation Alpes	Directeur de thèse
Mikko ALAVA FULL PROFESSOR, Aalto Yliopisto	Directeur de thèse
Ferenc KUN FULL PROFESSOR, Debreceni Egyetem	Rapporteur
Ludovic BERTHIER DIRECTEUR DE RECHERCHE, CNRS Délégation Paris Centre	Rapporteur
Péter Dusán ISPÁNOVITY ASSOCIATE PROFESSOR, Eötvös Lorand Tudomanyegyetem	Examinateur
Jean-Louis BARRAT PROFESSEUR DES UNIVERSITES, Université Grenoble Alpes	Examinateur

Invités :

Tero MÄKINEN POSTDOCTORAL RESEARCHER, Aalto Yliopisto	Co-Encadrant de thèse

Aalto University

Université Grenoble Alpes

ABSTRACT

Author Juan Carlos Verano Espitia

Name of the doctoral thesis Statistical physics of creep rupture of heterogeneous materials

Article-based thesis

Number of pages viii + 146

Keywords creep, statistical physics, heterogeneous material, thermal activation

In this work, the creep behavior of heterogeneous materials, i.e., those subjected to a constant load, is studied using experimental, theoretical, and numerical approaches. Understanding how materials deform, damage, and approach failure is relevant in fields such as materials science, geophysics, and engineering. Nevertheless, in classical mechanics and engineering literature, the so-called "creep" failure is only described using empirical approaches. Such empirical laws are common to most brittle materials, soft materials, ductile metals, and granular media. Therefore, the universality of this phenomenon across a wide range of materials remains an open question, still lacking a full theoretical understanding. Therefore, this project aims (i) to track the progressive damage during creep of heterogeneous brittle materials, e.g. common office paper, using various monitoring tools such as acoustic emission, and (ii) to introduce statistical physics theory and numerical approaches (fiber bundle models, progressive damage model, kinetic Monte Carlo algorithm) to interpret this damage evolution. The final goal is to predict failure in the early stages of creep experiments, leveraging all acquired knowledge, using a Bayesian inference framework. This research has potential applications in material diagnostics and failure prediction, which are highly relevant to civil engineering and risk analysis, as well as to geophysical phenomena such as landslides and rockfalls.

TIIVISTELMÄ

Tekijä Juan Carlos Verano Espitia

Väitöskirjan nimi Heterogeenisten materiaalien virumismurtumisen tilastollinen fysiikka

Artikkeliväitöskirja

Sivumäärä viii + 146

Avainsanat viruminen, tilastollinen fysiikka, heterogeeninen materiaali, terminen aktivointi

Tässä työssä tutkitaan heterogeenisten materiaalien virumiskäytöstä, eli käytöstä vakiokuormituksen alaisena, kokeellisin, teoreettisin ja numeerisin menetelmin. Materiaalien muodonmuutosten, vaurioiden ja murtumien ymmärtäminen on tärkeää esimerkiksi materiaalitieteessä, geofysiikassa ja insinööritieteissä. Klassisessa mekaniikassa ja tekniikan kirjallisuudessa ns. ”virumis”murtumista kuvataan kuitenkin vain empiiristen lähestymistapojen avulla. Tällaiset empiiriset lait ovat yleisiä useimmille hauraille materiaaleille, pehmeille materiaaleille, muovautuville metalleille ja rakeisille materiaaleille. Siksi tämän ilmiön universaalisuus laajassa materiaalijoukossa onkin edelleen avoin kysymys, jolle ei ole täydellistä teoreettista ymmärrystä. Tämän vuoksi tämän projektin tavoitteena on (i) seurata heterogeenisten hauraiden materiaalien, kuten tavallisen toimistopaperin, vaurioitumista virumisen aikana käyttämällä erilaisia seurantavälineitä, kuten akustista emissiota, ja (ii) ottaa käyttöön tilastollisen fysiikan teoria ja numeeriset lähestymistavat (kuitukimppumallit, progressiivinen vaurioitumismalli, kineettinen Monte Carlo -algoritmi) tämän vaurioitumisen kehityksen tulkitsemiseksi. Lopullisena tavoitteena on ennustaa murtuminen virumiskokeiden alkuvaiheessa hyödyntämällä kaikkea hankittua tietoa bayesilaisen päättelyn avulla. Tällä tutkimuksella on potentiaalisia sovelluksia materiaalien diagnostiikassa ja murtumisen ennustamisessa, jotka ovat erittäin merkityksellisiä rakennustekniikassa ja riskianalyysissä sekä geofysikaalisissa ilmiöissä, kuten maanvyörymissä ja kivivyöryissä.

RÉSUMÉ

Auteur Juan Carlos Verano Espitia

Titre de la thèse Physique statistique de la rupture par fluage des matériaux hétérogènes

Thèse sur publications

Nombre de pages viii + 146

Mots clés fluage, physique statistique, matériau hétérogène, activation thermique

Dans ce travail, le comportement au fluage des matériaux hétérogènes, c'est-à-dire ceux soumis à une charge constante, est étudié à l'aide d'approches expérimentales, théoriques et numériques. Comprendre comment les matériaux se déforment, s'endommagent et approchent de la rupture est pertinent dans des domaines tels que la science des matériaux, la géophysique et l'ingénierie. Néanmoins, dans la littérature classique sur la mécanique et l'ingénierie, la rupture dite «par fluage» n'est décrite qu'à partir d'approches empiriques. Ces lois empiriques sont communes à la plupart des matériaux fragiles, des matériaux souples, des métaux ductiles et des milieux granulaires. Par conséquent, l'universalité de ce phénomène pour un large éventail de matériaux reste une question ouverte, qui manque encore d'une compréhension théorique complète. Par conséquent, ce projet vise (i) à suivre les dommages progressifs lors du fluage de matériaux fragiles hétérogènes, par exemple le papier de bureau ordinaire, à l'aide de divers outils de surveillance tels que l'émission acoustique, et (ii) à introduire la théorie de la physique statistique et des approches numériques (modèles de faisceaux de fibres, modèle de dommages progressifs, algorithme cinétique de Monte Carlo) pour interpréter cette évolution des dommages. L'objectif final est de prédire la défaillance dès les premières étapes des expériences de fluage, en tirant parti de toutes les connaissances acquises, à l'aide d'un cadre d'inférence bayésienne. Cette recherche a des applications potentielles dans le domaine du diagnostic des matériaux et de la prédiction des défaillances, qui sont très pertinentes pour le génie civil et l'analyse des risques, ainsi que pour les phénomènes géophysiques tels que les glissements de terrain et les chutes de roches.

Preface

A mis padres, Carlos y Maria Elisa,
con quienes este largo camino comenzó en los años 1960,
entre las montañas de Boyacá y Santander.

This is the final page of my doctoral dissertation, and I would like to thank everyone who has been a part of this journey. A journey that has taken place entirely within public institutions, from elementary school all the way through my doctorate. So I could say that I am a product of the public system. In this thesis, I have attempted to frame all my PhD work within the subject of creep rupture of heterogeneous materials. My work over the past years has tried to bridge the gap between statistical physics, creep phenomenology, and disordered materials. My journey into this unknown field began during my master's studies, when I conducted my research internship with Jérôme Weiss and David Amitrano. From them, I learned some concepts of statistical physics (completely new to me at the time) to explain the physical behavior of brittle materials under constant loads. For me, it was revealing because it combined most of the scientific fields I enjoy: mathematics, physics, probability, numerical modeling, and geophysics.

This work would not have been possible without the guidance of my supervisors, Jérôme Weiss, Mikko Alava, and Tero Mäkinen. Their experience and expertise in fields ranging from applied physics to geophysics provided me with a wide range of approaches for solving scientific problems. I never cease to be amazed by how they always find a reasonable explanation for scientific challenges. I would also like to express my deepest gratitude for their patience in explaining physical concepts to me that were, on many occasions, completely unfamiliar to me. I thank my colleagues from the Fault Mechanics team at ISTerre and the CSM group at Aalto for their enriching discussions and critical feedback. I would like to thank Christian Geindreau, Martin Obligado, and Cino Viggiani for accepting me as a master's student in 2020 at the Université Grenoble Alpes (UGA), despite my having not studied for nearly four years, and for their guidance during my early steps in scientific research. I also thank Mai-Linh Doan, Alberto Rosso, and Lasse

Laurson for serving as examiners on my “Comité de Suivi Individuel” and “Midterm Review”.

I would also like to thank Isaac Miranda and Etienne Niemiec for all their support in navigating the bureaucracy and complexities of the Finnish system (y las conversaciones en español / et pour les discussions en français). I would also like to thank the Monday futsal group; having those moments to clarify and organize my thoughts was very important to me. Beyond my colleagues, I am grateful for the financial and infrastructural support provided by Aalto University, Université Grenoble Alpes, and the Finnish Academy of Science and Letters.

Beyond academia, I want to thank the Latin crew from Grenoble and Helsinki. It was huge, but regarding my time in Grenoble, I’d especially like to thank "las rolitas" (Lau and Sindy) for the time we spent together and all the philosophical discussions, and "las grenobloises" (Estela y mi catalana favorita, Ari) for always coming up with new travel ideas. En Colombia, quisiera agradecer a mis mejores amigos: Cata, Pocho, Juli, Sarita, Dianis, Leidy (Lila) y Jonathan (Pachon). Su amistad ha sido una de las mayores alegrías de mi vida. Además, un gran agradecimiento a la profe Maritzabel en la Universidad Nacional (la Nacho) por creer siempre en que soy capaz de dar más. Y a Yoldana, quien llegó para ser mi guía espiritual para mi cabeza tumultuosa. En mi familia, son muchas las personas que han aportado su ayuda en los momentos más difíciles. Especialmente, quisiera agradecer a Yeimy y a mi tía Dora por estar siempre disponibles para tendernos una mano. Y no puedo olvidar a mi hermana mayor, Sandra, y a mis sobrinas Dana, Lizeth, Isabella y Alisson. Ustedes son el futuro y quiero estar presente cuando triunfen.

Mis profundos agradecimientos van para mis padres y mis hermanos. Su largo trayecto en la vida también es mío y quisiera honrarlo con este trabajo; esto también es el resultado de todo su esfuerzo. A mis hermanos menores, Jimmy, Angélica y Camilo, también les dedico este trabajo, aunque no he estado mucho para ustedes en estos últimos años; ustedes siempre han sido y serán muy importantes para mí y me enorgullece mucho en lo que se han convertido. Finally, I would like to express my heartfelt gratitude to the most important person in my life, my wife, Luz Andrea “Morita”, who has been by my side throughout this journey and has been a vital pillar of support, helping our dreams continue to come true despite the challenges we’ve faced. Tu compañía me hace muy feliz y me alegra que juntos hayamos podido crecer, tanto personalmente como profesionalmente.

Helsinki, May 18, 2026,

Juan Carlos Verano Espitia

Contents

Preface **1**

Contents **3**

Abbreviations **5**

List of Symbols **6**

List of Publications **13**

Author's contributions **15**

List of Figures **17**

List of Tables **23**

1. Introduction **25**
1.1 Motivation and background 25
1.1.1 Creep phenomenology 26
1.1.2 Heterogeneous materials 27
1.1.3 Elastic interaction kernel 28
1.1.4 Thermal activation 29
1.2 Objectives 32
1.3 Thesis outline 32

2. Effect of the local elastic interaction geometry on the creep lifetimes **35**
2.1 A theoretical approximation for the creep lifetime . . . 36
2.1.1 General case 36
2.1.2 Negligible mechanical interaction 37
2.2 Description of the numerical model 38
2.2.1 Athermal model 38
2.2.2 Thermal activation 41
2.3 Numerical results 44

2.3.1 Effective temperature and dependency on the heterogeneity and the elastic interaction geometry 44
2.3.2 Variability of the creep lifetime around its average 47
2.3.3 Implications of the heterogeneity and elastic interaction kernel on the interpretation of macro parameters 49

3. Ranking persistence from a catalog of AE event times 53
3.1 Fiber bundle model with thermal activation 54
3.1.1 Extremal dynamics emerges from thermal activation in the DFBM 54
3.1.2 Model used 55
3.2 Results 56
3.2.1 Cumulative probability distribution and rank persistence of event times 56
3.2.2 Multiplicative random process connected to the tail of the excitation spectrum 59

4. Bayesian inference for early prediction of creep failure times 63
4.1 Bayesian inference model 64
4.1.1 Master curve behavior 64
4.1.2 Acoustic emission correlations 67

5. Conclusions 75

6. Devices and methods 79
6.1 Experimental methods 79
6.1.1 Samples and athermal testing 79
6.1.2 Creep testing 80
6.1.3 Acoustic emission 81
6.2 Thermal activation via a BKL–kMC algorithm 84

References 87

Key terms of the doctoral thesis 97

Publications 99

Abbreviations

AE Acoustic Emission.

BKL Bortz–Kalos–Lebowitz.

CRPS continuous ranked probability score.

DFBM democratic fiber bundle model.

FBM fiber bundle model.

FEM Finite Element Method.

kMC kinetic Monte Carlo.

MC Mohr–Coulomb.

MCMC Markov chain Monte Carlo.

PDM progressive damage model.

List of Symbols

Greek letters

$\Delta\sigma_{n,j}^{\text{tract}}$ traction stress gap

γ Euler–Mascheroni constant

λ scale parameter of the Weibull distribution

π pi number

ρ shape parameter of the Weibull distribution

$\sigma_{\text{tract},n}$ traction stress threshold

β tertiary creep exponent

$\Delta\tau_{j+1}$ duration of the $(j+1)$th AE event, also known as coda length in seismology

Δt_{j+1} waiting time between successive AE events (experiments) or thermal transitions (simulations), $t_{j+1} - t_j$ at transition $j+1$

$\Delta\sigma_{\text{macro}}$ macro stress gap proportional to the difference between the athermal strength and the applied stress

$\Delta\sigma_{n,j}$ local stress gap at transition $j+1$

$\dot{\varepsilon}$ global strain rate in Newton's—or dot—notation for differentiation. Also written as $\mathrm{d}\varepsilon/\mathrm{d}t$

μ internal friction coefficient for geomaterials, e.g., rocks, concrete. $\mu = \tan\phi$

ν Poisson's ratio

Ω_0 thermal vibration frequency

ω_{j+1} global jump rate at transition $j+1$

$\omega_{n,j+1}$ local jump rate at transition $j+1$ for the element n. Probability per unit time that element n will thermally activate during transition $j+1$

Φ orientation of the failure normal surface, based on the Mohr–Coulomb criterion

ϕ internal friction angle for geomaterials, e.g. rocks, concrete

ψ_{j+1} prefactor of the power law emerging from the lognormal distribution and rank persistence of the time series t_{j+1} obtained experimentally (AE event times) and numerically (fiber failure times), relating t_f and t_{j+1}

$\sigma_{\max,j}$ maximum of the local strength at transition $j+1$, constant in the PDM ($C_{\max}$) and variable in the DFBM

$\sigma_{\min,j}$ minimum of the local strength at transition $j+1$, constant in the PDM ($C_{\min}$) and variable in the DFBM

$\sigma_{\parallel,n,j} - \sigma_{\perp,n,j}\mu$ local Coulomb stress for geomaterials computed with the MC criterion during the creep phase. $\sigma_{\parallel,n,j}$ and $\sigma_{\perp,n,j}$ are the shear and the normal stress in the orientation that maximizes the Coulomb stress

$\sigma_{\parallel,n} - \sigma_{\perp,n}\mu$ local Coulomb stress for geomaterials computed with the MC criterion during the athermal phase. $\sigma_{\parallel,n}$ and $\sigma_{\perp,n}$ are the shear and the normal stress in the orientation that maximizes the Coulomb stress

σ_{appl} constant applied stress at macroscale

σ_{ath} strength of the sample or macro stress threshold in athermal conditions

$\sigma_{n,j}^{\text{appl}}$ local stress state (2D) or local applied stress (1D) in the element n at transition $j+1$

σ_n local strength. In the PDM, introduced via the local cohesion C_n

σ_n^{appl} local stress state (2D) or local applied stress (1D) in the element n during the athermal phase

σ_n^{ath} local stress threshold in athermal conditions

τ_{j+1} initial time of the $(j+1)$th AE event

θ_{j+1} exponent of the power law emerging from the lognormal distribution and rank persistence of the time series t_{j+1} obtained experimentally (AE event times) and numerically (fiber failure times), relating t_f and t_{j+1}

ε	global strain
$\varepsilon_n^{\text{appl}}$	local strain at transition $j+1$
$\varepsilon_n^{\text{ath}}$	local strain during athermal phase
ϑ	set of parameters for the Bayesian inference

Latin letters

$\dot{\mathscr{D}}$	global event rate in Newton's—or dot—notation for differentiation. Also written as $\mathrm{d}\mathscr{D}/\mathrm{d}t$
$\mathscr{D}$	global number of accumulated damage events
R_0	prefactor of the random multiplicative process accounting for the sample-to-sample variability among samples, e.g., the strength variability shown by a material with the same geometry and subjected to the same applied force
$\mathbf{x}$	observed data e.g. strain, strain rate or event times
$\mathscr{D}_{n,j}$	local accumulated damage events during creep phase
$\mathscr{D}_n$	local accumulated damage events during athermal load
$\mathscr{N}$	number of thermally activated transitions (simulations) or acoustic emission events (experiments) leading to failure
A	primary creep prefactor
B	tertiary creep prefactor
C_n	local cohesion
D	damage parameter
E	activation energy
$E_{j+1}^{(\text{AE})}$	energy radiated by the $(j+1)$th AE event, defined as the area below the curve of $y(t)^2$ in the time window $(\tau_{j+1}, \tau_{j+1}+\Delta\tau_{j+1})$
$E_{n,j}$	local activation energy at jump rate $j+1$
F_j	free energy barrier at jump rate $j+1$
j	index indicating an AE event / thermally activated transition
k_B	Boltzmann's constant
N	total number of elements (sub-volumes in 3D, sub-areas in 2D, fibers in 1D) forming a solid (or area or fiber bundle)
n	index indicating a sub-volume (local space, element)

p primary creep exponent

S_j entropy, used from the 'lack' of information point of view, i.e., more related to Shannon's entropy. It is a quantifier of the spatial heterogeneity distribution and damage disorder

T temperature

t continuous time

t_f creep failure time

t_j event times obtained from catalog of acoustic emission events or event series in simulations

T_{eff} effective temperature

V true activation volume for the micro damage mechanism

V_{est} activation volume estimated from creep experiments

$y(t)$ amplitude of the AE continuous signal

Y_0 Young's modulus of reference

$Y_{n,0}$ initial local Young's modulus during creep

$Y_{n,j}$ local Young's modulus at transition $j+1$

Y_n local Young's modulus during athermal loading

Z_j partition function at the transition $j+1$

F_{appl} applied constant load

F_{ath} maximum load in athermal conditions, i.e., maximum load a system/-material can handle before failure

Mathematical functions and probability distributions

$\exp(\cdot)$ exponential function. $\exp(1) = e$ is Euler's number

$\ln(\cdot)$ natural logarithm function

$\operatorname{erfc}(\cdot)$ complementary Gaussian error function

$\sinh(\cdot)$ hyperbolic sine function

$H(\cdot)$ Heaviside step function

$\mathscr{L}(\mathbf{x}|\vartheta)$ likelihood distribution

$f(\Delta\sigma_{n_b,j})$ discrete probability distribution of the stress gap at transition $j+1$, also called excitation spectrum. $f(\Delta\sigma_{n,j})$ for a continuous form

$f(\sigma_n)$ probability distribution of local strengths, e.g., Weibull, Gaussian, uniform, etc. Defines the initial quenched disorder. In the PDM, it is fixed and introduced via the local cohesion distribution $f(C_n)$. In the DFBM, it could be variable due to the elimination of fibers, i.e., it becomes the probability distribution of local strengths of the surviving fibers $f(\sigma_{n,j})$

$f(\vartheta|\mathbf{x})$ posterior distribution of the set of parameters ϑ

$f(\vartheta)$ prior distribution of the set of parameters ϑ

$f(E_{n_b,j})$ discrete probability distribution of energy barriers at transition $j+1$. $f(E_{n,j})$ is the representation in a continuous form

$g(E_{n_b,j})$ discrete density of states at transition $j+1$, i.e., number of subvolumes with energy within a small range $(E_{n_b,j}, E_{n_b,j}+dE_{n_b,j})$. $g(E_{n,j})$ is the representation in a continuous form

$p(E_{n,j})$ in statistical physics, the probability of the system to be in an energetic configuration $E_{n,j}$, related to the probability per unit time of an element n to activate during the thermal transition $j+1$

Statistical measures

δR_0 standard deviation of the prefactor of the random multiplicative process

$\langle R_0 \rangle$ average of the prefactor of the random multiplicative process

$\delta(\cdot)$ standard deviation over different experiments of the same material or numerical realizations of the same initial disorder distribution

δC standard deviation of the cohesion distribution

$\delta E_{\Delta\sigma,j}$ standard deviation of the activation energy at transition $j+1$

δt_f standard deviation of the creep failure time

$\delta_{\Delta\sigma,j}$ standard deviation of the stress gap at transition $j+1$

$\langle \cdot \rangle$ average over different experiments of the same material or numerical realizations of the same initial disorder distribution. Spatial average

$\langle \Delta\sigma \rangle_j$ average of the stress gap at transition $j+1$

$\langle C \rangle$ mean value of the cohesion

$\langle E \rangle_j$ internal energy. Average energy weighted by the activation energy probability $p(E_{n,j})$, at transition $j+1$

$\langle E_{\Delta\sigma} \rangle_0$ mean of the activation energy for the first transition

$\langle E_{\Delta\sigma} \rangle_j$ average activation energy at the thermal transition $j+1$

$\langle t_f \rangle$ mean creep failure time

$\langle \Delta t \rangle_{j+1}$ average waiting time between successive AE events (experiments) or thermal transitions (simulations), $t_{j+1} - t_j$ at transition $j+1$

$\overline{(\cdot)}$ time history average. Average over the last j events

List of Publications

This thesis consists of an overview and of the following publications which are referred to in the text by their Roman numerals.

I J.C. Verano-Espitia, J. Weiss, D. Amitrano, T. Mäkinen, M.J. Alava. Effect of quenched heterogeneity on creep lifetimes of disordered materials. *Phys. Rev. E*, 110, 064133, DOI 10.1103/PhysRevE.110.064133, December 2024.

II J.C. Verano-Espitia, T. Mäkinen, M.J. Alava, J. Weiss. Creep failure in heterogeneous materials from the barrier landscape. *Phys. Rev. E*, 112, L063501, DOI 10.1103/xbnt-6csz, December 2025.

III J.C. Verano-Espitia, T. Mäkinen, M.J. Alava, J. Weiss. Early Prediction of Creep Failure via Bayesian Inference of Evolving Barriers. *Under review at Phys. Rev. Lett.*, (Preprint available on arXiv DOI arXiv:2603.16419), March 2026.

Author's contributions

Publication I: "Effect of quenched heterogeneity on creep lifetimes of disordered materials"

Juan C. Verano-Espitia and Jérôme Weiss carried out the investigation. David Amitrano and Jérôme Weiss developed the first version of the numerical model. Juan C. Verano-Espitia performed the computations and validation with input from Tero Mäkinen, David Amitrano, Jérôme Weiss, and Mikko J. Alava. Juan C. Verano-Espitia analyzed the numerical data. Mikko J. Alava and Jérôme Weiss planned and carried out the project administration and funding acquisition. Juan C. Verano-Espitia, Jérôme Weiss, and David Amitrano developed the methodology and formal analysis. Juan C. Verano-Espitia wrote the manuscript with input from all coauthors. Tero Mäkinen, Jérôme Weiss, and Mikko J. Alava provided supervision and validation.

Publication II: "Creep failure in heterogeneous materials from the barrier landscape"

Juan C. Verano-Espitia and Tero Mäkinen carried out the investigation. Juan C. Verano-Espitia and Tero Mäkinen conceived the experiment. Juan C. Verano-Espitia conducted the validation with input from Tero Mäkinen, Jérôme Weiss, and Mikko J. Alava. Juan C. Verano-Espitia analyzed the experimental and numerical data. Jérôme Weiss and Mikko J. Alava planned and carried out the project administration and funding acquisition. Juan C. Verano-Espitia and Tero Mäkinen developed the methodology, conducted the formal analysis, and curated the data. Juan C. Verano-Espitia wrote the manuscript with input from all coauthors. Tero Mäkinen, Jérôme Weiss, and Mikko J. Alava provided supervision and validation.

Publication III: "Early Prediction of Creep Failure via Bayesian Inference of Evolving Barriers"

Juan C. Verano-Espitia and Tero Mäkinen carried out the investigation and conceived the experiment. Tero Mäkinen developed the Bayesian code, and Juan C. Verano-Espitia modified it to address the scientific question. Juan C. Verano-Espitia conducted the validation with input from Tero Mäkinen, Jérôme Weiss, and Mikko J. Alava. Juan C. Verano-Espitia analyzed the experimental and numerical data. Jérôme Weiss and Mikko J. Alava planned and carried out the project administration and funding acquisition. Juan C. Verano-Espitia and Tero Mäkinen developed the methodology, conducted the formal analysis, and curated the data. Tero Mäkinen and Juan C. Verano-Espitia wrote the first draft of the manuscript with input from all coauthors. Tero Mäkinen, Jérôme Weiss, and Mikko J. Alava provided supervision and validation.

List of Figures

1.1 Illustration of typical creep phenomenology with deformation obtained from a tensile creep experiment on a sheet of paper. **a)** creep as a time-dependent deformation (black line) under constant applied load (red line). **b)** Power law decay of the strain rate during primary creep. **c)** Power law acceleration of the strain rate during tertiary creep. 27

2.1 Schematic representation of the limits of zero and infinity disorder for different parameters as a function of the term $\langle E_{\Delta\sigma}\rangle_0/k_BT$. **a)** Correcting term $\overline{\Delta Z_j}$. **b)** Effective temperature T_{eff}/T. **c)** Creep lifetime $\langle t_f\rangle/t_0$. Red dashed line: Homogeneous case $\delta \to 0$, green dashed line: Strongly heterogeneous case $\delta \to \infty$. All intermediate cases of heterogeneity are in the filled blue zone. 37

2.2 Different parameters of the thermally activated progressive damage model: **a)** Gaussian probability distribution of the cohesion for different disorder levels. **b)** Representation of the MC criterion at microscale and the identification of its respective local stress gap $\Delta\sigma_{n,j}$, and identification of an additional traction criterion, $\Delta\sigma_{n,j}^{\text{tract}}$, in cases where $\sigma_{3,n,j} < 0$. **c)** Example of the temporal evolution of the macroscopic axial strain for creep simulations at different disorder levels. Adapted from [1]. 40

2.3 **a)** Example of the evolution of the stress gap field $\Delta\sigma_{n,j}$, and **b)** its respective excitation spectrum $f(\Delta\sigma_{n,j})$ at different stages: initial $t_0 = 0$, end of primary creep $t_{\min} = t(\dot{\varepsilon}_{\min})$, and rupture time t_f. Adapted from [1]. 41

2.4 **a)** Theoretical dependency of the effective temperature T_{eff} on the friction coefficient μ, for different initial quenched disorder values given in terms of the cohesion C_n: homogeneous (red), intermediate (blue), and large disorder (green). **b)** Theoretical dependency of the effective temperature T_{eff} on the initial quenched disorder term $\delta_{\Delta\sigma,0}/\langle\Delta\sigma\rangle_0$, for different friction coefficients: $\mu = 0$ (light blue), $\mu = 0.7$ (blue) and $\mu = 1.0$ (dark blue), where the dashed lines are the approximation for the infinity–disorder limit given by Eq. 2.4. Each case was computed under different applied stress $\sigma_{\text{appl}}/\langle C\rangle$, with $\langle C\rangle = 20$MPa and $T = 300$K. 43

2.5 Influence of the internal friction coefficient, $\mu = \{0.0, 0.7\}$, on the elastic interaction geometry. **a)** and **c)** Cohesion field, set as the same for both cases. Example of the evolution of the stress gap field $\Delta\sigma_{n,j}$ for different friction coefficients: **b)** $\mu = 0.0$ and **b)** $\mu = 0.7$, at different stages: initial $t_0 = 0$, end of primary creep $t_{\text{min}} = t(\dot{\varepsilon}_{\text{min}})$, and rupture time t_f. t_f is given in arbitrary units. 44

2.6 Theoretical (dashed line) vs. numerical (squares, dots) results for t_f/t_0 dependency on the term $V\langle\Delta\sigma\rangle_0/k_BT$, for different values of the stress ratio $\sigma_{\text{appl}}/\sigma_{\text{ath}}$ and friction coefficients **a)** $\mu = 0.0$ (squares) and **b)** $\mu = 0.7$ (dots). The different colors represent homogeneity (red), intermediate heterogeneity (blue), and strong heterogeneity (green). The theoretical curves are obtained with Eq. 2.12. Adapted from [1]. 45

2.7 **a)** Effective temperature ratio T_{eff}/T as a function of the heterogeneity. **b)** Dependency of the lifetime t_f/t_0 on $V_a\langle\Delta\sigma\rangle_0/k_BT_{\text{eff}}$. Squares: $\mu = 0.0$, dots: $\mu = 0.7$. Red: homogeneous, blue: intermediate, green: strongly heterogeneous. Adapted from [1]. 46

2.8 Size cell independence of the creep lifetime t_f. Theoretical (dashed line) vs. numerical (squares, dots) results for t_f/t_0 dependency on the term $V\langle\Delta\sigma\rangle_0/k_BT$, for different values of the stress ratio $\sigma_{\text{appl}}/\sigma_{\text{ath}}$, friction coefficient $\mu = 0.7$ and two different system sizes: **a)** $N = 960$ and **b)** $N = 3968$. The different colors represent homogeneity (red) and strong heterogeneity (green). The theoretical curves are obtained with Eq. 2.12. 48

2.9 Dependence of the standard deviation on the mean failure time. Different realizations of the thermal disorder for **a)** a system with the same initial cohesion field (quenched disorder constant in space, thermal activation variable) and **b)** different variations of the cohesion field from the same initial disorder distribution (quenched disorder variable in space, thermal activation variable). Each dot corresponds to a set of experiments under the same T, $\sigma_{\text{appl}}/\sigma_{\text{ath}}$, and $\mu = 0.7$. Red: homogeneous, and green: strongly heterogeneous. Adapted from [1]. 49
2.10 Initial quenched disorder introduced via the cohesion distribution for a **a)** homogeneous system and a **c)** strongly heterogeneous system, and its respective accumulated damage patterns at failure for a **b)** homogeneous system and a **d)** strongly heterogeneous system, when the kMC algorithm is launched six different times under the exactly same initial quenched disorder. 50
2.11 **a)** Dependency of V_{est}/V on the disorder level $\delta_{\Delta\sigma,0}/\langle\Delta\sigma\rangle_0$. **b)** Histogram of V_{est}/V. 51

3.1 Evolution of the cumulative probability distribution for the AE time series t_{j+1} in the set of **a)** experimental tests and **b)** FBM simulations. The red dashed line corresponds to a perfect lognormal distribution. Adapted from [2]. 56
3.2 Non–Markovian trajectories for individual **a)** experimental tests and **b)** FBM simulations. The inset figure is a zoom of the trajectories at early events. The color palette is a function of the creep lifetime t_f. Adapted from [2]. 57
3.3 Experimental results. **a)** Dependency of the creep failure time t_f on the arrival times t_{j+1} for different events $(j+1) = \{1, 40, 90\}$ (in green) compared to the theoretical result obtained from Eq. 3.4 (black dashed line). Evolution with j of **b)** the power–law exponent θ_{j+1}, and **c)** the power–law prefactor ψ_{j+1}, obtained from a power-law fit (green) and comparison to the theoretical result from Eqs. 3.5 and 3.6 (black dashed line). Evolution along j of **d)** the mean of the logarithm of the population of event times $\langle \ln t_{j+1} \rangle$. Dots: full population of samples, Squares: subpopulation of samples (the ones subjected to the same creep load $\mathrm{F}_{\text{appl}} = 245\mathrm{N}$). . . 58

3.4 Numerical results. **a)** Dependency of the creep failure time t_f on the arrival times t_{j+1} at an early stage $(j+1)=5$ (green squares) compared to the theoretical result obtained from Eq. 3.4 (black dashed line). Evolution along j of **b)** the power–law exponent θ_{j+1}, and **c)** the power–law prefactor ψ_{j+1}, obtained from a power-law fit (green squares) and comparison to the theoretical result from Eqs. 3.5 and 3.6 (black dashed line). 59

3.5 **a)** Evolution of the mean multiplier $\langle r_j \rangle = \langle \Delta t_{j+1}/t_j \rangle$ for the experimental results (red points), numerical results (green points), and theoretical result obtained from Eq. 3.8 in one FBM simulation (light green points). **b)** Evolution of the minimum gap for one simulation (light green points), and obtained solving $\Delta\sigma_{\min,j}$ in Eq. 3.8 from the experimental (red points) and numerical (green points) results. **c)** Evolution of the stress gap distribution for different values of j in one simulation. Adapted from [2]. 60

4.1 Schematic description of the prediction process through Bayesian inference. **a)** Temporal evolution of the strain rate $\dot{\varepsilon}$ (lightgreen) and cumulative number of AE event j (red). The data **x** come from the strain data set and the catalog of AE events read up to a time t_{obs}, and based on this data, one tries to predict the failure time t_f. **b)** Prior distribution $f(\vartheta)$, with $\vartheta = t_f$ in this example. **c)** By conditioning on the data **x**, one arrives at a posterior distribution, $f(\vartheta|\mathbf{x})$, from the strain data (ligthgreen) and AE events (red). Adapted from [3]. 65

4.2 **a)** An example of the failure time prediction from the strain signal. **b)** The evolution of the posterior distribution of the failure time (blue) as one changes the prediction time t_{obs} for a representative example. The green symbols show the prior distributions for the failure time for comparison. **c)** The proportion of predicted experiments for a given tolerance and prediction time t_{obs}, with a zoomed-in view below. Here, a 10 % precision is chosen. Adapted from [3]. 67

4.3 **a)** The evolution of the posterior distribution of the creep lifetime, $t_f^{\text{pred}} \sim f(t_f, \text{x})$, as one changes the observed time t_{obs} for one experiment. **b)** The prediction score ($\text{CRPS}_{\log}$) for all the experiments, where the bold lines represent the mean value for all the individual trajectories. Evolution of **c)** the power–law exponent θ_{j+1}, and **d**) the power–law prefactor ψ_{j+1}, for all the experiments taking the prediction at $t_{\text{obs}}/t_f^{\text{true}} \leq 0.9$. Lightgreen: the master curve approach, and red: the AE correlations approach. Adapted from [3]. 71

4.4 Influence of the prior of $\mathcal{N}$ on the predictions. **a)** The evolution of the posterior distribution of the creep lifetime as one changes the observed time t_{obs} for one experiment. **b)** Prediction score (CRPS_{log}) for all the experiments. The dashed line corresponds to the naive case $t_f^{\text{pred}} = t_{\text{obs}}$. Adapted from [3]. 72

6.1 Athermal experiments to obtain an average strength σ_{ath} at macroscale. **a)** Force – displacement curve and identification of maximum applied force (dots). **b)** stress – strain curve ($\sigma - \varepsilon$) and identification of the maximum applied stress σ_{ath} (dots). **c)** Tangent modulus $\text{d}\sigma/\text{d}\varepsilon$ as a function of the strain scaled by its value at σ_{ath}, $\varepsilon/\varepsilon(\sigma_{\text{ath}})$. The Young's modulus is defined as the average of the tangent modulus for $\varepsilon/\varepsilon(\sigma_{\text{ath}}) < 10^{-2}$ 80

6.2 Creep behavior in all the experiments. **a)** Temporal evolution of the strain ε. **b)** Temporal evolution of the strain rate $\dot{\varepsilon}$ and identification of the minimum strain rate $\dot{\varepsilon}_{\text{min}}$ (blue dots). **c)** Mechanical noise around the loading target. 81

6.3 Computation of the event time t_{j+1} and its radiated energy $E_{j+1}^{(\text{AE})}$. **a)** Continuous signal obtained from the AE sensor (light blue) in one creep test ($F_{\text{appl}} = 270\text{N}$) showing the amplitude $y(t)$. Location of the different event times t_{j+1}, the waiting time Δt_{j+1}, and the energy radiated by each one of the events $E_{j+1}^{(\text{AE})}$ (red circles), where the different sizes indicate the magnitude of the event. The black dashed line is the chosen amplitude threshold $A_{\text{thres}} = 1.48 \times 10^{-2}$. **b)** For two consecutive events, j and $j+1$, the identification of the respective parameters characterizing that event: the coda length $\Delta\tau_{j+1}$, the event time t_{j+1} (black square) and the energy $E_{j+1}^{(\text{AE})} = \int_{\tau_{j+1}}^{\tau_{j+1}+\Delta\tau_{j+1}} y^2 \text{d}t$ (light red region). 82

6.4 Example of the continuous signal obtained from the AE sensor (light blue) and evolution of the displacement (red) in one single creep test with $F_{\text{appl}} = 270\text{N}$. The black dashed line is the chosen amplitude's threshold $A_{\text{thres}} = 1.48 \times 10^{-2}$. Adapted from [2]. 83

6.5 **a)** Example of AE signal $y(t)$ in an individual creep experiment. Inset plot: zoom-in of the signal in a time interval and identification of different amplitude thresholds y_{thr} (dashed lines), where the dots are the amplitudes $|y(t)| > y_{\text{thr}}$. **b)** Number of events $\mathcal{N}$ leading to failure as a function of y_{thr} for all the creep experiments and its **c)** derivative $\mathrm{d}\mathcal{N}/\mathrm{d}y_{\text{thr}}$ to identify y_{thr} leading to divergence of the number of events. The black continuous line is the threshold implemented to obtain the catalog of events. 84

List of Tables

6.1 Summary of relevant data obtained from the creep experiments: Test code, applied creep load F_{appl}, creep lifetime t_f, and the acoustic emission events $\mathcal{N}$. 85

1. Introduction

This dissertation focused on the theoretical analysis of creep rupture using concepts from statistical physics, along with experimental data and numerical simulations. Creep is the time-dependent deformation of a material or system under a constant, long-term stress. It is relevant in many fields, such as material science [4, 5], civil engineering [6], soft matter physics [7–12] or geophysics and rock mechanics [13–15]. A three-stage model describes the creep phenomenology (Fig. 1.1) as follows: a primary or transient phase, a secondary or steady-state phase, and a tertiary or accelerating phase. During transient creep, strain increases with a logarithmic or power law dependence on time at a rate which depends on the applied stress and the material [16–19], and the strain rate is initially large due to the activation of 'soft spots' [20, 21]. A constant strain rate characterizes secondary creep over a period [17, 20], which, in many materials, can be interpreted as an inflection point between primary and tertiary creep [22]. During the last stage, the deformation rapidly increases before fracture [17, 23–25], or strain instability/fluidization, e.g., in soft matter [26].

In this work, the systems studied exhibit brittle and quasi-brittle behavior. It means we mainly study brittle creep, in which creep deformation results from the growth and coalescence of *microcracks*, i.e., *damage localization*. In materials like metals [4] or ice [27], creep can result from dislocation motion assisted by thermal activation. There are some analogies with brittle creep, such as thermal activation of weak spots (e.g., [20]), but others, such as damage, are irrelevant.

1.1 Motivation and background

Answering the question of how creep deformation and failure emerge in heterogeneous materials has both practical and theoretical significance. Prior studies have shown that the initial microstructure plays an important role in determining not only the mean but also the variability of failure time and strain [28, 29]. The proposed methodology will sharpen the precision

and reliability of characterizing this initial microstructure—an issue of direct relevance to civil engineering, materials science, and risk analysis —while also raising fundamental questions in statistical physics. Crucially, this work will push beyond the current state of the art, where failure prediction is only possible at the latest stages of deformation, by enabling forecasts much earlier in the creep process.

To understand the title of the present thesis, *Statistical physics of creep rupture of heterogeneous materials* it is important to get into each one of the main elements that cover this manuscript: empirical laws describing the creep physics, heterogeneous materials and the introduction of statistical physics to describe creep through the thermal activation concept, as well as another not less relevant key concept which is the elastic interaction kernel connecting the thermally activated events.

1.1.1 Creep phenomenology

To describe the *creep* phenomenology, some authors have developed empirical laws that work quite well across a wide range of materials, suggesting that this similarity stems from a universal physical law of creep, yet leaving a theoretical understanding lacking. Some of these empirical laws are:

- the power law decay of the strain rate which describes transient creep [20], i.e., $\dot{\varepsilon} \sim (t+c)^{-p}$ (see Fig. 1.1b), where $\dot{\varepsilon}$ is the strain rate, t the time and the constant c is a small delay timescale avoiding a singularity of the strain rate at $t=0$ [21], p is a constant varying between 0 and 1, e.g., $p=2/3$ corresponding to the Andrade's transient creep [16]. This law appears across a wide range of materials, including rocks [17], metals [16], paper [9], and concrete [30].

- during tertiary creep, the strain rate before failure is well described by a power law singularity consistent with a critical point concept [24, 31, 32], i.e., $\dot{\varepsilon} \sim (t_f - t)^{-\beta}$ (see Fig. 1.1c), where t_f is the creep lifetime, and β is a critical exponent. The term $t_f - t$ is the distance to failure.

- power law relationships between the failure time and some other quantities, e.g. the Monkman-Grant relationship which relates the creep lifetime with the minimum strain rate, $\dot{\varepsilon}_{\min} = \min\{\dot{\varepsilon}\}$, during secondary creep (see Fig. 1.1b-c), $t_f \sim \dot{\varepsilon}_{\min}^{-m}$, [22], or the relationship between the time at which the minimum strain rate occurs, $t_{\min} = t(\dot{\varepsilon}_{\min})$, and the failure time, $t_f \sim t_{\min}^{b}$ [10, 33].

- to follow the microcracking process during brittle creep, some authors often use Acoustic Emission (AE) [17]. AE event rate, also known as avalanche rate, $\dot{\mathscr{D}}$, follows an Omori-type relationship [34] during primary creep, $\dot{\mathscr{D}} \sim (t+c)^{-p'}$ and a reverse Omori law just before the

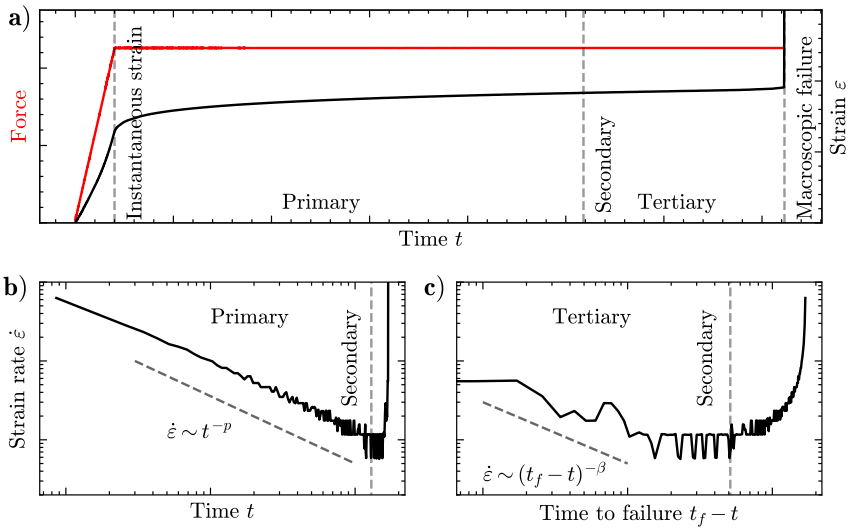


Figure 1.1. Illustration of typical creep phenomenology with deformation obtained from a tensile creep experiment on a sheet of paper. **a)** creep as a time-dependent deformation (black line) under constant applied load (red line). **b)** Power law decay of the strain rate during primary creep. **c)** Power law acceleration of the strain rate during tertiary creep.

macroscopic failure, $\dot{\mathscr{D}} \sim (t_f - t)^{-\beta'}$ [30, 35–37]. p' and β' are power-law exponents. .

1.1.2 Heterogeneous materials

Heterogeneous materials refer to materials whose local material properties vary spatially [38–40]. In this work, we describe heterogeneity, also known as spatial disorder, as the spatial variability of the local *quenched* yield stress and its implications at the global scale. The term quenched refers to heterogeneity introduced into the system via a random distribution of the yield stress, and breakdown governed by deterministic rules [41, 42]. In athermal mechanics of disordered materials this disorder combined with elastic stress interactions leads to various interesting phenomena, extensively studied for a few decades, e.g. in brittle materials such as rocks or concrete, some of the experimental observations are (i) high statistical fluctuations of the macroscopic strength—also known as athermal strength or failure stress—among different samples, (ii) dependency of the average strength on the system size, and (iii) presence of local damage localization [39]. Besides, the role of heterogeneity in the athermal fracture of a material is strong, in the sense that the more heterogeneous the material, the more deterministic the fracture process is if we have perfect knowledge of this disorder [43–46]. In real materials, signals of this heterogeneity emerge from the variation of physical quantities such as AE, elastic and electric

properties, among others [43, 44].

For the case of the creep fracture process in heterogeneous materials, the interaction between the quenched disorder and *thermal activation*, leads to the local excitation and breakage of 'soft' spots by the applied constant stress and thermal fluctuations, and later by the accumulation and cooperative interactions of microruptures, i.e., damage localisation and loss of stability in the sample [31, 47]. It is possible to describe the quenched heterogeneity and the thermal activation as two sources of "stochasticity" in the creep process. These two kinds of stochasticity interact and compete with each other; e.g., a less heterogeneous system is more sensitive to thermal noise, whereas, in the opposite case, heterogeneity governs the rupture, which becomes "deterministic" if the disorder distribution is known exactly, as stated above. In the present thesis, disorder and thermal noise are key to the evolution of the excitation spectrum of energy barriers —or stress gap distribution—. Section 1.1.4 will further discuss the connection between the thermal activation and the quenched heterogeneity.

1.1.3 Elastic interaction kernel

The creep rupture process consists of the breakage of elements by thermal activation —spots with a high probability of surpassing their energy barriers—, the accumulation of damaged clusters, and the cooperative interaction of microruptures. The way this process occurs is governed by the elastic interaction kernel, which regulates stress redistribution and the interaction between microcracks, thereby linking to spatial damage localization [31, 48]. In other words, the constant creep load $\mathrm{F}_{\mathrm{appl}}$ applied to the material does not imply that the stress distribution is spatially and temporally constant, and it affects the rupture process.

The *elastic stress redistribution kernel*, i.e., the physical law that governs stress redistribution after a damage event, plays a crucial role in understanding the creep rupture process. Mean-field (global) load redistribution is the most basic type of elastic interaction in which all the material is assumed infinitely stiff, and the stress redistributes equally along the material [49]. Local load sharing is the opposite of the elastic interaction case in mean-field, which arises when the material is very soft; i.e., the regions nearest to a microcrack experience greater stress redistribution [49]. This approach agrees with the stress enhancement around cracks described by Griffith's theory [50, 51]. One good example where we can see these two cases is the fiber bundle model (FBM), where the bundle formed by N fibers has an equal initial applied stress in all fibers, $\sigma_{n,0}^{\mathrm{appl}} = \mathrm{F}_{\mathrm{appl}}/N$. After some fibers break, the stress is redistributed equally among the surviving fibers in the mean-field (democratic) load-sharing model. For the local sharing case, the redistribution occurs only to the first neighbors. However, more realistic kernels are not mean-field, nor local, but long-range, where the

stress applied in all surviving fibers is dependent on the stress of the failed fiber, which redistributes following a power law decay with the distance among the surviving and broken fibers [49].

The elastic stress redistributes according to a yield criterion for damage/-plastic deformation or rupture, expressed in terms of stress state. These two concepts are key to understanding damage localization and formation of shear bands [31]. Some examples of yield criteria in the engineering literature include: Mohr-Coulomb to describe rocks or concrete [17], von Mises for amorphous plasticity [37], and the Tresca plastic criterion for metals. The correct choice of the yield criterion for a specific material determines how rupture clusters interact to reach failure. For instance, from the Tresca criterion, it is possible to obtain ductility with diffuse damage, and with the Mohr-Coulomb criterion, we can obtain brittleness with localized damage [31, 48].

In conclusion, to describe the creep rupture process, (i) an elastic stress redistribution law and (ii) a yield criterion combine to obtain a more realistic elastic interaction kernel. To gain a clearer understanding of these two concepts, let us consider a system formed by an elastic lattice subjected to a compressive creep load, with a long-range redistribution law and a local Mohr-Coulomb criterion. The Coulomb stress gives the local yield stress, expressed in terms of the internal cohesion C and the friction angle ϕ. The stress redistribution law is unique, whatever the value of C or ϕ. However, ϕ is crucial in the enhancement of shear stresses and consequently in the formation of shear bands with a failure plane angle Φ relative to the global major principal stress (vertically oriented in our case), such as $2\Phi = \pi + \phi/2$, with $\pi = 3.141\ldots$. Therefore, the mechanical interactions between two identical lattices but different ϕ will become completely different [31, 48].

1.1.4 Thermal activation

Creep lifetime t_f—Creep, seen as a time-dependent deformation, opens a strong connection to *statistical physics*. The role of thermal activation in creep deformation has been put forward for a long time [20], with suggestions of a creep lifetime in an Arrhenius form [14, 17, 47, 52]:

$$t_f \sim \frac{1}{\Omega_0} \exp\left(\frac{E}{k_B T}\right) \tag{1.1}$$

where $\exp(1) = e = 2.728\ldots$ is Euler's number, E is an activation energy, Ω_0 an attempt or thermal vibration frequency [47, 53], k_B the Boltzmann constant and T the thermodynamic temperature. In most studies, authors propose an expression similar to Eq. 1.1 at the *macroscopic* scale, with an activation energy poorly defined. At a *microscopic* scale, a connection between a local activation energy and a stress gap distribution —also known as the *excitation spectrum*—is defined. One important observation from the Arrhenius relation is that t_f depends strongly on the temperature and the

applied load. Furthermore, we can see that small variations in strength, strongly dependent on the disorder, translate into large differences in t_f, a feature observed in heterogeneous materials ranging from paper [10] to rocks [14, 54–56] and other engineering materials [57–59]. For that reason, some authors extend the definition of T in Eq. 1.1 to an effective temperature T_{eff}, dependent on T and the quenched disorder in the system [28, 29, 60, 61], creating a connection between the macro and the micro scale, which is not trivial, as will be shown in Chapter 2 about Publication I. The activation energy might connect to the spatial distribution of the heterogeneity through a gap $\Delta\sigma$ between a strength (stress threshold), and the applied stress, via $E \sim \Delta\sigma$, in the absolute reaction rates theory proposed by Eyring [62] or $E \sim \Delta\sigma^{3/2}$ in molecular systems [63].

From local thermal activation to inter-event times Δt_j—Let us imagine a solid, whose failure takes place by the accumulation of $\mathcal{N}$ successive local damage / fracturing events, i.e., creep lifetime is the sum of $\mathcal{N}$ inter-event times. Each event $j+1$ represents a transition by thermal activation of the entire system, with average waiting time of a single transition $\langle \Delta t \rangle_{j+1}$. In this framework, the jump rate ω_{j+1}, associated to a thermal transition, follows an Arrhenius formula [42, 53, 64]:

$$\omega_{j+1} \approx \Omega_0 \exp\left(-\frac{F_j}{k_B T}\right), \tag{1.2}$$

where the sub-index $j+1$ denotes the $(j+1)$th thermal transition, and F_j is the free energy barrier, inherited from the previous transition, to be overcome to trigger this event. The inversion of Eq. 1.2 gives the average waiting time between successive transitions, $\langle \Delta t \rangle_{j+1} = \omega_{j+1}^{-1}$ [53]:

$$\langle \Delta t \rangle_{j+1} = \frac{1}{\Omega_0} \exp\left(\frac{F_j}{k_B T}\right). \tag{1.3}$$

Here the inter–event time, Δt_{j+1}, between transitions follows an exponential distribution, $h(\Delta t_{j+1})_{j+1} = \omega_{j+1} \exp\left(-\omega_{j+1} \Delta t_{j+1}\right)$ [65, 66], with a mean and standard deviation equal to ω_{j+1}^{-1}. In brittle creep, $h(\Delta t_{j+1})_{j+1}$ is defined as a transitional probability of damage [67]. It can also be the probability of local plasticization, either from dislocation motion in metals or from shear transformation zones in glasses. It is important to note that $h(\Delta t_{j+1})_{j+1}$ is not constant as the jump rate ω_{j+1} varies due to the elastic stress redistribution in the system after a damage event occurs, modifying the energy barrier landscape.

Connection between the spatial heterogeneity and the thermal activation—The spatial heterogeneity of the material appears at the scale of the N number of subvolumes, indexed by n. Each element n has an associated activation energy, $E_{n,j}$, proportional to their local stress gap [21, 30, 37, 62],

which is evolving after the $(j+1)$th thermal transition occurs, as the result of previous transitions and their associated stress redistribution. In Eq. 1.3, the free energy barrier F_j is given by:

$$F_j = -k_B T \ln Z_j \tag{1.4}$$

where $Z_j = \Omega_0^{-1} \sum_n \omega_{n,j+1} = \sum_n e^{-E_{n,j}/k_B T}$, is the partition function [32, 68, 69], and the local jump rate, $\omega_{n,j+1} = e^{-E_{n,j}/k_B T}$ defines a probability, $p(E_{n,j+1})$, per unit time at the element n to generate a jump rate by thermal activation during the $(j+1)$th transition, where $p(E_{n,j+1}) = \omega_{n,j+1} Z_j^{-1}$. The local energy barrier here is defined proportional to the stress gap with an activation volume V as a proportionality constant, i.e., $E_{n,j} = V \Delta\sigma_{n,j}$ [42, 62]. As an alternative representation of the last equations, it is more convenient to introduce the density of states $g(E_{n_b,j})$, i.e., the number of sub-volumes that have an energy within a small range $E_{n_b,j} + dE_{n_b,j}$, and grouped in the bin n_b [32, 68]. We can then rewrite, $g(E_{n_b,j}) dE_{n_b,j} = N f(E_{n_b,j}) dE_{n_b,j}$, which can be replaced into Z_j [68]:

$$Z_j = N \sum_{n_b} f(E_{n_b,j}) e^{-E_{n_b,j}/k_B T}, \tag{1.5}$$

where $f(E_{n_b,j}) = g(E_{n_b,j})/N = f(\Delta\sigma_{n_b,j})/V$ represents the probability distribution of the activation energy, and is a function of the probability distribution of the stress gap —or excitation spectrum—, $f(\Delta\sigma_{n_b,j})$. In this thesis, $f(\Delta\sigma_{n,j})$ will be used, instead of $f(\Delta\sigma_{n_b,j})$, to represent the continuous excitation spectrum. Note that for the case $n_b \to \infty$, Eq. 1.5 becomes $Z_j = N \int_0^\infty f(E_{n,j}) e^{-E_{n,j}/k_B T} \mathrm{d}E_{n,j}$. The partition function of the system, Z_j, is a crucial term that incorporates the initial quenched disorder, accounts for the evolution of the excitation spectrum, and ultimately defines the spots that are more likely to be thermally activated.

Spatial heterogeneity analysis from the concept of entropy—Another definition from the free energy, largely used in statistical physics is $F_j = \langle E \rangle_j - T S_j$, where $\langle E \rangle_j$ is the internal energy and S_j is the entropy, $S_j = -k_B \sum_n p(E_{n,j}) \ln p(E_{n,j})$, used here from the 'lack' of information point of view, i.e., more related to the Shannon's entropy [70]. S_j could quantify the spatial heterogeneity of a system or the spatial structure of damage as done by Ref. [71]. In our case, we compute the explicit expression of S_j, obtaining:

$$S_j = k_B \ln \left[N \left\langle \exp\left(-\frac{E_{n_b,j} - \langle E \rangle_j}{k_B T} \right) \right\rangle \right]. \tag{1.6}$$

Equation 1.6 describes the entropy as a function of any stress gap distribution. A first key result is that the material heterogeneity of a system can indeed affect its entropy. A classical definition for the entropy is given by $S_j = k_B \ln(\mathscr{M})$ where $\mathscr{M}$ is the number of possible microstates, which in our specific case becomes $\mathscr{M} = N \langle \exp[-(E_{n_b,j} - \langle E \rangle_j)/k_B T] \rangle$ [68, 69]. One

obvious remark is that, for the case of a perfectly homogeneous system, the probability is $p(E_{n,j}) = 1/N$ and the activation energy in all elements is constant, $E_{n,j} = \langle E \rangle_j$, i.e., S_j reaches a maximum value equal to $k_B \log N$, which describes a system with all the elements n having the same probability of occurrence as found by Ref. [71]. It is also true for the $T \to \infty$ case. $k_B \log N$ represents the limit of infinite thermal disorder [32], or a high degree of spatial unpredictability [68], in the sense that thermal noise dominates the damage evolution.

1.2 Objectives

The main objective of this thesis is to understand how materials deform and damage when they are subjected to constant loads. In addition, understanding the physics underlying damage localization as failure approaches is relevant to engineering and materials science. Nevertheless, in classical mechanics and engineering literature, creep failure is described empirically, with an incomplete physical understanding, which does not allow for predicting failure from a more theoretical perspective. Therefore, this project aims to track progressive damage of a material under creep loading (i) from tensile creep experiments in a well-known heterogeneous material —normal office paper—using monitoring tools such as the Acoustic Emission (AE), and (ii) from a numerical model used to describe the mechanical behavior of brittle materials —e.g., rocks—. Then, to apply statistical physics theory to interpret the damage evolution and subsequently predict failure.

A further outcome of this research will be the prediction of creep lifetime using a Bayesian inference approach from early stages, building on numerical methods such as the fiber bundle model (FBM), progressive damage model (PDM), and a statistical physics framework implemented via a Bortz–Kalos–Lebowitz (BKL)–kinetic Monte Carlo (kMC) algorithm. The results of this thesis will help bridge the gap between local-scale mechanical response and the early-stage prediction of creep rupture. Finally, the methodology developed here may be extended to other heterogeneous materials, thereby expanding its applicability across a wide range of material classes with diverse mechanical properties, including brittle materials that exhibit damage-induced memory effects.

1.3 Thesis outline

This thesis provides supplementary theoretical background on the physical understanding of heterogeneous materials under constant loads. **Chapter 2** introduces the concept of thermal activation to explain creep rupture. It discusses the concept of effective temperature and its dependence on the

excitation spectrum $f(\Delta\sigma_{n,j})$, extending the results obtained in [28, 29] to include a dependence on the elastic interaction kernel, as already shown in Publication I. Furthermore, **Chapter 3**, based on Publication II, discusses a more general temporal inference framework, where damage history can help to make early-stage predictions about future failure, based on the non–Markovian trajectories shown by a sequence of AE event times t_{j+1}, which are explained by a random multiplicative behavior and extremal dynamics, creating a direct connection to the tail of the excitation spectrum.

Chapter 4 discusses an implementation of a Bayesian inference model, using Markov chain Monte Carlo (MCMC) methods. This approach integrates strain and AE data to provide reasonable predictions in the early creep stages, as shown in Publication III, based in part on the theoretical background of Publication II. Knowledge of the first arrival times is a way to "probe" the initial excitation spectrum of the sample/system —at least its tail—. This information is critical to understanding the full creep process and, consequently, creep failure. **Chapter 5** summarizes the main findings and conclusions of the thesis. Finally, **Chapter 6** presents the experimental and numerical methods employed in this work. Crucially, this work will push beyond the current state of the art, where recently failure prediction is only possible at the latest stages of deformation, by enabling forecasts much earlier in the creep process. It can be of relevant importance in fields such as materials science, geophysics, civil engineering, or risk analysis.

2. Effect of the local elastic interaction geometry on the creep lifetimes

Creep is a time-dependent deformation described as a thermally activated process, with the creep lifetime t_f given by an Arrhenius expression (Eq. 1.1). However, considering disorder in this approach presents difficulties. Some authors, based on a democratic fiber bundle model (DFBM), showed that Eq. 1.1 would be valid only if one substitutes the absolute temperature T by an effective temperature T_{eff} dependent on the initial quenched disorder, which works as an amplifier of the thermodynamic temperature T [28, 29, 72]. Some of their results indicate that the greater the spatial heterogeneity, the larger T_{eff} is, and therefore the smaller the average t_f. To explain that, Ref. [29] concluded that thermal activation and spatial disorder control the enhancement of the cracking process. In addition, for strongly heterogeneous samples/systems, t_f is essentially dictated by the quenched initial disorder and is less sensitive to the thermal noise. Nevertheless, these conclusions were obtained from a simple creep rupture model, and based on two rough assumptions: (i) a mean-field elastic stress redistribution after a fiber breaks, and (ii) an absence of memory effect of the broken fibers over the surviving ones as the broken fiber vanishes after the thermal activation.

In Publication I, a theoretical approach based on reaction-rate theory examines the concept of effective temperature and its implications for the creep lifetimes of materials. In addition, a numerical approach is used to implement a model that more accurately represents realistic situations, including local-scale memory effects and non-democratic elastic redistribution kernels. This path allows us to analyze the interplay among thermal activation, disorder, damage mechanics, and the nature of elastic interactions in creep rupture, with a particular focus on creep lifetimes. We implemented a numerical progressive damage model (PDM) which reproduces thermal activation via a Bortz–Kalos–Lebowitz (BKL) kinetic Monte Carlo (kMC) algorithm.

2.1 A theoretical approximation for the creep lifetime

2.1.1 General case

Using the statistical physics background mentioned in Section 1.1.4, it is possible to obtain a theoretical approximation for the mean creep lifetime $\langle t_f \rangle$ for a system described by an evolving energy landscape distribution $f(E_{n,j})$ whose initial average energy barrier is $\langle E_{\Delta\sigma} \rangle_0$, by doing some mathematical manipulations. First, one can combine Eqs. 1.4 and 1.3 to obtain another way to write the inter-event time, $\langle \Delta t \rangle_{j+1} = \Omega_0^{-1} Z_j^{-1}$. Then, a simple way to write $\langle t_f \rangle$ is by saying that it corresponds to the total number of thermal transitions $\mathcal{N}$ multiplied by the average inter-event time over the transitions' history, i.e., $\langle t_f \rangle = \mathcal{N} \Omega_0^{-1} \overline{Z_j^{-1}}$, with $\overline{(\cdot)}$ denoting the average over j. In this manner if one multiplies and divides by $\exp(\langle E_{\Delta\sigma} \rangle_0 / k_B T)$, $\langle t_f \rangle$ becomes:

$$\langle t_f \rangle = t_0 \exp\left(\frac{\langle E_{\Delta\sigma} \rangle_0}{k_B T_{\text{eff}}} \right) = \left(\overline{\Delta Z_j} \right) t_0 \exp\left(\frac{\langle E_{\Delta\sigma} \rangle_0}{k_B T} \right), \tag{2.1}$$

where $t_0 = \mathcal{N}/(N\Omega_0)$, and $\langle E_{\Delta\sigma} \rangle_0$ is proportional to the average of the initial stress gap distribution as $V \langle \Delta\sigma \rangle_0$ [62]. The term $\overline{\Delta Z_j} = Z_{0,\text{h}} \overline{Z_j^{-1}}$ is a correcting factor that takes into account the mean of the initial disorder, $Z_{0,\text{h}} = N \exp(-\langle E_{\Delta\sigma} \rangle_0 / k_B T)$, and the evolution of the excitation spectrum due to the thermal transitions, $\overline{Z_j^{-1}}$, i.e., due to memory effects. $\overline{\Delta Z_j}$ modifies the "simple" Arrhenius expression of t_f given in Eq. 1.1, by adding the initial quenched disorder and the evolution of the excitation spectrum during creep. Consequently, T_{eff} is given by:

$$k_B T_{\text{eff}} = \frac{k_B T}{1 + \dfrac{k_B T}{\langle E_{\Delta\sigma} \rangle_0} \ln \overline{\Delta Z_j}}. \tag{2.2}$$

If we check for extreme cases, in one hand, we could imagine an invariant homogeneous system with $f(E_{n,j}) = 1/N$ and $E_{n,j} = \langle E_{\Delta\sigma} \rangle_0$, then $Z_j = Z_{0,h}$ and $\overline{\Delta Z_j} = 1$ (red dashed line in Fig. 2.1a), and finally we get that $k_B T_{\text{eff}} = k_B T$ (red dashed line in Figs. 2.1b). On the other hand, we could think in a strongly heterogeneous system, so that the energy barrier distribution approximates a uniform distribution with $f(E_{n,j}) \approx 1/E_{\max}$ and initial average energy $\langle E_{\Delta\sigma} \rangle_0 \approx E_{\max}/2$, both functions of the maximum energy barrier which is much larger than the minimum value $E_{\max} \gg E_{\min}$. In this case it is easy to demonstrate that $Z_j \approx N E_{\max}^{-1} \int_0^\infty e^{-E_{n,j}/k_B T} \mathrm{d}E_{n,j} \approx N E_{\max}^{-1} k_B T$, and the correcting term becomes $\overline{\Delta Z_j} \approx (E_{\max}/k_B T) \exp(-E_{\max}/2k_B T)$, which is lower than one and tends to zero for $E_{\max} \to \infty$ (green dashed line in Fig. 2.1a). Studying these two simple cases, one can deduce that $\overline{\Delta Z_j}$ has a finite, non-negligible effect on t_f, i.e., $(E_{\max}/k_B T) \exp(-E_{\max}/2k_B T) < \overline{\Delta Z_j} \leq 1$. In the same way, it is possible to deduce that $\langle t_f \rangle$ varies from $t_0 \exp(\langle E_{\Delta\sigma} \rangle_0 / k_B T)$ for a homogeneous system to $2t_0 \langle E_{\Delta\sigma} \rangle_0 / k_B T$ for a strongly heterogeneous

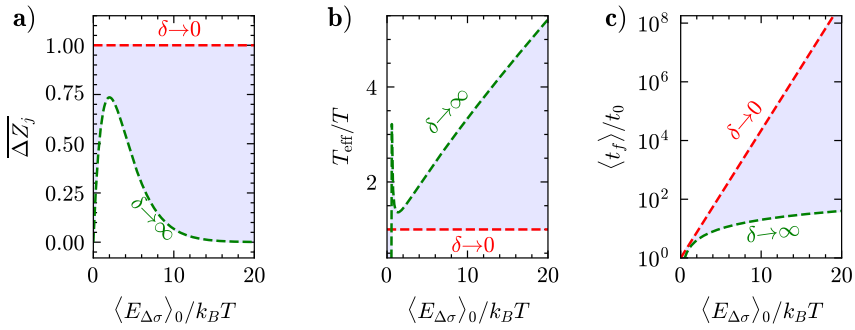


Figure 2.1. Schematic representation of the limits of zero and infinity disorder for different parameters as a function of the term $\langle E_{\Delta\sigma}\rangle_0/k_BT$. **a)** Correcting term $\overline{\Delta Z_j}$. **b)** Effective temperature T_{eff}/T. **c)** Creep lifetime $\langle t_f\rangle/t_0$. Red dashed line: Homogeneous case $\delta \to 0$, green dashed line: Strongly heterogeneous case $\delta \to \infty$. All intermediate cases of heterogeneity are in the filled blue zone.

system (see Fig. 2.1c). The main observations from this approach are in agreement with those obtained by Ref. [29].

2.1.2 Negligible mechanical interaction

For the case when the excitation spectrum remains invariable along the creep experiment (although unrealistic, this provides an approximation of $\langle t_f\rangle$ depending only on the initial quenched heterogeneity) the average creep lifetime is given by the first time step $\langle t_f\rangle \approx \mathcal{N}\langle\Delta t\rangle_1 \approx Nt_0\exp(F_0/k_BT) \approx Nt_0Z_0^{-1}$, with Z_0 given by Eq. 1.5, and the standard deviation δt_f given by $\delta t_f \approx \mathcal{N}^{-1/2}\langle t_f\rangle$.

If we define a specific distribution for the initial excitation spectrum, $f(\Delta\sigma_{n,0})$, we can provide a quantitative representation of the effect of quenched heterogeneity on t_f. Assuming a Gaussian distribution, with mean $\langle E_{\Delta\sigma}\rangle_0$ and standard deviation $\delta E_{\Delta\sigma,0}$, the term $\overline{\Delta Z_j} \approx \Delta Z_0$ becomes:

$$\overline{\Delta Z_j} \approx \Delta Z_0 = 2\exp\left[-\frac{1}{2}\left(\frac{\delta E_{\Delta\sigma,0}}{k_BT}\right)^2\right]\left[\text{erfc}\left(\frac{z_{var,0}}{\sqrt{2}}\right)\right]^{-1}, \tag{2.3}$$

where $z_{var,0} = \delta E_{\Delta\sigma,0}/k_BT - \langle E_{\Delta\sigma}\rangle_0/\delta E_{\Delta\sigma,0}$ and $\text{erfc}(\cdot) = 2/\sqrt{\pi}\int_{(\cdot)}^{\infty} e^{-x^2}dx$, the complementary Gaussian error function, which equals 2 for the homogeneous case, i.e., $\Delta Z_0 = 1.0$.

Generalization for the heterogeneity limits—In the case of strong heterogeneity, $\delta_{\Delta\sigma,0} \to \infty$ and quasi-homogeneity $\delta_{\Delta\sigma,0} \to 0$, we get that the asymptotics for the complementary error function reads $\text{erfc}(\cdot) \approx 2(1-H(\cdot)) + e^{-(\cdot)^2}/[(\cdot)\sqrt{\pi}]$, with $H(\cdot)$ the Heaviside step function. Then, the term ΔZ_0 is:

$$\Delta Z_0^{\delta_{\Delta\sigma,0}\to 0,\delta_{\Delta\sigma,0}\to\infty} = \frac{\sqrt{2\pi}\exp\left[-\frac{1}{2}\left(\frac{\delta E_{\Delta\sigma,0}}{k_BT}\right)^2\right]}{\sqrt{2\pi}H\left(-z_{var,0}\right) + z_{var,0}^{-1}\exp\left[-\frac{1}{2}z_{var,0}^2\right]}. \tag{2.4}$$

For a heterogeneous case, we take into account that $\delta_{\Delta\sigma,0} \sim \langle\Delta\sigma\rangle_0 > 0$, then we could say that $\langle\Delta\sigma\rangle_0 \approx z\delta_{\Delta\sigma,0}$ with $z = 1.96$, the value to get a 95% of confidence interval in a Gaussian distribution, but for sake of simplicity we define $z \approx 2$. With this approach for heterogeneity, Eq. 2.4 becomes:

$$\Delta Z_0^{\delta_{\Delta\sigma,0}\to\infty} \approx e^2\sqrt{\frac{\pi}{2}}\left[\frac{\langle E_{\Delta\sigma}\rangle_0}{k_BT} - 4\right]\left[\exp\left(-\frac{\langle E_{\Delta\sigma}\rangle_0}{k_BT}\right)\right], \tag{2.5}$$

and $k_BT_{\text{eff}} \approx \langle E_{\Delta\sigma}\rangle_0/[2 + \ln\sqrt{\pi/2}] \approx 0.45\langle E_{\Delta\sigma}\rangle_0$. The average creep lifetime is given by $\langle t_f\rangle \approx 9.3t_0(\langle E_{\Delta\sigma}\rangle_0/k_BT - 4)$. Eq. 2.5 applies in the case $\langle E_{\Delta\sigma}\rangle_0 \gg 4k_BT$, i.e., $\Delta Z_0 < \sqrt{8\pi\ln 2}/e^4 \approx 0.08$, $T_{\text{eff}}/T > 1.8$. For the quasi-homogeneous case, $\delta_{\Delta\sigma,0} \ll \langle\Delta\sigma\rangle$ and $\delta E_{\Delta\sigma,0} \ll k_BT$, the Eq. 2.4 is:

$$\Delta Z_0^{\delta_{\Delta\sigma,0}\to 0} \approx \exp\left[-\frac{1}{2}\left(\frac{\delta E_{\Delta\sigma,0}}{k_BT}\right)^2\right]. \tag{2.6}$$

Then, $k_BT_{\text{eff}} \approx k_BT/\left(1 - 0.5\frac{\delta E_{\Delta\sigma,0}}{\langle E_{\Delta\sigma}\rangle_0}\frac{\delta E_{\Delta\sigma,0}}{k_BT}\right)$, and the average creep lifetime reads $\langle t_f\rangle \approx t_0\exp[\langle E_{\Delta\sigma}\rangle_0/k_BT) - 0.5(\delta E_{\Delta\sigma,0}/k_BT)^2]$.

2.2 Description of the numerical model

We obtained from the theoretical approach that the main observations are in agreement with the results obtained by Ref. [29], i.e., t_f is expressed by an Arrhenius-like relation, but with a T_{eff} instead of T, which is dependent on the initial quenched disorder in the system. Now, from a numerical perspective, we study T_{eff} using a more realistic, non-mean-field elastic interaction kernel. We performed numerical simulations of a PDM [31, 73–76] with thermal activation [21, 30] implemented via a kMC algorithm. The main characteristics of the model are explained below.

2.2.1 Athermal model

The PDM was conceived to mimic the physical response of brittle materials, e.g., rocks or concrete, under uniaxial compression tests, i.e., in athermal conditions [31]. A common shape for the specimens has a height–to–diameter ratio of 2:1. This choice is made so that the final fault would not initiate from the corner of the sample, which would likely be the case with a 1:1 ratio specimen. In other words, it ensures that the angle of the failure normal surface, Φ, has typical values around $45° - 60°$ with respect to the major principal stress direction [18, 77].

Then, the PDM considers a bidimensional elastic domain under plane strain conditions, with a height-to-width ratio of 2:1, avoiding the final fault appearing most of the time along the diagonal of the sample. The system/sample consists of an isotropic elastic material with an initial Young's modulus Y_0 and Poisson's ratio ν. It is discretized into an unstructured

mesh using the Finite Element Method (FEM), thereby generating N homogeneous cells of mesoscopic size [73]. To mimic uniaxial compression, the domain is initially loaded in small stress steps along the y–axis, with the lower boundary fixed and free lateral-displacement allowed in the x–axis. The local stress–strain field $(\sigma_n^{\text{appl}}, \varepsilon_n^{\text{appl}})$ is computed using a FEM procedure, and the vertical global strain ε is given by the vertical deformation in the upper boundary—average of the local displacements—divided by the initial sample's height. The stress field variation could cause some elements to fail by traction, as the model is not scalar [31, 74]. We implement the initial quenched heterogeneity through the local strength, which also defines the local damage threshold σ_n.

When $\sigma_n^{\text{appl}} \geq \sigma_n$, the local Young's modulus, Y_n, is decreased by a damage factor $1-D$, with $D<1$, a term related to the cracks density [78]. Each exceedance of σ_n produces a local damage event in the element n. The damage accumulates, and after a number $\mathscr{D}_n$ of accumulated damage events, Y_n falls to $Y_n = (1-D)^{\mathscr{D}_n} Y_0$ [75], while ν remains unaffected by this damage. Initially, the material is undamaged, and the stress state is homogeneous. This stress field becomes heterogeneous once the first damage event occurs, due to elastic stress redistribution.

The static equilibrium is recalculated after a damage event, redistributing σ_n to the surrounding elements and comparing the updated stress field with the local thresholds. If any threshold is exceeded, an avalanche of damage is triggered; the process stops when all elements are below their thresholds. The total number of events during a stress step defines the avalanche size [31]. In laboratory monotonic compression tests, recording acoustic emissions provides a quantitative measure of avalanche size [14, 79–82].

The local threshold for damage is expressed in terms of the Mohr–Coulomb (MC) criterion, relevant for geomaterials under compressive stress states [18], $\sigma_{\parallel,n} - \sigma_{\perp,n} \tan\phi = C_n$, where the left side of the expression is known as the Coulomb stress, with $\sigma_{\parallel,n}$ and $\sigma_{\perp,n}$ the shear and the normal stress over an orientation that maximizes the Coulomb stress. C_n is the cohesion, and ϕ is the internal friction angle. ϕ is key in quantifying the orientation of the failure normal surface, $\Phi = \pi/4 + \phi/2$, and the coefficient of friction, $\tan\phi = \mu$. The comparison between the Coulomb stress and the cohesion allows us to define a tensorial model in terms of a scalar stress gap. We introduce microstructural heterogeneity [39] via the local cohesion C_n, which is set randomly from a Gaussian distribution (Fig. 2.2a):

$$f_C(C_n) = \frac{1}{\sqrt{2\pi}\delta C} \exp\left[-\frac{1}{2}\left(\frac{C_n - \langle C\rangle}{\delta C}\right)^2\right], \tag{2.7}$$

with $\langle C\rangle$ and δC, the mean and standard deviation of C_n respectively. C_n remains unchanged to mimic quenched disorder, while μ is set constant in space and time.

An initial linear elastic response followed by a macroscopic softening describes the mechanical response of the system in the athermal version,

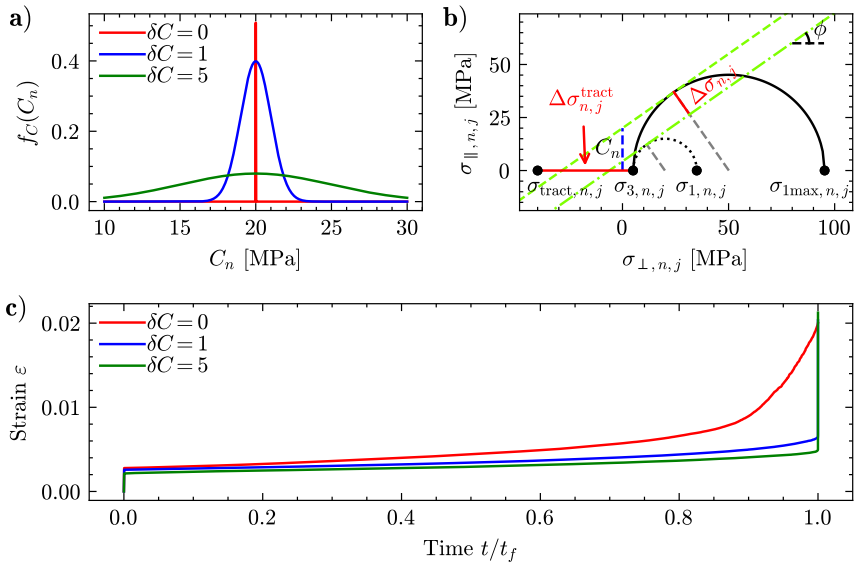


Figure 2.2. Different parameters of the thermally activated progressive damage model: **a)** Gaussian probability distribution of the cohesion for different disorder levels. **b)** Representation of the MC criterion at microscale and the identification of its respective local stress gap $\Delta\sigma_{n,j}$, and identification of an additional traction criterion, $\Delta\sigma^{\text{tract}}_{n,j}$, in cases where $\sigma_{3,n,j} < 0$. **c)** Example of the temporal evolution of the macroscopic axial strain for creep simulations at different disorder levels. Adapted from [1].

reaching the peak stress —also called athermal strength σ_{ath}—at the end of the softening, and finally showing a large stress drop mimicking a macroscopic rupture [31, 75]. This model captures the Coulombic failure of materials such as rocks and concrete quite well [83]. The numerical limitations of the PDM have been extensively studied by Ref. [73], e.g., the effects of the small deformations assumption from the FEM, the cell shape effects on the damage localization and the macroscopic behavior, the effects of a purely elastic damage, among others. Ref. [73] mainly found no effect of mesh size or aspect ratio on the damage evolution behavior [31, 73]. In our case, from the theoretical approximation of $\langle t_f \rangle$ in Section 2.1, $\langle t_f \rangle = t_0 \exp(\langle E_{\Delta\sigma} \rangle_0 / k_B T_{\text{eff}})$, it could be checked a possible size effect, just on the term $t_0 \sim \mathcal{N} N^{-1}$, as the exponential term is size independent. Then, it is logical to think that $\mathcal{N}$ will increase as N increases, e.g., as a power-law $\mathcal{N} \sim N^a$, with $a \geq 1$. The linear dependency case, $a = 1$, corresponds to the non-size effect case. In our numerical results, we examined the effects of sample size during the creep phase and found that the main conclusions are size-independent (See Section 2.3.1).

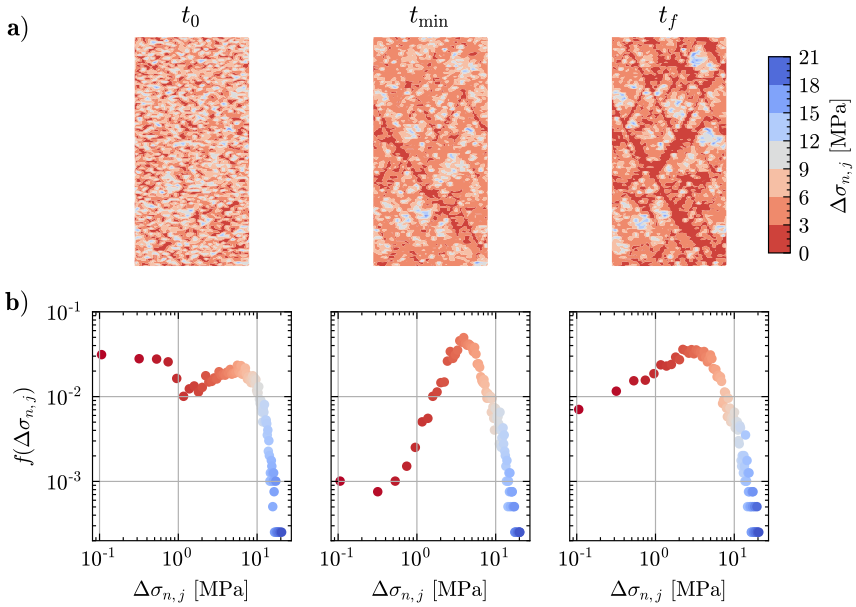


Figure 2.3. **a)** Example of the evolution of the stress gap field $\Delta\sigma_{n,j}$, and **b)** its respective excitation spectrum $f(\Delta\sigma_{n,j})$ at different stages: initial $t_0 = 0$, end of primary creep $t_{\min} = t(\dot{\varepsilon}_{\min})$, and rupture time t_f. Adapted from [1].

2.2.2 Thermal activation

In the athermal version, time is not implemented, and damage occurs only when the external stress or deformation increases in small loading steps. To describe the time-dependent deformation under constant load, thermal activation and a physical timescale are introduced via a BKL–kMC algorithm [64, 84], whose main details are described in Section 6.2. The implementation in the PDM was carried out by Refs. [21] and [30]. The model is initially run athermally up to a target uniaxial stress σ_{appl}, with $\sigma_{\text{appl}}/\sigma_{\text{ath}} < 1$. Creep starts when the load reaches σ_{appl}, defining here $t = 0$.

At the local —element—scale, the gap $\Delta\sigma_{n,j}$ between the local stress state and the MC envelope is linearly proportional to the energy barrier, $E_{n,j} = V\Delta\sigma_{n,j}$ [21, 62]. The goal of the kMC algorithm is to activate one single element n per thermal transition, according to the rates of the individual processes, $\omega_{n,j+1}$ [21, 30, 53], triggering one single damage event and increasing the time from t_j to $t_{j+1} = t_j + \Delta t_{j+1}$, with $\Delta t_{j+1} = -(\Omega_0 Z_j)^{-1} \ln u_{j+1}$ (Eq. 6.7), and $0 < u_{j+1} < 1$ a random number (see Section 6.2 for more details). The internal stress-strain field is recalculated after any $(j+1)$th-thermal transition, and an athermal avalanche of damage events might occur, i.e. $(\sigma^{\text{appl}}_{n,j}, \varepsilon^{\text{appl}}_{n,j}) \rightarrow (\sigma^{\text{appl}}_{n,j+1}, \varepsilon^{\text{appl}}_{n,j+1})$. The avalanche duration is considered negligible compared to the creep timescales; i.e., Δt_{j+1} remains unchanged. Then, the local Young's modulus, $Y_{n,j}$, falls to $Y_{n,j+1} = (1-D)^{\mathscr{D}_{n,j+1}} Y_{n,0}$, with

$Y_{n,0}$ the local elastic modulus inherited from the athermal phase and $\mathscr{D}_{n,j+1}$ the local accumulated number of damage events. As a way to quantify the local damage, one can introduce the term $1-Y_{n,j}/Y_{n,0} = 1-(1-D)^{\mathscr{D}_{n,j}}$, where 0 represents no local damage and 1 a completely damaged element.

To simulate brittle creep [17], we use the local MC criterion to define a Coulomb stress gap $\Delta\sigma_{n,j}$ between the local C_n cohesion and the local Coulomb stress $\sigma_{\parallel,j} - \sigma_{\perp,j}\tan\phi$ (see Fig. 2.2b):

$$\Delta\sigma_{n,j} = C_n\cos\phi + \sigma_{3,n,j}\frac{1+\sin\phi}{2} - \sigma_{1,n,j}\frac{1-\sin\phi}{2}, \tag{2.8}$$

where $\sigma_{1,n,j}$ and $\sigma_{3,n,j}$ are respectively the local major and minor principal stresses (see Fig. 2.2b), $\cos\phi = (1+\mu^2)^{-1/2}$ and $\sin\phi = \mu(1+\mu^2)^{-1/2}$. In this approach, the intermediate principal stress is $\sigma_{2,n,j} = \nu(\sigma_{1,n,j}+\sigma_{3,n,j})$. Note that in rare cases, some elements n could fail by traction due to the tensorial nature of the model. In such cases, we implemented a traction stress gap, which compares a traction stress threshold $\sigma_{\text{tract},n}$ to $\sigma_{3,n,j}$, i.e., $\Delta\sigma^{\text{tract}}_{n,j} = \sigma_{\text{tract},n} - \sigma_{3,n,j}$. Then, the local stress gap to compute $E_{n,j}$ is given by $\Delta\sigma_{n,j} = \min\{\Delta\sigma_{n,j}, \Delta\sigma^{\text{tract}}_{n,j}\}$.

The evolving excitation spectrum $f(\Delta\sigma_{n,j})$ (e.g. Fig. 2.3), corresponds to a convolution of probability distributions [32]:

$$f(\Delta\sigma_{n,j}) = \left(f_C * f_{\sigma_1,\sigma_3}\right)(\Delta\sigma_{n,j}) \sim \int_{-\infty}^{\infty} f_C(C_n\cos\phi) f_{\sigma_1,\sigma_3}(\Delta\sigma_{n,j} - C_n\cos\phi)\mathrm{d}C_n \tag{2.9}$$

with $f_C(C_n\cos\phi) = f_C(C_n)/\cos\phi$, and f_{σ_1,σ_3} the probability distribution of the stress state, $f_{\sigma_1,\sigma_3}(\Delta\sigma_{n,j} - C_n\cos\phi) = \left(f_{\sigma_1} * f_{\sigma_3}\right)(\Delta\sigma_{n,j} - C_n\cos\phi)$. In the model, final failure occurs once the axial macroscopic strain reaches a predefined maximum value $\varepsilon_j > \varepsilon_{\max}$, with $\varepsilon_{\max} = \text{const.}$, coming from the strain rate divergence during tertiary creep, thus defining t_f (see Fig. 2.2c).

Theoretical approach for the dependence of T_{eff} on C_n and ϕ–In the extreme case when no damage occurs during the athermal phase, the only term affecting the initial excitation spectrum at the onset of the creep stage is $f_C(C_n) = f(C_n)$, as the initial stress field is homogeneous, with $\sigma_1 = \sigma_{\text{appl}}$ and $\sigma_3 = 0$ spatially invariant. Afterward, the initial stress gap distribution adopts the shape of the cohesion distribution, $f(\Delta\sigma_{n,0}) = f(C_n)/\cos\phi$. Then, the starting local gap becomes $\Delta\sigma_{n,0} = C_n\cos\phi - \sigma_{\text{appl}}(1-\sin\phi)/2$, with an average $\langle\Delta\sigma\rangle_0 = \langle C\rangle\cos\phi - \sigma_{\text{appl}}(1-\sin\phi)/2$ and standard deviation $\delta_{\Delta\sigma,0} = \delta C\cos\phi$. In this naive case, it is possible to get a theoretical approximation of the term ΔZ_0 in Eq. 2.3 as a function of the internal distribution of the cohesion, the internal friction angle, the applied stress and the temperature, i.e., $\Delta Z_0 = \Delta Z_0(C_n, \phi, V\sigma_{\text{appl}}, k_BT)$:

$$\Delta Z_0^{(C_n,\phi)} = \frac{2\exp\left[-\dfrac{\cos^2\phi}{2}\left(\dfrac{V\delta C}{k_BT}\right)^2\right]}{\operatorname{erfc}\left[\dfrac{1}{\sqrt{2}}\left(\dfrac{V\delta C}{k_BT}\cos\phi - \dfrac{\langle C\rangle}{\delta C} + \dfrac{\sigma_{\text{appl}}}{2\delta C}\dfrac{\cos\phi}{1+\sin\phi}\right)\right]}. \tag{2.10}$$

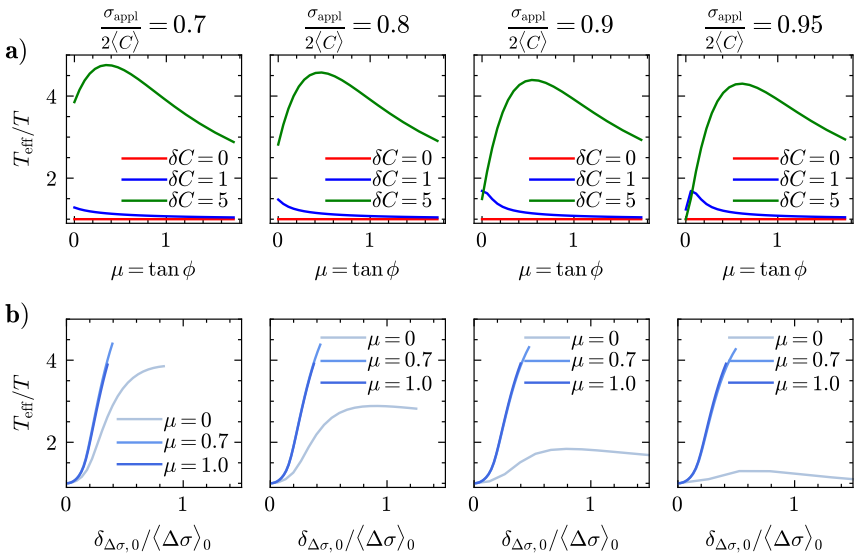


Figure 2.4. a) Theoretical dependency of the effective temperature T_{eff} on the friction coefficient μ, for different initial quenched disorder values given in terms of the cohesion C_n: homogeneous (red), intermediate (blue), and large disorder (green). **b)** Theoretical dependency of the effective temperature T_{eff} on the initial quenched disorder term $\delta_{\Delta\sigma,0}/\langle\Delta\sigma\rangle_0$, for different friction coefficients: $\mu = 0$ (light blue), $\mu = 0.7$ (blue) and $\mu = 1.0$ (dark blue), where the dashed lines are the approximation for the infinity–disorder limit given by Eq. 2.4. Each case was computed under different applied stress $\sigma_{\text{appl}}/\langle C\rangle$, with $\langle C\rangle = 20$MPa and $T = 300$K.

The effective temperature could be obtained by replacing Eq. 2.10 in Eq. 2.2:

$$k_B T_{\text{eff}} = \frac{k_B T}{1 + \dfrac{2k_B T \ln \Delta Z_0^{(C_n,\phi)}}{2V\langle C\rangle(1+\sin\phi) - V\sigma_{\text{appl}}\cos\phi}\dfrac{1+\sin\phi}{\cos\phi}}$$

$$= \frac{k_B T}{1 + \dfrac{2\sqrt{1+\mu^2}}{2\langle C\rangle - \sigma_{\text{appl}}(\sqrt{1+\mu^2}-\mu)}\dfrac{k_B T}{V}\ln \Delta Z_0^{(C_n,\phi)}}. \quad (2.11)$$

From Eq. 2.11, one can observe that T_{eff} shows a dependency not only on the initial quenched disorder (see Fig. 2.4b), but also on μ (see Fig. 2.4a), with important implications on the fracture process and the failure time. The term $\delta_{\Delta\sigma,0}/\langle\Delta\sigma\rangle_0$ is a representation of the initial level of disorder comparing the standard deviation and the mean of $\Delta\sigma_{n,0}$. For larger μ, the damage localization becomes more significant, and it is a key parameter when the applied stress is near the athermal stress. In addition, replacing Eq. 2.10 in Eq. 2.1, and calling

$$z_{var,0}^{(C_n,\phi)} \approx \frac{V\delta C}{k_B T}\cos\phi - \frac{\langle C\rangle}{\delta C} + \frac{\sigma_{\text{appl}}}{2\delta C}\frac{\cos\phi}{1+\sin\phi},$$

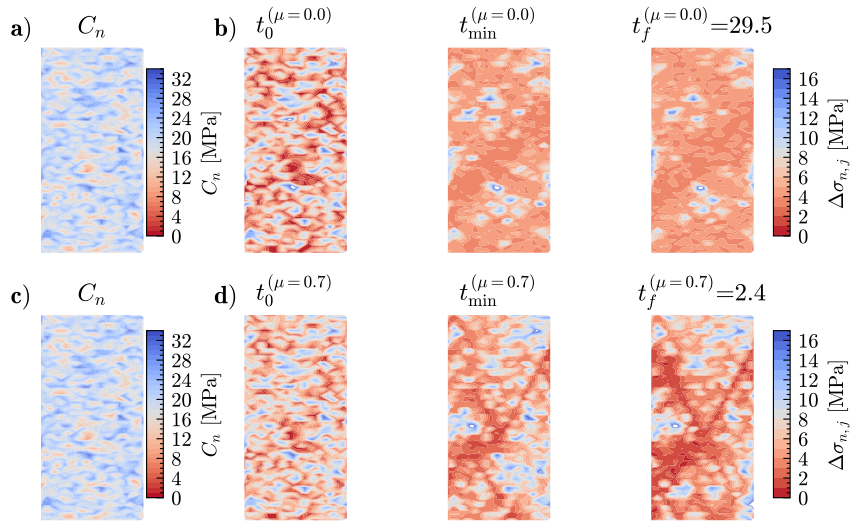


Figure 2.5. Influence of the internal friction coefficient, $\mu = \{0.0, 0.7\}$, on the elastic interaction geometry. **a)** and **c)** Cohesion field, set as the same for both cases. Example of the evolution of the stress gap field $\Delta\sigma_{n,j}$ for different friction coefficients: **b)** $\mu = 0.0$ and **b)** $\mu = 0.7$, at different stages: initial $t_0 = 0$, end of primary creep $t_{\min} = t(\dot{\epsilon}_{\min})$, and rupture time t_f. t_f is given in arbitrary units.

the failure time becomes:

$$\frac{\langle t_f \rangle^{\text{theor}}}{t_0} \approx 2\exp\left[\left(\frac{V\delta C}{k_B T}\right)^2 \frac{\cos^2\phi}{2}\right] \frac{\exp\left[-z_{var,0}^{(C_n,\phi)} \frac{V\delta C}{k_B T}\cos\phi\right]}{\operatorname{erfc}\left[\frac{z_{var,0}^{(C_n,\phi)}}{\sqrt{2}}\right]}, \tag{2.12}$$

Eq. 2.12 is an explicit representation of the failure time as a function of the initial quenched disorder and the elastic interaction kernel under the assumption that no significant damage occurs during the loading phase before starting the creep stage (see dashed lines in Fig. 2.6).

2.3 Numerical results

2.3.1 Effective temperature and dependency on the heterogeneity and the elastic interaction geometry

Influence of the friction coefficient on the elastic interaction geometry–In Section 2.2.1, we introduced the MC criterion based on two key parameters: the cohesion C_n and the friction coefficient μ [18, 77]. To describe realistic mechanical behavior in geomaterials, μ plays a crucial role. It is a physical parameter that links sliding at discrete discontinuities and is defined as the ratio of shear forces to normal forces required to initiate (static fric-

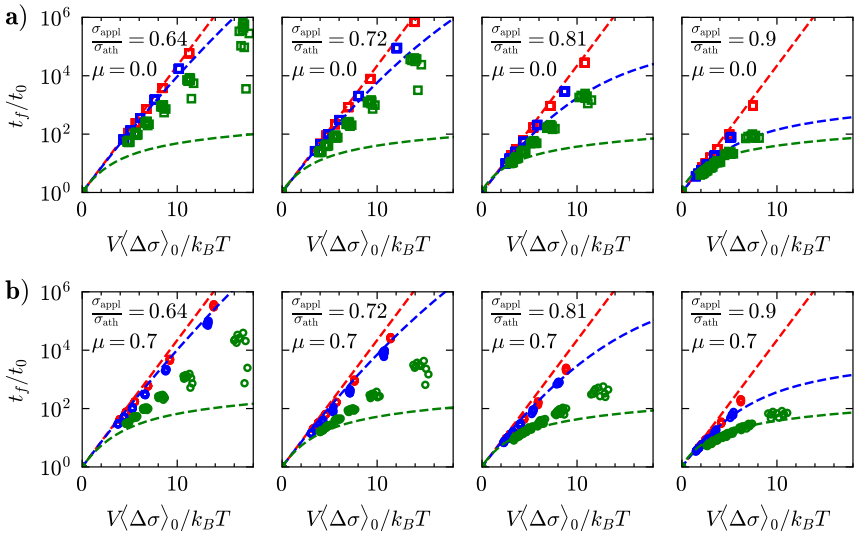


Figure 2.6. Theoretical (dashed line) vs. numerical (squares, dots) results for t_f/t_0 dependency on the term $V\langle\Delta\sigma\rangle_0/k_BT$, for different values of the stress ratio $\sigma_{appl}/\sigma_{ath}$ and friction coefficients **a)** $\mu = 0.0$ (squares) and **b)** $\mu = 0.7$ (dots). The different colors represent homogeneity (red), intermediate heterogeneity (blue), and strong heterogeneity (green). The theoretical curves are obtained with Eq. 2.12. Adapted from [1].

tion) or maintain (kinetic friction) sliding. It is constant from a classical perspective [77]. Two classical values of friction coefficient are $\mu \approx 0.7$ for geomaterials [18], and $\mu \approx 0.0$ where the MC criterion reduces to a Tresca plastic criterion [31], i.e., it is independent of the normal stress $\sigma_\perp$, and it is used, e.g., as a plastic yield criterion for metals. More recently, from athermal simulations in a PDM, Refs. [31, 73] found that μ controls the local interaction kernel between inhomogeneities, i.e., the transition from diffuse to localized damage. They also found that the ductile and brittle macroscopic response is merely a consequence of the progressive damage localization in systems with different values of μ, e.g., ductile response with diffuse damage for the case $\mu = 0$ and brittle behavior with damage localization for $\mu = 1.0$. The physical explanation of such a behavior lies in the evolution of the stress gap field, $\Delta\sigma_n$, which is a good quantifier of the interaction between defects: (i) for lower values of μ, the surrounding area of a weak spot shows a low gradient, meaning that the interaction happens in all directions. (ii) For higher values of μ, the gap field shows a strong directionality and strong gradient increasing with the damage progress, meaning that the interaction in the neighborhood will be limited to a localized domain [31, 73]. We extended these findings to creep tests, more exactly to numerical simulations with the same cohesion field C_n, temperature T, and ratio $\sigma_{appl}/\sigma_{ath}$, but different internal friction coefficients, $\mu = 0.0$ and $\mu = 0.7$. We obtained results similar to those found by [31] (see

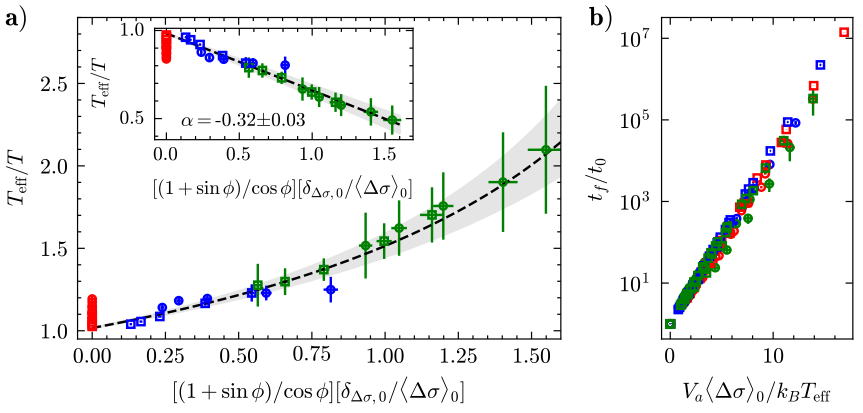


Figure 2.7. a) Effective temperature ratio T_{eff}/T as a function of the heterogeneity. **b)** Dependency of the lifetime t_f/t_0 on $V_a\langle\Delta\sigma\rangle_0/k_BT_{\text{eff}}$. Squares: $\mu = 0.0$, dots: $\mu = 0.7$. Red: homogeneous, blue: intermediate, green: strongly heterogeneous. Adapted from [1].

Fig. 2.5). It is worth noting that at the onset of the creep behavior, the sample with implemented $\mu = 0$ (left on Fig. 2.5b) shows more damaged spots than the case $\mu = 0.7$ (left plot on Fig. 2.5d), which means more diffuse damage during the athermal phase. However, with a different consequence at failure, i.e., for $\mu = 0.0$, the stress gap field $\Delta\sigma_{n,j}$ shows a more homogeneous distribution of the damage, which intuitively suggests that it will take a longer time to reach the failure (see right plot on Fig. 2.5b and Fig. 2.6a). For $\mu = 0.7$, as expected, the gap field shows a strong directionality of the weakest spots —elements in the tail of $f(\Delta\sigma_{n,j})$ —, i.e. the damage process concentrates in specific areas and will take less time to reach the boundaries of the system (see right plot on Fig. 2.5d and Fig. 2.6b).

Influence of the elastic interaction geometry on the creep lifetimes–In Section 2.2.2, we studied the case of a material with initial quenched disorder, while neglecting elastic stress redistribution and memory effects during the deformation, we found from an analytical approach that $\langle t_f \rangle$ follows an Arrhenius-like expression, with T_{eff} increasing with the heterogeneity of the material as found by Refs. [28, 29], but also dependent on μ (see Eq. 2.12). In Fig. 2.5, we have shown for a simple comparison the spatial effect of μ on the elastic interaction kernel, and in Fig. 2.4, we have plotted this theoretical dependency for different values of μ and δC, finding that the average creep lifetime $\langle t_f \rangle$ is inversely dependent on μ and δC. Then, here we will extend this analysis to different cases involving heterogeneity, temperature, and creep load. We conducted a numerical study of three configurations of the initial quenched heterogeneity, ranging from homogeneous (in red) to strongly heterogeneous (in green), and two values of the friction coefficient to represent two different shapes of the elastic interaction kernel at the

local scale. In Fig. 2.6, we see that these theoretical results (dashed lines) obtained with Eq. 2.12 agree quite well with the numerical simulations using the PDM (squares and dots) in the quasi-homogeneous cases (red and blue) and for some cases of the strong heterogeneity level, when the applied load is near the athermal strength. It indicates that elastic interactions during creep have a limited effect in the cases mentioned, and the initial quenched disorder dominates the creep rupture process. When the creep load is far from the athermal strength, elastic interactions become more important, and the creep failure time is much larger than the theoretical value by a factor of $2-3$ orders of magnitude.

From the numerical results, we found that T_{eff} does not only depend on the initial disorder, but also on the nature of the elastic interaction kernel, with an increasing convexity enhancing T_{eff} (see Fig. 2.7a) and represented empirically by:

$$k_B T_{\text{eff}} \approx \frac{k_B T}{1-\alpha \dfrac{1+\sin\phi}{\cos\phi} \dfrac{\delta_{\Delta\sigma,0}}{\langle \Delta\sigma \rangle_0}} \approx \frac{k_B T}{1-\alpha \left(\mu + \sqrt{1+\mu^2}\right) \dfrac{\delta_{\Delta\sigma,0}}{\langle \Delta\sigma \rangle_0}}, \tag{2.13}$$

where $\alpha = 0.32 \pm 0.03 \approx 1/3$ results from a linear regression (see subfigure in Fig. 2.7a). The term $\delta_{\Delta\sigma,0}/\langle \Delta\sigma \rangle_0$ is a representation of the initial level of disorder comparing the standard deviation and the mean of $\Delta\sigma_{n,0}$. Here, the term μ explicitly represents the effect of the elastic interaction kernel. If one replaces $k_B T$ by $k_B T_{\text{eff}}$ (Eq. 2.13) in the expression for the creep rupture time, $t_f = t_0 \exp(V \langle \Delta\sigma \rangle_0 / k_B T)$ (Eq. 1.1), all the data collapse (see Fig. 2.7b), showing the importance of the dependence of t_f on T_{eff}.

In our numerical approach, we compute the different results during the creep phase for two different system sizes: $N = 960$ triangular elements (Fig. 2.8a) and $N = 3968$ triangular elements (Fig. 2.8b). We found no significant differences in t_f between them; the same holds for T_{eff}. Then. the main conclusions are size-independent, and at least with $960 \leq N \leq 3968$, we coud infer that $\mathcal{N} \sim N$.

2.3.2 Variability of the creep lifetime around its average

We studied t_f from numerical simulations under the same initial conditions ($T = \text{const.}$, $\sigma_{\text{appl}}/\sigma_{\text{ath}} = \text{const.}$, $\delta C = \text{const.}$), but different realizations of the initial quenched heterogeneity (random seed to generate C_n variable among samples) and the thermal disorder (random seed to generate u_{j+1} variable among samples). The analysis shows that the variability of the creep failure time, δt_f, is essentially proportional to its average, $\langle t_f \rangle$, i.e., $\delta t_f \sim \langle t_f \rangle$ (see Fig. 2.9b). Surprisingly, it is also true for the case of fixed spatial distribution of the initial quenched heterogeneity (random seed to generate C_n invariable among samples), but different realizations of the thermal disorder (random seed to generate u_{j+1} variable among samples),

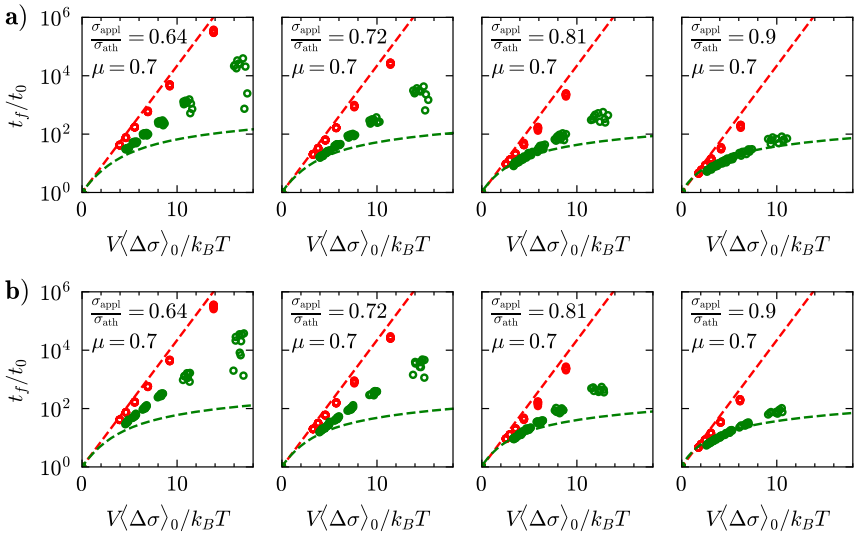


Figure 2.8. Size cell independence of the creep lifetime t_f. Theoretical (dashed line) vs. numerical (squares, dots) results for t_f/t_0 dependency on the term $V\langle\Delta\sigma\rangle_0/k_BT$, for different values of the stress ratio $\sigma_{\text{appl}}/\sigma_{\text{ath}}$, friction coefficient $\mu = 0.7$ and two different system sizes: **a)** $N = 960$ and **b)** $N = 3968$. The different colors represent homogeneity (red) and strong heterogeneity (green). The theoretical curves are obtained with Eq. 2.12.

$\delta t_{f,\text{thermal}} \sim \langle t_f \rangle_{\text{thermal}}$ (see Fig. 2.9a). This proportionality is a characteristic of the quasi-independence of successive thermal transitions [28, 66], as seen in Section 2.1.2 from a theoretical perspective: the memory effects and the elastic interaction kernel have only a limited effect on this scaling.

Then, we can define δt_f as coming from two sources of stochasticity as follows: the thermal and the spatial disorder, i.e., $\delta t_f = f(\delta t_{f,\text{thermal}}, \delta t_{f,\text{spatial}})$. In Section 1.1.4, we showed that one way to quantify the spatial heterogeneity in a system is by using the concept of entropy, S_j, in the sense of "lack" of information. Under this assumption, in the case of initially homogeneous systems (see Fig. 2.10a), we showed that S_j is maximized, with $S_{\text{homog}} = k_B \log N$, i.e., $\delta t_f \approx \delta t_{f,\text{thermal}}$, and is associated to a maximum spatial unpredictability as shown in the damage field just before failure (see Fig. 2.9a and Fig. 2.10b). In contrast, for simulations of samples with strong initial quenched disorder (see Fig. 2.10c) and different realizations of thermal disorder, but spatially identical samples, we show in Fig. 2.10d that the damage fields just before failure are very similar. In this case, S_j is small, as found by Ref. [71] with their structural entropy term, and the spatial disorder mainly controls the rupture, i.e., $\delta t_f \approx \delta t_{f,\text{spatial}}$. In other words, if we have any knowledge of the initial microstructure, it is possible to get a reasonable idea of the damage patterns and become spatially "deterministic". Fig. 2.9 shows that $\delta t_{f,\text{thermal}}$ decreases with increasing heterogeneity (see Fig. 2.9a). In contrast, this δt_f is larger in disordered

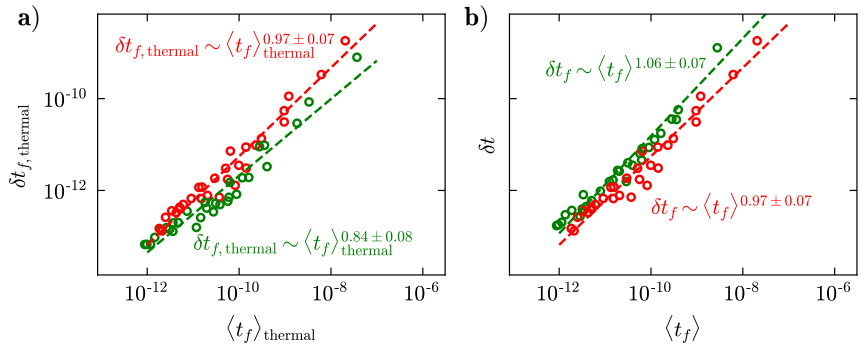


Figure 2.9. Dependence of the standard deviation on the mean failure time. Different realizations of the thermal disorder for **a)** a system with the same initial cohesion field (quenched disorder constant in space, thermal activation variable) and **b)** different variations of the cohesion field from the same initial disorder distribution (quenched disorder variable in space, thermal activation variable). Each dot corresponds to a set of experiments under the same T, $\sigma_{\text{appl}}/\sigma_{\text{ath}}$, and $\mu = 0.7$. Red: homogeneous, and green: strongly heterogeneous. Adapted from [1].

samples compared to homogeneous ones, due to $\delta t_{f,\text{spatial}}$ which is non-zero for heterogeneous samples (see Fig. 2.9b).

In Publication II, we studied the variability of creep lifetimes on sheets of paper obtained from tensile creep experiments to give additional insights with respect to this topic.

2.3.3 Implications of the heterogeneity and elastic interaction kernel on the interpretation of macro parameters

When conducting creep experiments on disordered materials under given conditions of temperature and load, it is common to use the "classical" Arrhenius law given in Eq. 1.1 to estimate an activation energy and consequently an activation volume V_{est} which is a parameter at the microscopic level [42], however, ignoring that the heterogeneity could affect such estimations. If one assumes that $t_f \sim \exp(V_{\text{est}}\Delta\sigma_{\text{macro}}/k_B T)$, then the estimated activation volume V_{est} is obtained by computing the slope in a semi-logarithmic plot as $V_{\text{est}} \approx \partial \log t_f / \partial(\Delta\sigma_{\text{macro}}/k_B T)$, where $\Delta\sigma_{\text{macro}} = (\sigma_{\text{ath}} - \sigma_{\text{appl}})(1 - \sin\phi)/2$ is a macro stress gap between a, supposedly known, athermal strength and the applied constant stress. $\Delta\sigma_{\text{macro}}$ is obtained from the MC rupture criterion (see Fig. 2.2b), with $\sigma_{3,\text{ath}} = \sigma_{3,\text{app}} = 0$, $\sigma_{1,\text{ath}} = \sigma_{\text{ath}}$ and $\sigma_{1,\text{appl}} = \sigma_{\text{appl}}$. Now, taking into account the initial quenched disorder, we know that $t_f \sim \exp(V\langle\Delta\sigma\rangle_0/k_B T_{\text{eff}})$, which considers the true V. From this, we can write:

$$\frac{V_{\text{est}}}{V} \approx \frac{T}{T_{\text{eff}}} \frac{\langle\Delta\sigma\rangle_0}{\Delta\sigma_{\text{macro}}}, \tag{2.14}$$

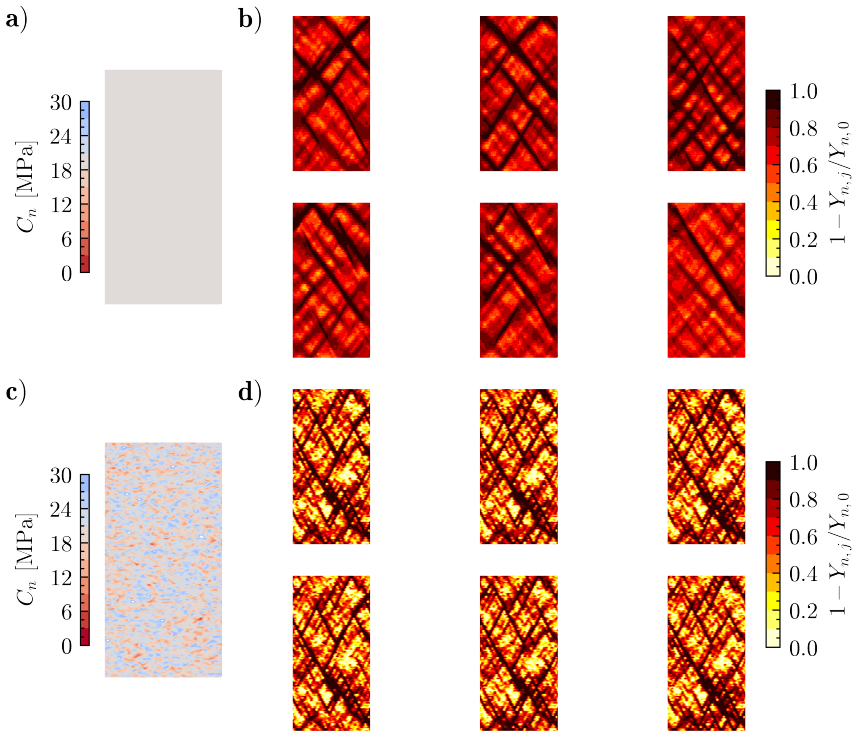


Figure 2.10. Initial quenched disorder introduced via the cohesion distribution for a **a)** homogeneous system and a **c)** strongly heterogeneous system, and its respective accumulated damage patterns at failure for a **b)** homogeneous system and a **d)** strongly heterogeneous system, when the kMC algorithm is launched six different times under the exactly same initial quenched disorder.

and replacing the empirical expression for T_{eff} (Eq. 2.13) into Eq. 2.14, we get:

$$\frac{V_{\text{est}}}{V} \approx \left[1 - \alpha \frac{1+\sin\phi}{\cos\phi} \frac{\delta_{\Delta\sigma,0}}{\langle\Delta\sigma\rangle_0}\right] \frac{\langle\Delta\sigma\rangle_0}{\Delta\sigma_{\text{macro}}},$$

or:

$$V \approx V_{\text{est}} \frac{\Delta\sigma_{\text{macro}}\cos\phi}{\langle\Delta\sigma\rangle_0\cos\phi - \alpha(1+\sin\phi)\delta_{\Delta\sigma,0}}. \tag{2.15}$$

From the numerical results, we can see that V_{est} overestimates the true value V. In general, $V_{\text{est}}/V > 1$, for both homogeneous and heterogeneous systems (see Fig. 2.11), explained by the initial quenched disorder and emergence of heterogeneity from the damage evolution. By simple inspection of Eq. 2.14, and knowing that $T \leq T_{\text{eff}}$, the only option to obtain the numerical observations is for the case $\langle\Delta\sigma\rangle_0 > \Delta\sigma_{\text{macro}}$, which is likely located in the tail of the stress gap distribution, $f\left(\Delta\sigma_{n,j} < \langle\Delta\sigma\rangle_0\right)$, thus showing the importance of the excitation spectrum in the definition of V.

Assuming no damage occurs during the athermal phase, $\langle\Delta\sigma\rangle_0 = \langle C\rangle\cos\phi - \sigma_{\text{appl}}(1-\sin\phi)/2$ and $\delta_{\Delta\sigma,0} = \delta C\cos\phi$, with. $\sigma_3 = \sigma_{3,\text{app}} = 0$ and $\sigma_1 = \sigma_{\text{appl}}$. Then

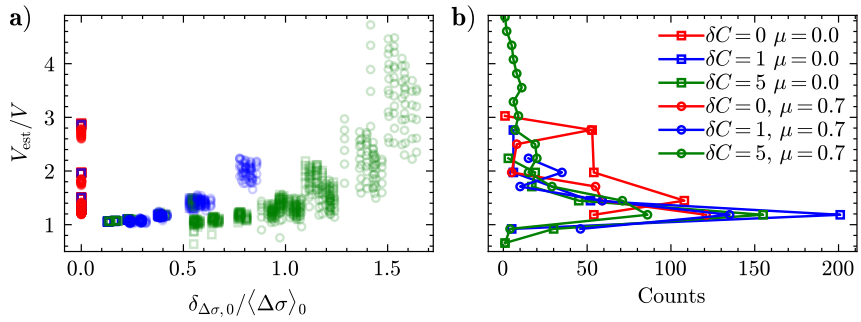


Figure 2.11. a) Dependency of V_{est}/V on the disorder level $\delta_{\Delta\sigma,0}/\langle\Delta\sigma\rangle_0$. **b)** Histogram of V_{est}/V.

V from Eq. 2.15 becomes:

$$V \approx V_{\text{est}} \frac{(\sigma_{\text{ath}} - \sigma_{\text{appl}})(1-\sin\phi)}{2\langle C\rangle\cos\phi - \sigma_{\text{appl}}(1-\sin\phi) - 2\alpha\delta C(1+\sin\phi)}. \tag{2.16}$$

which depends on the statistics of the cohesion C_n (mean and standard deviation) and on the friction coefficient ϕ (elastic interaction kernel).

3. Ranking persistence from a catalog of AE event times

From Chapter 2 based on Publication I, we achieved significant results that are worth noting in what follows. (i) We first studied theoretically a heterogeneous brittle material subjected to a constant load, with local damage thresholds expressed in terms of the MC criterion. While ignoring memory effects and elastic stress redistribution, we showed that the average creep lifetime follows an Arrhenius expression that depends on the inverse of the effective temperature T_{eff}, which increases with the initial quenched disorder, as found in Refs. [28, 29] using a DFBM, but additionally on the friction coefficient, which is a parameter of the nature of the elastic interaction geometry. (ii) Later, we implemented a numerical study, but this time including a more realistic elastic interaction kernel. We found an empirical expression for the dependence of t_f on T_{eff}; with T_{eff} depending on the level of heterogeneity and on the nature of the elastic interaction kernel. (iii) Our analysis also showed that $\delta t_f \sim \langle t_f \rangle$, indicating that the non-independence of the successive transitions has a limited effect on this scaling, i.e., δt_f has a similar Arrhenius law to that of $\langle t_f \rangle$. Additionally, (iv) we found that for strongly disordered systems, δt_f is mainly dependent on sample-to-sample variation of the initial quenched disorder, and not on thermal disorder, characteristic of homogeneous systems. Finally, we showed some implications of ignoring this disorder dependency in the computation of mechanical parameters, such as the activation volume.

In Publication II, we performed tensile creep experiments on sheets of paper, obtaining a sequence of AE event times t_{j+1} (see detailed information in Section 6.1), as well as fiber failure times from numerical simulations on a DFBM with thermal activation. We first show that the probability distribution of these times across a population of samples follows a lognormal distribution in accumulated form for all events. In addition, for individual experiments, the time series t_{j+1} shows non-Markovian rank persistence. Consequently, from these two observations emerges a power-law relation between the sequence of times and the creep lifetime, with an exponent that is a function of j. We demonstrate that this lognormal form and rank

persistence can be explained by a random multiplicative process with a random multiplier that depends on j. Finally, we show that the multiplicative process directly relates to the gap distribution (i.e., the excitation spectrum) and, using an extremal dynamics approach, allows us to reconstruct the minimum gap properties during the experiment.

3.1 Fiber bundle model with thermal activation

Here, we consider a very simple FBM with global load sharing—DFBM—[40, 49], including thermal activation of individual fiber—element—failures via a BKL–kMC algorithm [21, 84], explained in more detail in Section 6.2. The fiber bundle is a set of N parallel fibers, each one with constant Y_0, subjected to a constant initial stress $\sigma_{n,0}^{\text{appl}} = \sigma_{\text{appl}} = \text{F}_{\text{appl}}/N$, with F_{appl} the creep load. The initial quenched heterogeneity is implemented via the local strength σ_n, which follows a known probability distribution, e.g., uniform, Gaussian, or Weibull. In the model, the probability per unit time for an element n to be activated thermally at the $(j+1)$th transition is $\omega_{n,j+1}$ [53, 64] (akin to Section 1.1.4). After one fiber is thermally activated, it is eliminated. The time increment is chosen randomly following the procedure in Section 6.2, i.e., $\Delta t_{j+1} = -\langle \Delta t_{j+1} \rangle \ln u_{j+1}$, with average given by Eq. 1.3 [1, 53, 64]. The bundle deforms through the accumulation of successive thermal transitions, which can generate avalanches of athermal ruptures on some surviving elements due to load redistribution. After one transition ends, the applied stress on the surviving fibers becomes $\sigma_{n,j+1}^{\text{appl}} = \sigma_{\text{appl}}/(N - N_{\text{broken},j})$, with $N_{\text{broken},j}$ the accumulated number of broken fibers. The procedure continues until the bundle stability is exceeded, due to the last thermal activation or the final athermal avalanche.

3.1.1 Extremal dynamics emerges from thermal activation in the DFBM

Let us consider a very simple DFBM with global load sharing and thermal activation of individual fiber ruptures; the bundle is then subjected to $\sigma_{n,0}^{\text{appl}}$. Fibers have variable initial strengths, $\sigma_n \in [\sigma_{\min,0}, \sigma_{\max,0}]$, chosen from a uniform distribution, $f(\sigma_n) = (\sigma_{\max,0} - \sigma_{\min,0})^{-1}$. Using Eq. 1.3 and the theoretical approach from 2.1 applied to a uniform distribution of local strength (Eq. A29 in Publication I) and adapted to the DFBM, we derived an expression for the time increment after a given thermal activation considering the assumption that the excitation spectrum remains uniformly distributed after the elimination of fibers during the creep process, $f(\Delta\sigma_{n,j}) = f(\sigma_{n,j}) = (\sigma_{\max,j} - \sigma_{\min,j})^{-1}$:

$$\langle \Delta t \rangle_{j+1} = \frac{1}{(N - N_{\text{broken},j})\Omega_0} \frac{\Delta E_j / k_B T}{\sinh(\Delta E_j / k_B T)} \exp\left(\frac{\langle E_{\Delta\sigma} \rangle_j}{k_B T} \right), \tag{3.1}$$

with $\Delta E_j = 0.5V(\sigma_{\max,j} - \sigma_{\min,j})$, $\langle E_{\Delta\sigma}\rangle_j = 0.5V(\sigma_{\max,j} + \sigma_{\min,j}) - V\sigma_{\text{appl},j}$. The term $\sinh(\cdot) = 0.5[e^{(\cdot)} - e^{-(\cdot)}]$ is the hyperbolic sine. Notice that the term $\overline{\Delta Z_j}$ taking into account the initial quenched heterogeneity becomes $\overline{\Delta Z_j} = \Delta_j / \sinh \Delta_j$, with $\Delta_j = \Delta E_j / k_B T$. After replacing the expressions for ΔE_j and $\langle E_{\Delta\sigma}\rangle_j$, for the case of strong heterogeneity, $\sigma_{\max,j} \gg \sigma_{\min,j}$, in Eq. 3.1 we get:

$$\langle \Delta t \rangle_{j+1} = \frac{1}{(N - N_{broken,j})\Omega_0} \frac{V(\sigma_{\max,j} - \sigma_{\min,j})}{k_B T} \exp\left(\frac{V\Delta\sigma_{\min,j}}{k_B T}\right),$$

with $\Delta\sigma_{\min,j} = \sigma_{\min,j} - \sigma_{n,j}^{\text{appl}}$. We can see that the evolution of the minimum stress gap is crucial in the definition of the inter-event time, $\langle \Delta t \rangle_{j+1} \sim \exp(V\Delta\sigma_{\min,j}/k_B T)$. During primary creep, and under the assumption of large disorder, it is logical to think that the probability of an element to be chosen to generate a thermal transition is much larger on the excitation spectrum tail, i.e., the element with the minimum strength $\sigma_{\min,j}$ is the one with a higher chance to generate a transition compared to the element with the maximum strength $\sigma_{\max,j}$, i.e., the term $\sigma_{\max,j}$ will tend to remain constant, $\sigma_{\max,j} \approx \sigma_{\max,0}$ and the only term varying is $\sigma_{\min,j}$, which approximates to $\sigma_{\min,j} \approx \sigma_{\min,0} + (\sigma_{\max,0} - \sigma_{\min,0}) N_{broken,j} N^{-1}$. Then, $\langle \Delta t \rangle_{j+1}$ can be written as:

$$\langle \Delta t \rangle_{j+1} \approx \frac{2}{N\Omega_0} \frac{\Delta E_0}{k_B T} \exp\left(\frac{V\Delta\sigma_{\min,j}}{k_B T}\right). \tag{3.2}$$

We can see in Eq. 3.2 the importance of the minimum gap in the evolution of the inter-event times, demonstrating with this very simple case that the failure of the weakest elements governs each thermal transition, i.e., it agrees quite well with an extremal dynamics approximation [85–87]—relevant for low temperatures—. Although we use a uniform distribution of strength in this approach, we are confident that doing the same calculation for different types of strength distributions, e.g., lognormal, Weibull, we will obtain similar results if we take into account that this distribution tends to be positively skewed with concentration of the stress gaps and strength values near their minimum values.

3.1.2 Model used

In Section 3.1.1 we have shown that the extremal dynamics emerge from thermal activation in a DFBM, at least under the assumption of initial uniform distribution of fiber strengths. We also said that this assumption should apply to positively skewed distributions, recognizing that stress gaps concentrate around the minimum, i.e., a higher probability of thermal activation. For that reason, we tuned the initial quenched disorder to a more realistic case, i.e., Weibullian distribution of fiber strengths $f(\sigma_n)$, commonly used to describe materials strength [38, 40, 88], such as brittle ones [89, 90], as e.g., glass fibers [91], ceramics [92], or carbon fibers [93, 94].

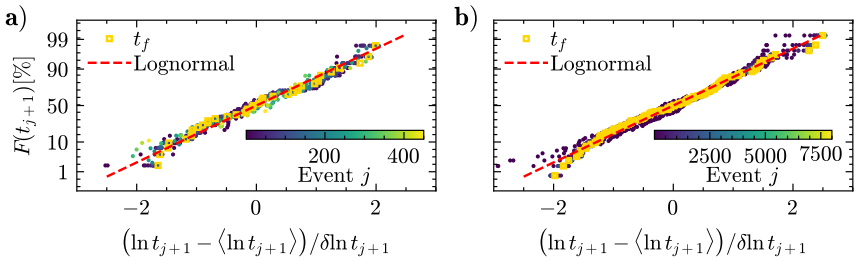


Figure 3.1. Evolution of the cumulative probability distribution for the AE time series t_{j+1} in the set of **a)** experimental tests and **b)** FBM simulations. The red dashed line corresponds to a perfect lognormal distribution. Adapted from [2].

Fibers have initial variable strengths σ_n, with shape and scale parameters ρ and λ, respectively. We implemented an increase in sample-to-sample variability to represent more realistic variability observed experimentally among a population of samples, e.g., failure times on paper sheets creeping under the same constant load can vary in three orders of magnitude [10], where microstructural disorder and processing variations coming from the papermaking process [95] define somehow the strength distribution. Other examples presenting such a sample-to-sample variability are glass fibers [91], rocks [14], concrete [96], or Kevlar filaments [57]. To reproduce this variability, we allow λ to fluctuate somewhat between simulations by adding a zero-mean Gaussian perturbation, η_k, in the kth simulation, i.e., $\lambda \to \lambda + \eta_k$. This variation reflects the heterogeneity of real materials, in which $\sigma_{\min,j}$ and $\langle \sigma_n \rangle$ vary from sample to sample.

3.2 Results

3.2.1 Cumulative probability distribution and rank persistence of event times

From the acquired time series from the experimental set, we found that the cumulative distribution of t_{j+1} over the population of creep tests ($k = 39$ samples) is universally lognormal (Fig. 3.1a):

$$F(t_{j+1}) = \frac{1}{2}\left[1 + \mathrm{erf}\left(\frac{\ln t_{j+1} - \langle \ln t_{j+1} \rangle}{\sqrt{2}(\delta \ln t_{j+1})}\right)\right], \tag{3.3}$$

where $F(t_{j+1})$ represents the cumulative probability distribution, $\delta \ln t_{j+1}$ and $\langle \ln t_{j+1} \rangle$ are the standard deviation and the mean value of the $(j+1)$th arrival time, t_{j+1}, of all the samples. It is also true for the series of thermal transition times obtained from the FBM simulations (see Fig. 3.1b). For a given experiment, t_{j+1} exhibits non-Markovian rank persistence, which differs for each experiment (see Fig. 3.2a), i.e., the relative ordering of

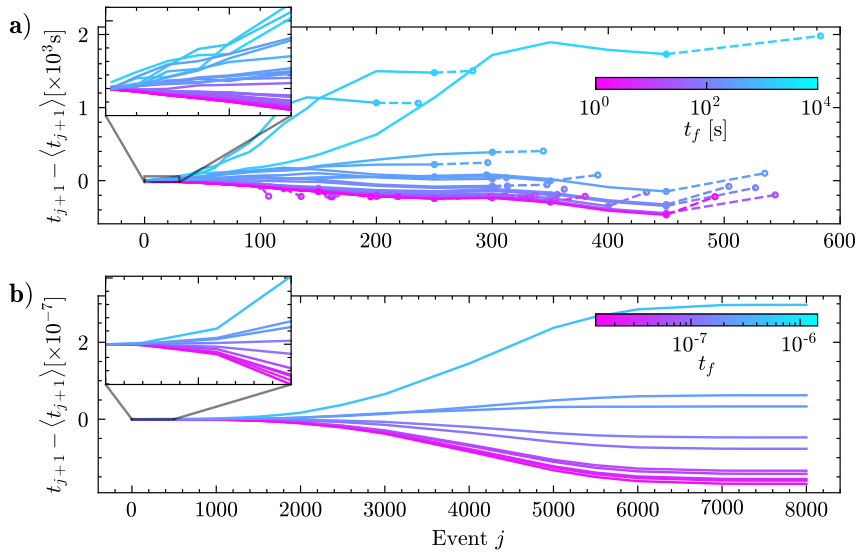


Figure 3.2. Non–Markovian trajectories for individual **a)** experimental tests and **b)** FBM simulations. The inset figure is a zoom of the trajectories at early events. The color palette is a function of the creep lifetime t_f. Adapted from [2].

trajectories is a sign of memory effect which is effectively established at the first AE events (or thermal transitions in the simulations), extended even to t_f (dashed lines in Fig. 3.2a). From the time series of fiber failures t_{j+1} in the FBM simulations (Fig. 3.2b) emerges a similar pattern, confirming that this rank memory is an intrinsic feature of the underlying dynamics. Non-Markovian trajectories are also present in the evolution of the minimum fiber strength, $\sigma_{\min,j}$, and the average fiber strength, $\langle \sigma_{n,j} \rangle$ (see Publication II).

One consequence of the lognormal distribution and the non-Markovian rank persistence of t_{j+1} for all js leads to the invariability of the corresponding ranking inside the cumulative distribution for a specific sample, i.e., $F(t_f) \approx F(t_{j+1})$:

$$\frac{\ln t_f - \langle \ln t_f \rangle}{\delta \ln t_f} \approx \frac{\ln t_{j+1} - \langle \ln t_{j+1} \rangle}{\delta \ln t_{j+1}},$$

which, after rearranging the terms, results in the emergence of a power-law relationship from the data obtained from AE arrival times (green dots and green squares in Fig. 3.3a) and the failure fiber times from the numerical simulations (green squares in Fig. 3.4a):

$$t_f \approx e^{\psi_{j+1}} t_{j+1}^{\theta_{j+1}}, \tag{3.4}$$

with power-law exponent θ_{j+1} and power-law prefactor ψ_{j+1} (green dots and green squares in Figs. 3.3b-c for experimental results and Figs. 3.4b-c

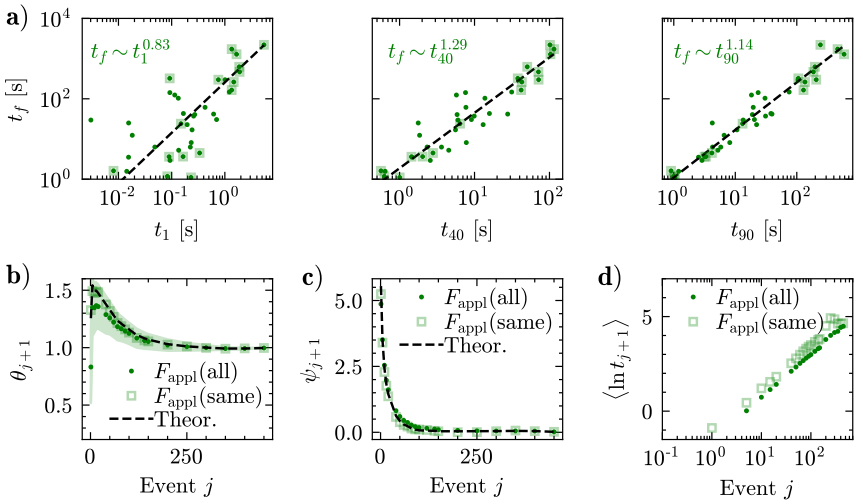


Figure 3.3. Experimental results. **a)** Dependency of the creep failure time t_f on the arrival times t_{j+1} for different events $(j+1) = \{1, 40, 90\}$ (in green) compared to the theoretical result obtained from Eq. 3.4 (black dashed line). Evolution with j of **b)** the power–law exponent θ_{j+1}, and **c)** the power–law prefactor ψ_{j+1}, obtained from a power-law fit (green) and comparison to the theoretical result from Eqs. 3.5 and 3.6 (black dashed line). Evolution along j of **d)** the mean of the logarithm of the population of event times $\langle \ln t_{j+1} \rangle$. Dots: full population of samples, Squares: subpopulation of samples (the ones subjected to the same creep load $\mathrm{F_{appl}} = 245\mathrm{N}$).

for numerical results) given by:

$$\theta_{j+1} = \frac{\delta \ln t_f}{\delta \ln t_{j+1}}, \tag{3.5}$$

$$\psi_{j+1} = \langle \ln t_f \rangle - \theta_{j+1} \langle \ln t_{j+1} \rangle, \tag{3.6}$$

with both terms, evolving with j. The theoretical expressions for θ_{j+1} obtained from Eq. 3.5 and ψ_{j+1} from Eq. 3.6, aligns quite well with the θ_{j+1} and ψ_{j+1} that fits the power-law dependency both in the experimental results (Figs. 3.3b-c) and in the numerical simulations (Figs. 3.4b-c) for any j. The only main difference between the theoretical and the fitted values of θ_{j+1} and ψ_{j+1} appears at an early number of events, with the theoretical being a bit larger than the fitted one. Surprisingly, the same results emerge if we choose a subpopulation of samples, e.g., those with the same applied creep load, $\mathrm{F_{appl}} = 245\mathrm{N}$ (see green squares in Fig. 3.3 and Table 6.1). Finally, we look for a dependence between the mean $\langle \ln t_{j+1} \rangle$ and the events j finding that there is a logarithmic dependence between these two terms, i.e., $\langle \ln t_{j+1} \rangle \sim \ln(j+1)$ (see Fig. 3.3d), showing the importance of the number of events in the power-law parameters shown above.

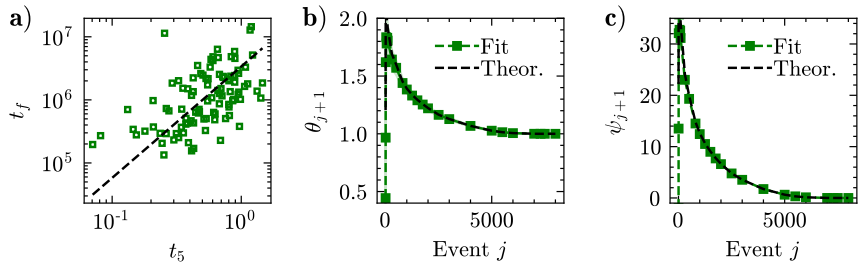


Figure 3.4. Numerical results. **a)** Dependency of the creep failure time t_f on the arrival times t_{j+1} at an early stage $(j+1)=5$ (green squares) compared to the theoretical result obtained from Eq. 3.4 (black dashed line). Evolution along j of **b)** the power–law exponent θ_{j+1}, and **c)** the power–law prefactor ψ_{j+1}, obtained from a power-law fit (green squares) and comparison to the theoretical result from Eqs. 3.5 and 3.6 (black dashed line).

3.2.2 Multiplicative random process connected to the tail of the excitation spectrum

We find that the lognormal form and non–Markovian trajectories for the sequence of times t_{j+1} could arise from a random multiplicative process [97, 98], related to e.g., lognormal multiplicative cascades of sea ice deformation [99] as well as irreversible deformation and accumulation of plastic strain in wood [100] and metals [101, 102]. The random multiplicative process is given by [97, 98]:

$$t_{j+1} = (1+r_j)t_j = \left[\prod_{m=1}^{j}(1+r_m)\right] t_1. \tag{3.7}$$

where $r_j > 0$ is the random multiplier evolving with j. For the naive case, assuming $r_j = \text{const.}$, the multiplicative process reproduces the two main findings here (lognormal distribution and non-Markovian trajectories). From our time series t_{j+1}, we can compute the mean multiplier over the population of experiments (red points for experiments in Fig. 3.5a) or simulations (green points for simulations in Fig. 3.5a) as $\langle r_j \rangle = \langle \Delta t_{j+1}/t_j \rangle = \langle t_{j+1}/t_j \rangle - 1$.

From Chapter 2 based on Publication I, we have shown the importance of the excitation spectrum $f(\Delta\sigma_{n,j})$ in defining the creep lifetime t_f, and in influencing the computation of micro mechanical parameters such as the activation volume V. Here, we go through this concept by demonstrating that the evolution of r_j can be related to the evolution of $f(\Delta\sigma_{n,j})$ (Fig. 3.5c), and most specifically its lower tail represented by the minimum gap $\Delta\sigma_{\min,j}$ (Fig. 3.5b). At the beginning, $\Delta\sigma_{\min,j}$ is low, but as low-strength elements are eliminated, $\Delta\sigma_{\min,j}$ increases as seen in Fig. 3.5b. In our model, thermal activation is implemented via a BKL–kMC thermal activation, where Δt_{j+1} is directly linked to $f(\Delta\sigma_{n,j})$ as already shown in Section 1.1.4. Nevertheless, from our theoretical analysis in Section 3.1.1, we found that the evolution of the waiting times Δt_{j+1} is controlled by

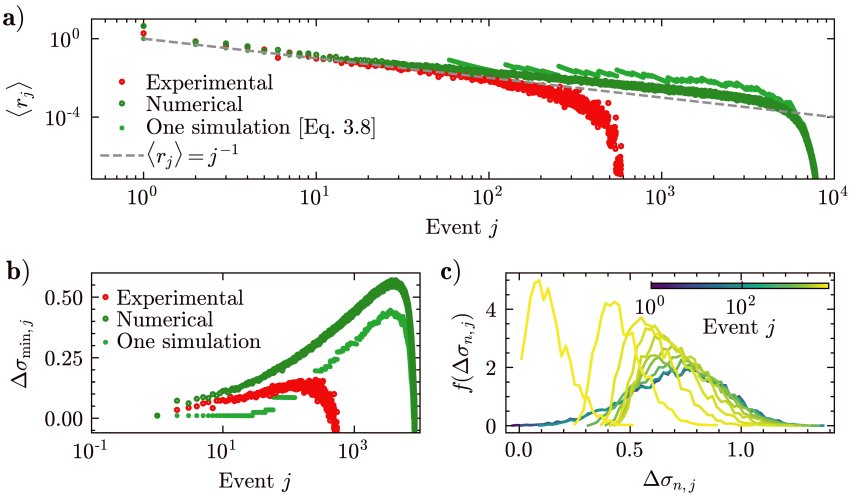


Figure 3.5. **a)** Evolution of the mean multiplier $\langle r_j \rangle = \langle \Delta t_{j+1}/t_j \rangle$ for the experimental results (red points), numerical results (green points), and theoretical result obtained from Eq. 3.8 in one FBM simulation (light green points). **b)** Evolution of the minimum gap for one simulation (light green points), and obtained solving $\Delta\sigma_{\min,j}$ in Eq. 3.8 from the experimental (red points) and numerical (green points) results. **c)** Evolution of the stress gap distribution for different values of j in one simulation. Adapted from [2].

the minimum energy barrier to be surpassed to get a thermal activation due to an extremal dynamics mechanism [85–87], i.e., after each thermal activation, the weakest element is eliminated. Then, it is possible to write $\langle \Delta t \rangle_{j+1} \approx 1/\max\{\omega_{n,j+1}\} \approx \Omega_0^{-1} \exp(V\Delta\sigma_{\min,j}/k_B T)$. In Fig. 3.5a we can see that for the first events, $\Delta\sigma_{\min,j}$ are roughly constant, showing a $r_j \sim j^{-1}$ behavior, valid for $j > 0$ to avoid a singularity. The tertiary creep regime is evident in the evolution of $\Delta\sigma_{\min,j}$ and $\langle r_j \rangle$, both of which decrease dramatically.

We can link r_j and $\Delta\sigma_{\min,j}$ by noting that: (i) we can write $t_j \approx j\overline{\Delta t_j}$, with $\overline{(\cdot)}$ denoting a temporal average over the history, and (ii) knowing that during primary creep, $r_j \sim j^{-1}$, we can assume that the first inter-event times do not show strong variation. In such a case, we can consider that there is not a huge difference between the arithmetic and the geometric average, or in other words, both means are of the same order of magnitude, i.e., $\overline{\Delta t_j} \approx \exp\left(\overline{\ln \Delta t_j}\right)$. Then, exchanging the arithmetic by the geometric mean, $\overline{\Delta t_j} \sim \exp(V\overline{\Delta\sigma_{\min,j-1}}/k_B T)$, and replacing in the term $r_j = \Delta t_{j+1}/\left(j\overline{\Delta t_j}\right)$, we obtain:

$$r_j \sim \frac{1}{j} \exp\left(\frac{V\Delta\sigma_{\min,j} - V\overline{\Delta\sigma_{\min,j-1}}}{k_B T}\right) \tag{3.8}$$

showing that r_j presents a power-law decrease as a function of j, with a cutoff defined by the difference between the current, $\Delta\sigma_{\min,j}$, and the temporal average minimum gap, $\overline{\Delta\sigma_{\min,j-1}}$. Eq. 3.8 recovers quite well the numerical results of the random multiplier as seen in Fig. 3.5a (light green

line). Additionally, solving for $\Delta\sigma_{\min,j}$ in Eq. 3.8 by an iterative process, we obtain the evolution of the minimum gap from the experimental results (red line in Fig. 3.5b) showing a reasonable evolution. Additionally, we compare the value $\Delta\sigma_{\min,j}$ obtained (i) over the population of simulations (green line in Fig. 3.5b) and (ii) from one FBM simulation itself (light green line in Fig. 3.5b). (i) and (ii) show very similar patterns reaching secondary creep at a similar j.

The results presented in this chapter open the door to a more general failure-inference framework based on the damage history obtained from AE time series. It could be improved to enable early predictions of failure, as will be evaluated in Chapter 4 using a Bayesian inference approach based on Publication III. Another possible utility is in the classification of damage regimes based on the AE sequence characteristics.

4. Bayesian inference for early prediction of creep failure times

From Chapter 3, based on tensile creep experiments on sheets of paper as well as DFBM simulations, we achieved very important outcomes to take into account. From a sequence of AE event times (experimental) and thermally activated fiber failure times (numerical), t_{j+1}, (i) we show that the cumulative probability distribution of these time series for a given AE event/thermal transition over a representative number of samples follows a universal lognormal distribution. (ii) the sequence of times t_{j+1} shows non-Markovian behavior as well as rank persistence. (iii) Combining (i) and (ii) emerges a power-law relationship between t_{j+1} and t_f, with an exponent and a prefactor varying with j and dependent on the statistical characteristics of $\ln t_{j+1}$ (mean and standard deviation). (iv) We demonstrate that (i) and (ii) can arise from a random multiplicative process. (v) Finally, we show that the random multiplier r_j from the multiplicative process has a connection to the gap distribution—specifically its tail— and using an extremal dynamics mechanism, it allows us to reconstruct and show the existence of the minimum gap in creep experiments.

In Publication III, we propose an early-prediction of creep lifetime from a Bayesian inference approach via Markov chain Monte Carlo (MCMC) methods on an evolving landscape from tensile creep experiments on sheets of paper. In a first approach, we used the concept of master curve behavior, which accounts for the full temporal evolution of the deformation under constant load, thereby allowing predictions of t_f only after the minimum strain rate is exceeded. In a second approach, using knowledge from a sequence of AE event times, we implement sequential Bayesian updating to infer the evolving barrier statistics in each sample and propagate uncertainty to a posterior predictive distribution for the time-to-failure $t_f - t_{j+1}$. In this last approach, we obtain much earlier predictions for most experiments. It provides an uncertainty-aware bridge from microscopic barrier evolution to macroscopic creep curves and quantitative lifetime forecasts. Additionally, Publication III gives additional theoretical insights into the results obtained in Publication II, from which we could say that the time-dependent distribution of activation barriers controls deformation: stress lowers barriers,

while irreversible rearrangements deplete the weakest spots and reshape the low-barrier tail, i.e., the minimum stress gap.

4.1 Bayesian inference model

We implement the Bayesian inference through MCMC methods implemented in the PyMC library [103], more specifically using the no-U-turn sampler (NUTS) [104]. The inference is performed by drawing 5000 samples per chain, running four independent chains to check for convergence, and setting an acceptance target of 90% to reduce the number of divergences in complex posterior distributions. In what follows, we will refer to the posterior data sets generated by Bayesian inference as Bayesian samples, and the tensile creep experiments performed ($k = 39$ tests) as samples.

4.1.1 Master curve behavior

Description of the model—For brittle creep, the master curve, onto which all individual creep curves can be scaled, consists of combining the main concepts of the empirical creep phenomenology (see Section 1.1.1) in one single expression [10], summarized as a model for the strain rate $\dot{\varepsilon}(t)$ as follows:

$$\dot{\varepsilon}(t) = A\left(\frac{t}{t_f}\right)^{-p} + B\left(\frac{t_f - t}{t_f}\right)^{-\beta} \tag{4.1}$$

where A is a constant prefactor for the transient creep behavior, t is a continuous time (and different from the sequence of event times t_{j+1}), and B is a constant prefactor for the tertiary creep. To reproduce the known relation between the time of the minimum strain rate, $t_{\min}$ and the failure time t_f [10, 33], B is fixed so that the minimum strain rate, $\dot{\varepsilon}_{\min} = \min\{\dot{\varepsilon}(t)\}$, occurs at $t = t_{\min} = \kappa_{\min} t_f$, where $\kappa_{\min} < 1$. Then, according to the last conditions, it is possible to obtain an expression for B. One can compute the derivative of Eq. 4.1, and solve for B when $t = t_{\min}$, i.e. $d^2\varepsilon/dt^2(t = t_{\min}) = 0$,

$$B = A\frac{p}{\beta}\frac{(1-\kappa_{\min})^{1+\beta}}{(\kappa_{\min})^{1+p}}, \tag{4.2}$$

where for the simple case of logarithmic creep during the transient and accelerated phase, $p = \beta = 1$, the prefactor B and the strain rate $\dot{\varepsilon}$ become $B = Ap\beta^{-1}(\kappa_{\min}^{-1} - 1)$ and $\dot{\varepsilon} = A(t/t_f)^{-1} + Ap\beta^{-1}(\kappa_{\min}^{-1} - 1)(1 - t/t_f)^{-1}$, respectively. In our specific material and geometry, we know that $\kappa_{\min} \approx 0.83$ [10]. It means that the strain-rate $\dot{\varepsilon}$ starts to accelerate very late in the creep process. From this, we can already guess that a prediction of failure time from the master curve will be difficult and arrive too late.

The master curve behavior potentially provides a way to predict the failure time for each creep test after $\dot{\varepsilon}_{\min}$. From the primary creep behavior, A and p can be easily inferred, and if one observes a minimum value in the strain

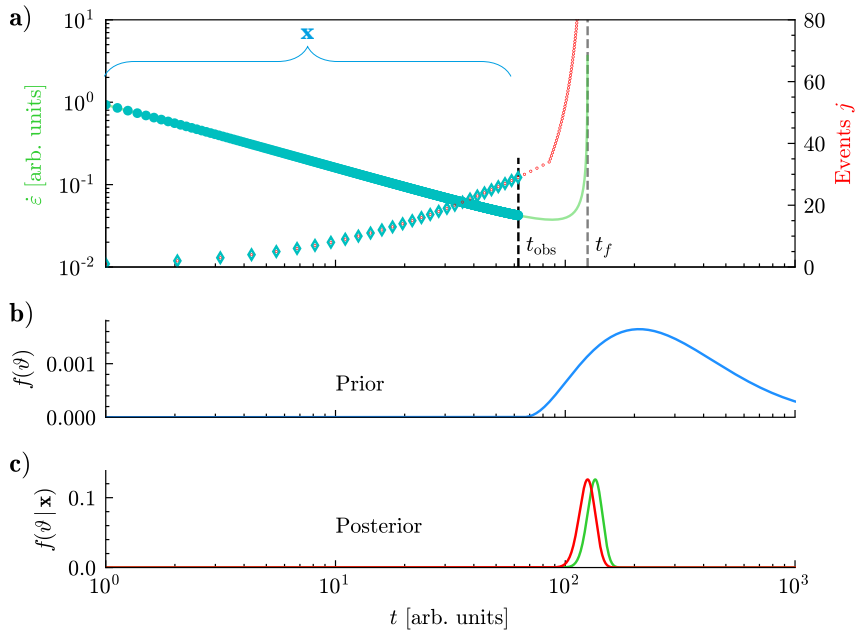


Figure 4.1. Schematic description of the prediction process through Bayesian inference. **a)** Temporal evolution of the strain rate $\dot{\varepsilon}$ (lightgreen) and cumulative number of AE event j (red). The data $\mathbf{x}$ come from the strain data set and the catalog of AE events read up to a time t_{obs}, and based on this data, one tries to predict the failure time t_f. **b)** Prior distribution $f(\vartheta)$, with $\vartheta = t_f$ in this example. **c)** By conditioning on the data $\mathbf{x}$, one arrives at a posterior distribution, $f(\vartheta\,|\,\mathbf{x})$, from the strain data (ligthgreen) and AE events (red). Adapted from [3].

rate, the Monkman–Grant relationship [22] then allows one to estimate t_f. In practice, determining the minimum in a noisy strain-rate signal during an experiment is very difficult and yields significant uncertainty. Given the need to quantify uncertainty, Bayesian inference is a natural tool for this task. It is based on Bayes' theorem [66, 103]

$$f(\vartheta\,|\,\mathbf{x}) = \frac{\mathscr{L}(\mathbf{x}\,|\,\vartheta) f(\vartheta)}{\displaystyle\int_{-\infty}^{\infty} \mathscr{L}(\mathbf{x}\,|\,\vartheta) f(\vartheta)\,\mathrm{d}\vartheta}, \tag{4.3}$$

where $\vartheta = \{A, p, \kappa_{\min}, \beta, t_f\}$ denotes the set of parameters of the model, $\mathbf{x}$ the observed data—for example the observed strain or strain rate data up to $t < t_{\text{obs}}$—, $f(\vartheta)$ is the prior distribution of the parameters, $\mathscr{L}(\mathbf{x}\,|\,\vartheta)$ the likelihood, $f(\vartheta\,|\,\mathbf{x})$ the posterior distribution of the parameters. The integral, known as the marginal distribution, is taken over all the possible parameter values. If ϑ is discrete, the integral is replaced by $\sum_\vartheta \mathscr{L}(\mathbf{x}\,|\,\vartheta) f(\vartheta)$. The basic idea is to start with reasonable estimates of the parameter distributions, priors $f(\vartheta)$, and to predict the parameter distributions conditional on the observed data, posteriors $f(\vartheta\,|\,\mathbf{x})$. This idea, applied to the prediction of creep lifetime, is illustrated in Fig. 4.1.

Using this framework for creep prediction involves taking strain data up to

time $t = t_{\text{obs}}$, using it as the data $\mathbf{x}$ for Bayesian inference, and obtaining the posterior prediction for the failure time t_f. For this, the model of Eq. 4.1 is used, by integrating it up to time t_{obs}, i.e. $\varepsilon_m(t_{\text{obs}}) = \varepsilon_m(t_0) + \int_{t_0}^{t_{\text{obs}}} \dot{\varepsilon}(t)\,\mathrm{d}t$, where $\varepsilon_m(t_0)$ is the strain at t_0. In addition, a Gaussian variability with standard deviation δ_ε around this model is allowed by choosing the likelihood

$$\mathscr{L}(\mathbf{x}\,|\,\vartheta) = \prod_{m=1}^{j_{\text{obs}}} \frac{1}{\sqrt{2\pi\delta_\varepsilon^2}} \exp\left(-\frac{1}{2\delta_\varepsilon^2} \left[\varepsilon_m - \varepsilon_m(t_0) - \int_{t_0}^{t_m} \dot{\varepsilon}(t)\,\mathrm{d}t \right]^2 \right) \tag{4.4}$$

where the index m runs through all the discrete (t_m, ε_m) data points and j_{obs} is the last index satisfying $t_{j_{\text{obs}}} \leq t_{\text{obs}}$. It essentially means that the inference aims to minimize the variability δ_ε while still accounting for the observed data. As the marginal distribution in Eq. 4.3 is not analytically tractable in the general case, sampling from the posterior distribution is done using MCMC methods. For priors, we chose uniform distributions for the exponents, $0.5 \leq p \leq 1$ and $0.8 \leq \beta \leq 2$, common ranges of values for these exponents in the studied material [10, 11], and a lognormal distribution for A, with mean and standard deviation equal to 10^{-3}. As we know that failure occurs at time $t_f > t_{\text{obs}}$ and additionally wanted the inference to catch the earliest signs of tertiary creep onset, we chose a lognormal prior for the time–to–failure, $t_f - t_{\text{obs}}$, with a mean equal to $t_{\text{obs}}(\kappa_{\text{min}}^{-1} - 1)$, obtained from the assumption that we are exactly at t_{min}, and a standard deviation equal to half the mean. Note that the average of the posterior failure time, $\langle t_f^{\text{pred}} \rangle$ is obtained by adding t_{obs} to the computed average of the posterior, $\langle (t_f - t_{\text{obs}})^{\text{pred}} \rangle$, i.e., $\langle t_f^{\text{pred}} \rangle = t_{\text{obs}} + \langle (t_f - t_{\text{obs}})^{\text{pred}} \rangle$.

Prediction at final stages of creep—From the strain-based prediction using the master curve approach, for each creep test, we obtain Bayesian samples from the parameters posterior, yielding different full strain-rate curves, as shown in Fig. 4.2a. A more useful metric is the evolution of the prior and posterior distributions as a function of t_{obs}, as shown in Fig. 4.2b, where we illustrate the behavior of their means and the standard deviations for one representative experiment. The prior is always defined just after t_{obs}, with mean value $t_{\text{obs}}\kappa_{\text{min}}^{-1}$ (see blue errorbars in Fig. 4.2b). Initially, when there is no sign of an inflection point in the strain rate, the posterior mean is much higher than the prior, and the distribution is wider. However, when the inflection point appears, the posterior assumes a narrower shape and converges to the real t_f (see lightgreen errorbars in Fig. 4.2b). Looking at this over all the experiments, we can define a precision metric, $\delta t_f^{\text{pred}}/t_f^{\text{true}}$—narrowness of the posterior distribution–, and an accuracy metric $\| t_f^{\text{true}} - \langle t_f^{\text{pred}} \rangle \| / t_f^{\text{true}}$ —relative distance of the posterior mean to the true value— and consider a prediction successful if the accuracy is below a given tolerance. By varying the tolerance (Fig. 4.2c), we see that indeed predictability arises after t_{min} when the tolerance is lower than 0.1, meaning that this method can predict t_f, in most of the experiments,

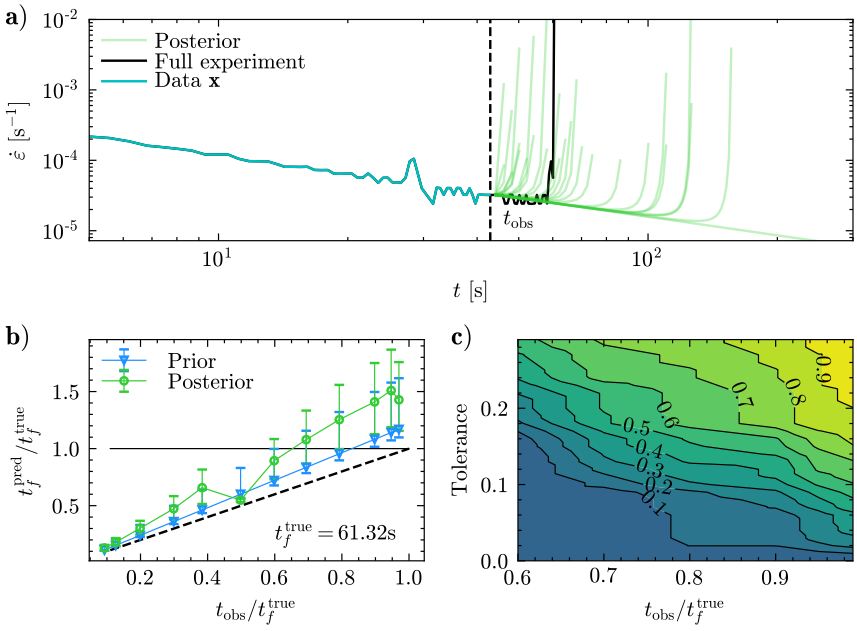


Figure 4.2. a) An example of the failure time prediction from the strain signal. **b)** The evolution of the posterior distribution of the failure time (blue) as one changes the prediction time t_{obs} for a representative example. The green symbols show the prior distributions for the failure time for comparison. **c)** The proportion of predicted experiments for a given tolerance and prediction time t_{obs}, with a zoomed-in view below. Here, a 10 % precision is chosen. Adapted from [3].

when around 10 % of the lifetime is left. However, it is useful as a baseline prediction.

4.1.2 Acoustic emission correlations

Definition of the variables from acoustic emission measurements—In addition to the strain data, one can also observe acoustic emission events. From Publication II, it is observed in a population of creep experiments that we have a rank-persistence of the AE event times defining a power law dependency of the creep lifetime t_f as a function of the event times t_{j+1} as given by Eq. 3.4 in Section 3.2.1, $t_f = e^{\psi_{j+1}} t_j^{\theta_{j+1}}$, where $\psi_{j+1} = \langle \ln t_f \rangle - \theta_{j+1} \langle \ln t_{j+1} \rangle$, and $\theta_{j+1} = \delta \ln t_f / \delta \ln t_{j+1}$. These two variables depend on the means and standard deviations of the times t_{j+1} over the population of creep tests, which we do not know in isolated experiments.

Furthermore, we know that the rank-persistence is coming from the multiplicative process nature of the event times defined in Eq.3.7, $t_{j+1} = t_1 \prod_{m=1}^{j} (1 + r_m)$, where $r_m \sim R_0 m^{-1}$, where R_0 is a prefactor accounting for the sample-to-sample variation among samples (see Section 3 and Publication II to see more details about sample-to-sample variability). It works well for primary creep, with r_m decreasing rapidly as tertiary creep begins,

as shown in Section 3.2.2. As mentioned, r_m accounts for sample-to-sample variation in the prefactor R_0 across k experiments, with mean $\langle R_0 \rangle$ and standard deviation δR_0. Then, by taking the logarithm of Eq. 3.7 and replacing the first-order Taylor expansion $\ln[1+(\cdot)]$ around zero, $\ln[1+(\cdot)] \approx (\cdot)$, one gets:

$$\ln t_{j+1} = \ln t_1 + R_0 \sum_{m=1}^{j} \frac{1}{m}, \tag{4.5}$$

where the summation has known asymptotics, $\sum_{m=1}^{j} m^{-1} \sim \gamma + \ln j$, where $\gamma \approx 0.577\ldots$ is the Euler-Mascheroni constant. Then, replacing it in Eq. 4.5,

$$\ln t_{j+1} = \ln t_1 + R_0 \left[\gamma + \ln j\right] = \ln t_2 + R_0 \ln j, \tag{4.6}$$

and computing the mean and standard deviation over j, one gets:

$$\langle \ln t_{j+1} \rangle = \langle \ln t_1 \rangle + \langle R_0 \rangle \left[\gamma + \ln j\right] \tag{4.7}$$

$$\delta \ln t_{j+1} = \sqrt{(\delta \ln t_1)^2 + (\delta R_0)^2 \left[\gamma + \ln j\right]^2} \tag{4.8}$$

Note that the expression for $\langle \ln t_{j+1} \rangle$ is in agreement with the observed logarithmic dependence, $\langle \ln t_{j+1} \rangle \sim \ln(j+1)$, shown in Section 3.2.1 (see Fig. 3.3d). Thus, replacing $\delta \ln t_{j+1}$ in Eq. 3.5, θ_{j+1} becomes:

$$\theta_{j+1} = \frac{\theta_1}{\sqrt{1 + \varphi_1^2 [\gamma + \ln j]^2}} \tag{4.9}$$

with $\theta_1 = \delta \ln t_f / \delta \ln t_1$, the value of the exponent function at the first event. $\varphi_1 = \delta R_0 / \delta \ln t_1$ is the ratio between the standard deviations over the specimens population of the sample-to-sample variable and the logarithm of the first event time; it could be interpreted as a variable characterizing the initial heterogeneity. Eq. 4.9 goes to zero as $j \to \infty$. However, we know that θ_{j+1} goes to unity close to failure at some finite $j = \mathcal{N}$, so we can simply write $\theta_1 \approx \sqrt{1 + \varphi_1^2 [\gamma + \ln \mathcal{N}]^2}$ and θ_{j+1} becomes:

$$\theta_{j+1} \approx \sqrt{\frac{1 + \varphi_1^2 [\gamma + \ln \mathcal{N}]^2}{1 + \varphi_1^2 [\gamma + \ln j]^2}}, \tag{4.10}$$

and in the same way $\langle \ln t_f \rangle$ could be approximated as:

$$\langle \ln t_f \rangle \approx \langle \ln t_1 \rangle + \langle R_0 \rangle \left(\gamma + \ln \mathcal{N}\right). \tag{4.11}$$

This enables the computation of the prefactor

$$\psi_{j+1} = \left(\langle \ln t_1 \rangle + \gamma \langle R_0 \rangle\right)(1 - \theta_{j+1}) + \langle R_0 \rangle \left(\ln \mathcal{N} - \theta_{j+1} \ln j\right). \tag{4.12}$$

With these expressions, one arrives at functions $\theta_{j+1} = \theta_{j+1}(\mathcal{N}, \delta R_0, \delta \ln t_1)$, where $\mathcal{N}$ roughly corresponds to the total number of AE events during the creep test, and $\psi_{j+1} = \psi_{j+1}(\langle \ln t_1 \rangle, \langle R_0 \rangle, \mathcal{N}, \theta_{j+1})$. Both terms only depend on

the distribution of three quantities: $\mathcal{N}$, R_0, $\ln t_1$ (or $\ln t_2$ if we use the equivalent definition of Eq. 4.6). Note that two of these quantities, $\ln t_1$ and R_0, are indicators of the initial quenched heterogeneity of the system [1, 28, 29] and of the sample-to-sample variability [2, 95], respectively. Now, we will make some initial guesses for the priors of these variables. For example, one can imagine that a good approximation for the first event captured by the AE sensor occurs at around 1 second, then $\langle \ln t_1 \rangle \approx 0$. For φ_1, we could assume that $\delta \ln t_1$ is of the same order of magnitude as δR_0; then we could say that $\langle \varphi_1 \rangle \approx 1$. The only term we do not have any a priori idea of is the total number of AE events $\mathcal{N}$ recorded by the sensor. Then, it is reasonable to expect that unrealistic prior assumptions about the parameter set might limit the results.

Barrier landscape trajectories and non-Markovian variability—We have shown that the multiplicative process described by Eq. 3.7 provides a direct connection between AE event time series and the stress gap landscape—at least its tail—. Under this interpretation, r_m encodes the successive exploration of local failure strengths, i.e., early AE events have information of the activation of the weakest spots, while later events explore progressively higher barriers. Then, R_0 could be interpreted as a parameter that controls the exploration rate within the excitation spectrum and therefore reflects the intrinsic sample-to-sample variability.

A crucial idea is that such a sample–to–sample variability resides in the barrier distribution itself, not only in stochastic realizations drawn from a fixed distribution. It means that each sample has its own disorder ensemble, characterized by a set of parameters, $\vartheta = \{R_0, t_1, \mathcal{N}\}$, and therefore follows a distinct trajectory through the barrier landscape. It describes the rank-persistence ordering of event times, t_{j+1}, across samples, which underlies the empirical power-law expression shown in Eq. 3.4.

As a consequence, creep dynamics is intrinsically non-Markovian, i.e., it exhibits memory effects. The statistics of future events depend on which parts of the barrier distribution have already been depleted and on the particular disorder ensemble realized in the sample. This type of memory is qualitatively different from that of standard depinning models with fixed disorder—even with history-dependent driving [105]—. Instead, it reflects a progressive selection within a sample-specific population of failure thresholds. Eq. 3.4 can thus appears as a projection of these sample-specific trajectories onto the (t_{j+1}, t_f) plane, where the coefficients $(\theta_{j+1}, \psi_{j+1})$ come from the population statistics of the set of parameters, $(\mathcal{N}, R_0, t_1)$. While these population quantities are not a priori known for a single experiment, the observed AE sequence constrains the admissible region of this parameter space, allowing for inferring the trajectory of an individual sample.

In practice, however, these trajectories are not directly visible in macroscopic observables such as strain; for example, different realizations with

distinct distributions for $(R_0, t_1, \mathcal{N})$ can produce very similar strain histories until late times. It explains why the master-curve-based prediction becomes accurate only after the minimum strain rate is reached. The AE signal, by contrast, probes microscopic dynamics and therefore contains information about the trajectory from early times onward.

Self-consistent Bayesian inference—To apply these ideas to actual prediction, we again set up a Bayesian inference-based prediction scheme. The crucial point here is to treat these population statistics as inherent parameters, $\vartheta = \{t_1, R_0, \mathcal{N}\}$, and infer them from the AE time series. Taking the natural logarithm of Eq. 3.4, $\ln t_f \approx \psi_{j+1} + \theta_{j+1} \ln t_{j+1}$, and remembering that arrival times follow a universally lognormal distribution in cumulative form as shown in Section 3.2.1, this idea of a self-consistent prediction is easily formalized by the Gaussian likelihood for $\ln t_f$,

$$\mathscr{L}(\mathbf{x}\,|\,\vartheta) = \prod_{j=1}^{j_{\mathrm{obs}}} \frac{1}{\sqrt{2\pi\delta^2_{\ln t_f}}} \exp\left(-\frac{[\langle \ln t_f \rangle - \psi_{j+1} - \theta_{j+1} \ln t_{j+1}]^2}{2\delta^2_{\ln t_f}} \right), \tag{4.13}$$

which essentially minimizes the scatter in the predictions of $\ln t_f$, denoted by $\delta_{\ln t_f}$, across all j values up to j_{obs}, with the observed data $\mathbf{x}$ the event times up to t_{obs}. The main difference from the strain-based prediction is that we are not trying to fit the model, $t_f \approx e^{\psi_{j+1}} t_{j+1}^{\theta_{j+1}}$ (Eq. 3.4), as well as possible, using the functional forms of θ_{j+1} and ψ_{j+1}, but are just trying to have self-consistent failure time predictions.

To set the priors, we assume that the first event is captured roughly at one second as mentioned above, and based on Publication II, $\langle R_0 \rangle \sim 1$ (see Fig. 3.5a). The sample-to-sample variability is then expressed in the first event time, t_1, so for the combined quantity, $\varphi_1 = \delta R_0 / \delta \ln t_1$, we assume $\delta \ln t_1 \sim \delta R_0$. In this way, we consider a Gaussian prior for φ_1 characterized by a mean of 1 and a standard deviation of 0.2. Finally, $\mathcal{N}$ was chosen to follow a lognormal distribution with mean 250 and standard deviation 50. Here, $\mathcal{N}$ and $\ln t_1$ are the most important quantities to consider when defining the prior distributions, as these terms depend on the AE signal and the thresholding made to such a signal, i.e., they are dependent on the piezoelectric sensor, the acquisition frequency, and parameters used on the thresholding method to obtain the catalog of AE events.

Creep failure prediction at early stages—Using self-consistent Bayesian inference, we can obtain much better predictions of failure times at early stages than strain-based predictions (see Fig. 4.3a for a representative experiment). The posterior distribution for t_f already roughly matches the actual creep lifetime at around 10% of the lifetime, i.e., significantly before t_{min}, thereby far surpassing the predictive capabilities based on the strain signal (see Fig. 4.3a). To quantify the distance between the true failure time, t_f^{true}, and the posterior distribution from the Bayesian inference, we

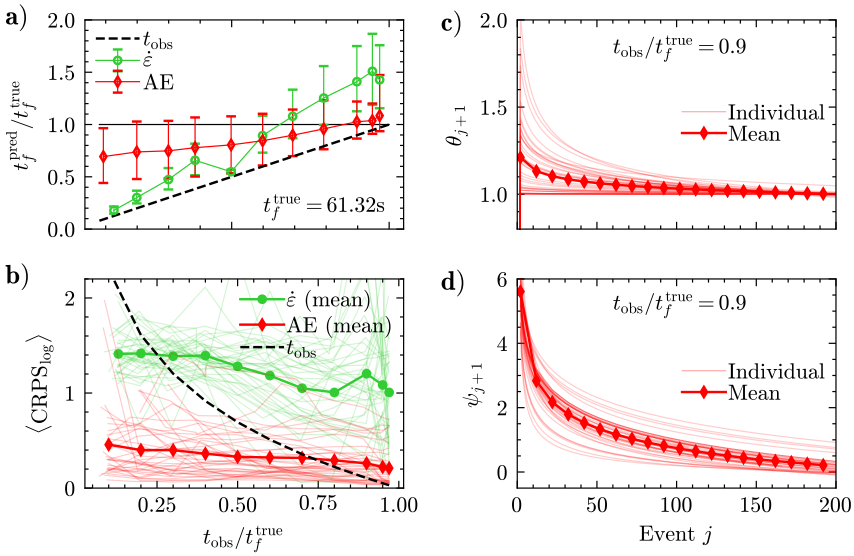


Figure 4.3. a) The evolution of the posterior distribution of the creep lifetime, $t_f^{\text{pred}} \sim f(t_f, \mathbf{x})$, as one changes the observed time t_{obs} for one experiment. **b)** The prediction score (CRPS_{log}) for all the experiments, where the bold lines represent the mean value for all the individual trajectories. Evolution of **c)** the power–law exponent θ_{j+1}, and **d**) the power–law prefactor ψ_{j+1}, for all the experiments taking the prediction at $t_{\text{obs}}/t_f^{\text{true}} \leq 0.9$. Lightgreen: the master curve approach, and red: the AE correlations approach. Adapted from [3].

compute the continuous ranked probability score (CRPS) [106] in log-space as

$$\text{CRPS}_{\text{log}} = \int_0^{\infty} \frac{\left[F(t_{\text{pred}}) - H(\ln t_{\text{pred}} - \ln t_f)\right]^2}{t_{\text{pred}}} \mathrm{d}t_{\text{pred}} \tag{4.14}$$

where $F(t_{\text{pred}})$ is the empirical cumulative distribution function of the posterior. Thus, the CRPS metric shows that the self-consistence Bayesian inference from the AE approach reflects a better score CRPS_{log} from much earlier stages (red lines in Fig. 4.3b) than the strain–based prediction (lightgreen lines in Fig. 4.3b), for which reasonable prediction occurs just after happens the minimum strain rate or when failure is imminent.

The individual trajectories for each sample can directly be seen by plotting the evolution of the inferred power-law exponent θ_{j+1} (Fig. 4.3c), and power-law prefactor ψ_{j+1} (Fig. 4.3d), for each experiment, based on the posterior means obtained at $t_{\text{obs}} \leq 0.9 t_f^{\text{true}}$. Even though they are based on population-level correlations, interpretation using our Bayesian inference scheme yields a unique trajectory for each experiment in these quantities. The individual inferred curves for θ_{j+1} and ψ_{j+1} are in agreement with the ones obtained in Section 3.2.1 (see Fig. 3.3b-c).

To identify a possible limitation on the choice of priors, most specifically for the parameter $\mathcal{N}$, we performed additional numerical tests by modifying

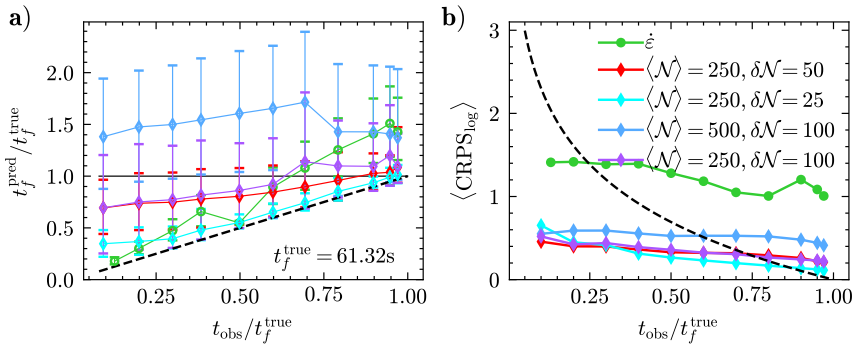


Figure 4.4. Influence of the prior of $\mathcal{N}$ on the predictions. **a)** The evolution of the posterior distribution of the creep lifetime as one changes the observed time t_{obs} for one experiment. **b)** Prediction score (CRPS_{log}) for all the experiments. The dashed line corresponds to the naive case $t_f^{\text{pred}} = t_{\text{obs}}$. Adapted from [3].

the prior for $\mathcal{N}$, which we find to be the most influential latent variable in the model. We fixed the shape of the prior as lognormal. Still, we shifted the prior mean to twice and to half of the studied case, while keeping the standard deviation fixed at 20% of the mean (see blue and cyan lines in Fig. 4.4), and one more case with the standard deviation fixed at 40% of the mean (see purple line in Fig. 4.4). We observed some effect of the prior choice on the posteriors obtained (see Fig. 4.4a), with the standard deviation of the posterior lifetime, δt_f^{pred}, being proportional to $\delta\mathcal{N}$. Nevertheless, the average prediction score over all creep tests, $\langle \text{CRPS}_{\text{log}} \rangle$, shows a similar result for all cases, being better than the strain-based prediction case (see Fig. 4.4b). Then, we note that the prior is expected to be material- and measurement-specific. Factors such as the AE sensor characteristics, detection thresholds, and signal processing protocols can influence the effective mapping between observed events and the latent variables. In practice, we could obtain a good initial guess for the priors from a limited set of preliminary experiments. Importantly, these need not be full creep-to-failure tests. A second option could be to perform monotonic loading experiments, which may provide approximate order-of-magnitude information on the total number of AE events. Another option is to measure the number of AE events during the loading phase before the creep onset and multiply it by, e.g., a factor of 10.

The predictive power of acoustic-emission timing can be traced to the evolution of the underlying barrier landscape governing thermally activated failure events. In Publication II we showed that the multiplier of the multiplicative process directly connects AE timing to the evolution of the minimum activation barrier. The relation $t_f = e^{\Psi_{j+1}} t_{j+1}^{\theta_{j+1}}$ is a coarse-grained representation of the evolving minimum barrier in the system. Because the rank-persistent, lognormal statistics of t_{j+1} reflect the initial position

of a sample in the barrier landscape, the eventual failure time is already encoded in the earliest events. In Publication III, we exploit this structure by inferring the latent parameters of the barrier landscape—encoded in the evolution of ψ_{j+1} and θ_{j+1}—through a self-consistent Bayesian scheme that minimizes the dispersion of t_f predictions across events. In this sense, acoustic emission does not merely provide empirical precursors of failure, but constitutes an indirect probe of the evolving barrier landscape governing creep rupture. The early predictability demonstrated here reflects the fact that the system's position in this landscape is effectively set at the very onset of damage accumulation.

5. Conclusions

This dissertation focused on the theoretical analysis of creep rupture using concepts from statistical physics, along with experimental data and numerical simulations. In general, this thesis provides supplementary theoretical background for understanding the physical phenomena that describe creep rupture in heterogeneous materials. It provides additional insight into the full creep process and, consequently, into creep failure. The main findings from this work are presented below.

In Chapter 2, we conducted a theoretical and numerical study of the creep failure time of a bidimensional brittle material with the Mohr–Coulomb criterion as its local yield criterion, which is a function of the stress state, the cohesion C_n, and the friction coefficient μ. We achieved significant results that are worth noting. From a theoretical perspective, we assume a material subjected to a constant load, in which the local distribution of cohesion defines the initial quenched heterogeneity. By ignoring memory effects and the elastic stress redistribution, we showed that the average creep lifetime, $\langle t_f \rangle$, follows an Arrhenius expression dependent on the inverse of an effective temperature T_{eff}, which increases with the initial quenched disorder—same conclusion as found by Refs. [28, 29] using a democratic fiber bundle model—, but additionally on the friction coefficient, μ, which is a representation of the nature of the elastic interaction geometry. Later, from a numerical study using a progressive damage model with thermal activation implemented via a Bortz–Kalos–Lebowitz–kinetic Monte Carlo algorithm, and including a more realistic elastic interaction kernel, we found an empirical dependence between t_f and T_{eff}, with T_{eff} dependent not only on the level of heterogeneity, but on the nature of the elastic interaction kernel. The key observation from this part is that $\langle t_f \rangle$ and T_{eff} are strongly dependent on the evolving excitation spectrum—also called stress gap distribution—$f(\Delta\sigma_{n,j})$, which accounts for the effects of initial disorder and the friction coefficient on the evolution of the energy barrier landscape. Its evolution proved to be relevant to the results presented in Chapters 3 and 4.

The numerical analysis in Chapter 2 also showed that the variability of the failure time from sets of simulations done under the same initial conditions—same temperature T, creep load $\sigma_{\text{appl}}/\sigma_{\text{ath}}$, and heterogeneity level δC—is proportional to its average, $\delta t_f \sim \langle t_f \rangle$. It indicates that the non-independence, or memory effect, of the successive thermal transitions has a limited effect on this scaling. Nevertheless, such a memory effect plays a key role in the evolution of the tail of the excitation spectrum, with important consequences in the creep lifetime, as shown in Chapter 3. Additionally, we found that in strongly disordered systems, δt_f is mainly determined by sample-to-sample variation in the initial spatial organization of the disorder rather than by thermal disorder. In contrast, thermal disorder controls δt_f in homogeneous systems. Finally, we showed some implications of ignoring this disorder dependency in the computation of mechanical parameters in laboratory creep tests, such as the activation volume.

From Chapter 3, based on tensile creep experiments on sheets of paper as well as democratic fiber bundle model simulations, we achieved very important outcomes to take into account. From a sequence of AE event times obtained experimentally, and thermally activated fiber failure times coming from the numerical simulations, t_{j+1}, we have shown that the cumulative probability distribution of these time series—even for the failure times t_f—for a given AE event / thermal activation over a representative number of samples follows a lognormal distribution, and additionally the times t_{j+1} show non-Markovian rank persistence. From these findings emerges a power-law expression, $t_f = e^{\psi_{j+1}} t_j^{\theta_{j+1}}$, with an exponent θ_{j+1} and a prefactor ψ_{j+1}. Both terms vary with j and are dependent on the statistical characteristics of $\ln t_{j+1}$, i.e., its mean and standard deviation. A key result here was that, from the cumulative lognormal distribution and rank persistence, a random multiplicative process characterized by a random multiplier r_j can arise, which is connected to the tail of the excitation spectrum. This connection was derived theoretically from an extremal dynamics mechanism that accounts for memory effects on the evolution of AE events. From this finding, we were able to reconstruct and show the existence of the minimum stress gap in creep experiments. Another key observation from this chapter is that the time series' rank persistence opens the door to an alternative approach to predicting the failure of brittle materials under creep loads, as evaluated in Chapter 4 from a Bayesian inference perspective.

In Chapter 4, we propose an early-prediction of creep lifetime from a Bayesian inference approach via Markov chain Monte Carlo methods on an evolving landscape from tensile creep experiments on sheets of paper, with main results explained in Chapter 3. We have presented a Bayesian inference method for predicting creep rupture using macroscopic information from strain data and acoustic emission event timing. In the first approach,

we used the concept of master curve behavior, which accounts for the full temporal evolution of deformation under constant load, yielding predictions of t_f only after the minimum strain rate is exceeded. In the second approach, using a sequence of AE times, we implement sequential Bayesian updating to infer the evolving barrier statistics for each sample and to propagate uncertainty into a posterior predictive distribution for the time-to-failure. The predictability arises mainly from the non-Markovian creep dynamics, in which the statistics of future events depend on both the depletion of weak barriers—the tail of the excitation spectrum—and the sample-specific disorder ensemble. Thus, the samples follow individual, ranked trajectories, as shown in Chapter 3. Additionally, it implies that the inferred curves of the power law exponent and prefactor, θ_{j+1} and ψ_{j+1}, also reflect individual trajectories, which is different from the single curves obtained from the full set of experiments, as shown in Chapter 3. By treating the population-level quantities determining the creep lifetime as latent variables and inferring them self-consistently from partial AE sequences, our Bayesian scheme converts early microscopic activity into a posterior distribution for the failure time with quantified uncertainty. The resulting predictions become accurate well before the strain-based predictions and, more importantly, at the early stages of the creep experiment. It demonstrates that the earliest damage events already encode information about time-to-failure through the minimum gap of each individual sample. More generally, the approach offers a method for early failure forecasting in systems governed by collective damage dynamics and finite-time singularities—e.g., from seconds to years—, in which failure signals from macroscopic quantities arrive late or are noisy, while event-level activity preserves microscopic information about the evolution of disorder. Finally, it could be interesting to perform an extensive analysis of the set of parameters used to implement Bayesian inference and identify the admissible region of this parameter space, as well as possible limitations in the choice of the prior distributions.

The fundamental challenge in failure prediction is that early-time observations can provide information about the lifetime but present significant uncertainty. In contrast, accurate predictions typically become possible only close to failure, when intervention is no longer feasible. The trajectory-based inference perspective shown in Chapter 4 is quite remarkable. It was based on just the arrival times t_{j+1} from the catalog of AE events–and associated waiting times Δt_{j+1}—, and not on other variables such as the AE energies $E_{j+1}^{(\mathrm{AE})}$, or the spatial localization of these events. For example, beyond laboratory creep, it should be relevant to the geophysical rupture phenomena where precursory event sequences provide a window into the underlying instability and failure forecasting, as e.g., landslides and slope creep [107–109], rockfalls [110, 111], serac collapses [112–114], and volcanic eruptions [115, 116]. In such geophysical objects, most predictions

arise from fitting-based estimates of physical models describing the rupture process, for which the Bayesian approach could provide additional insights for better predicting rupture. One crucial parallel between these geophysical systems and experimental creep lies in the presence of time-dependent deformation under a roughly constant load—e.g., in landslides, rockfalls, or serac collapses, such a load is their own weight.

Some possible limitations of applying the Bayesian approach to geophysical systems arise from the fact that the performed creep tensile experiments cover maximum creep lifetimes of $\sim 10^3$ seconds, which is a finite-time singularity much lower than in actual geophysical systems. Thus, it should be interesting to perform additional tests to extend the observed physical phenomena to additional orders of magnitude. Another imaginable limitation is that these systems are primarily subjected to compressive forces. Thus, it could be interesting to perform compressive creep experiments on, e.g., rocks, concrete, or ice, and extend the findings from tensile to compressive creep. Even though, in geophysical systems, precursory event sequences provide a window into the underlying instability and failure, from time to time and for short periods, they may also be subjected to external dynamical forces, e.g., due to the presence of water, which could add critical aspects to prediction. It is not evaluated in our approach, and it might be interesting to study possible effects at an experimental scale.

6. Devices and methods

6.1 Experimental methods

For Publication II and Publication III, we performed experimental tests and obtained data on the temporal evolution of force, displacement, and amplitudes from AE signals. This section will show the relevant information describing the experimental methods.

6.1.1 Samples and athermal testing

The material used is ordinary office paper, which is a two-dimensional material composed of a random fiber network [10, 11]. The default dimensions are $0.1 \times 0.05 \times 0.0001$ m (height×width×thickness) [10]. Industrial paper has two main directions defined by the fabrication process, the 'machine direction' and the 'cross direction'. The results shown in the present document come from tests on 'machine direction' office paper, or the direction along the wire. In what follows, global stress $\sigma(t)$ is the ratio between the applied force $\mathrm{F}(t)$ and the cross-sectional area $\mathscr{S}$:

$$\sigma(t) = \frac{\mathrm{F}(t)}{\mathscr{S}}, \tag{6.1}$$

with $\mathscr{S} = \mathrm{width} \times \mathrm{thickness}$, and strain refers to the global engineering strain,

$$\varepsilon(t) = \frac{l(t) - l_0}{l_0} = \frac{\Delta l(t)}{l_0}, \tag{6.2}$$

with $l(t)$ the temporal evolution of the length parallel to the applied force, and $l_0 = \mathrm{height}$, the initial length of the sample. $\Delta l(t)$ denotes the displacement. In creep tests, $\sigma(t) = \sigma_{\mathrm{appl}} = \mathrm{const.}$

The tensile breaking force threshold comes from 14 monotonic tension tests, and its average value is $\mathrm{F}_{\mathrm{ath}} \approx 0.27$ kN (Fig. 6.1a). Its equivalent stress is $\sigma_{\mathrm{ath}} \approx 53.4$ MPa or $\sigma_{\mathrm{ath}} \approx 5.3 \mathrm{kN m^{-1}}$ in force per unit length (Fig. 6.1b). The respective Young's modulus is $Y_0 \approx 5.2$GPa (Fig. 6.1c). The

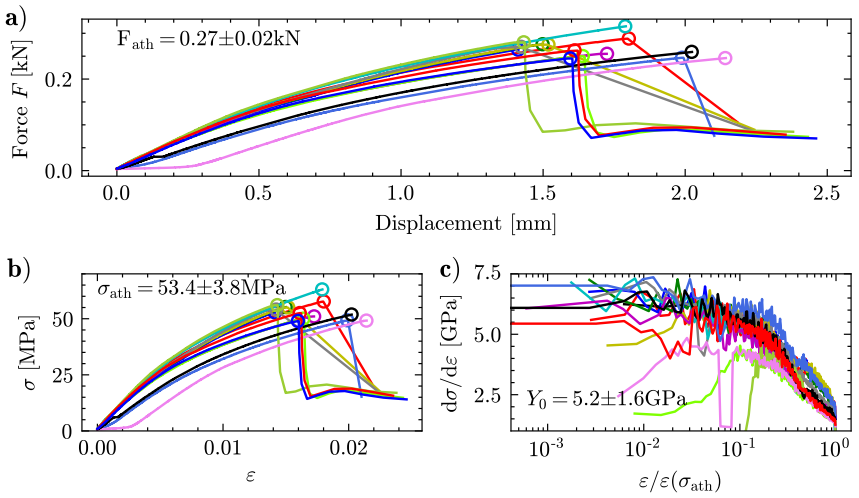


Figure 6.1. Athermal experiments to obtain an average strength σ_{ath} at macroscale. **a)** Force – displacement curve and identification of maximum applied force (dots). **b)** stress – strain curve ($\sigma - \varepsilon$) and identification of the maximum applied stress σ_{ath} (dots). **c)** Tangent modulus $d\sigma/d\varepsilon$ as a function of the strain scaled by its value at σ_{ath}, $\varepsilon/\varepsilon(\sigma_{ath})$. The Young's modulus is defined as the average of the tangent modulus for $\varepsilon/\varepsilon(\sigma_{ath}) < 10^{-2}$

areal weight, or grammage, was not measured, but common values for the specific samples are between $75 - 80 \text{gm}^{-2}$ [10, 11, 95]. Notice that we obtain these values for 'machine direction' paper, and they are between two and three times the values for 'cross direction' paper [10].

6.1.2 Creep testing

We performed 39 tensile creep experiments at room temperature on an Instron ElectroPuls E1000 testing machine with a force capacity of 1 kN. According to the breaking tensile thresholds obtained in section 6.1.1, we have chosen creep loads $F_{appl} < 0.3$ kN, given in Table 6.1. The precision of F_{appl}, i.e., the standard deviation of the mechanical noise around the loading target, is $\sim 10^{-4}$N ($\sim 0.1\%$ around F_{appl}) as shown in Fig. 6.2c. To reach the constant load, the force increases linearly from zero to the target F_{appl} in 10s, in a similar way as described in Ref. [10]. To obtain relevant data, we monitored the force and the displacement with an acquisition frequency of 1 kHz, resulting in the strain obtained with Eq. 6.2 (see Fig. 6.2a). To reduce noise and obtain a smooth curve for the strain rate, $\dot{\varepsilon}$, when computing the time derivative of the strain, we used a simple linear interpolation to obtain an interpolated time t_i and an interpolated strain ε_i. We compute the time derivative of the interpolated strain $\dot{\varepsilon}_i$ (see Fig. 6.2b) with a central difference approach as:

$$\frac{d\varepsilon_i}{dt} \approx \frac{\varepsilon_{i+1} - \varepsilon_{i-1}}{t_{i+2} - t_i} \approx \frac{\varepsilon_{i+1} - \varepsilon_{i-1}}{2\Delta t}, \tag{6.3}$$

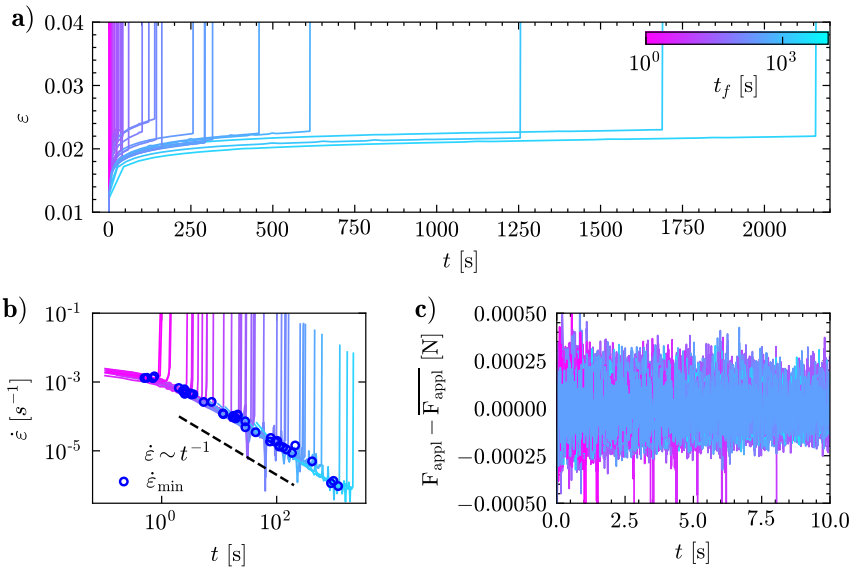


Figure 6.2. Creep behavior in all the experiments. **a)** Temporal evolution of the strain ε. **b)** Temporal evolution of the strain rate $\dot{\varepsilon}$ and identification of the minimum strain rate $\dot{\varepsilon}_{\text{min}}$ (blue dots). **c)** Mechanical noise around the loading target.

with $\Delta t = t_{i+1} - t_i = \text{const.}$, and the sub-index i varying from one to the total number of interpolation points. Similarly, we can obtain the minimum strain rate by looking for the time when the second time derivative of the strain is zero, $\mathrm{d}^2\varepsilon(t_{\text{min}})/\mathrm{d}t^2 = 0$. Then, using a finite differences approach, the second derivative becomes:

$$\frac{\mathrm{d}^2\varepsilon_i}{\mathrm{d}t^2} \approx \frac{\varepsilon_{i+1} - 2\varepsilon_i + \varepsilon_{i-1}}{(2\Delta t)^2}. \tag{6.4}$$

Furthermore, when Eq. 6.4 is zero, we obtain the minimum strain rate (see blue dots in Fig. 6.2b). Additionally, the creep lifetime t_f for each test is defined as the time when the strain rate diverges, i.e., $t_f = t(\dot{\varepsilon} \to \infty)$. We found that the strain rate during primary creep is consistent with logarithmic creep, $\dot{\varepsilon} \sim t^{-1}$. The values for t_f vary over three orders of magnitude, $1 < t_f < 2 \times 10^3$, even when different tests are performed under the same applied creep load (see Table 6.1), illustrating the sample-to-sample variability resulting from the heterogeneous distribution of the samples [10].

6.1.3 Acoustic emission

The Acoustic Emission (AE) was captured by a wideband piezoelectric sensor (WSα AE sensor from Physical Acoustics Corporation) in contact with the sample to follow the microcracking [117, 118]. The AE system consists of the piezoelectric microphone, an amplifier for the voltage signal produced by the piezoelectric sensor (60 dB), and a high-frequency acquisition system

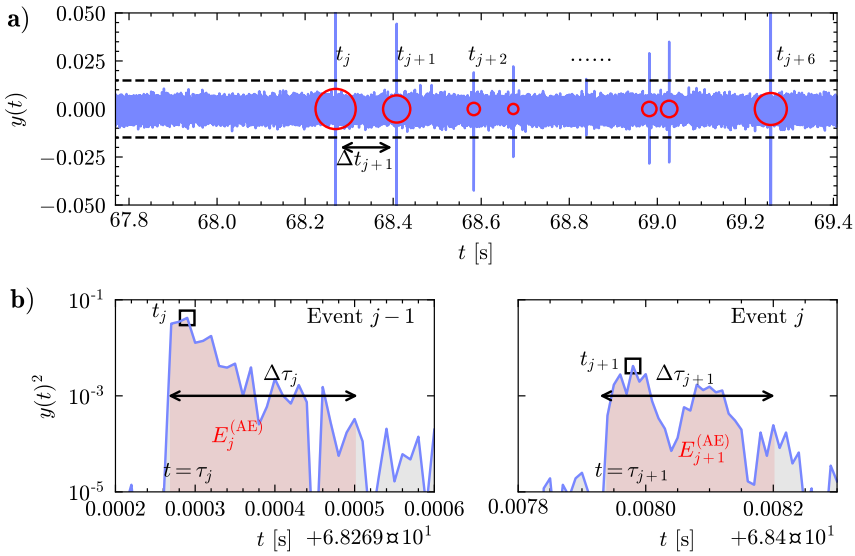


Figure 6.3. Computation of the event time t_{j+1} and its radiated energy $E_{j+1}^{(AE)}$. **a)** Continuous signal obtained from the AE sensor (light blue) in one creep test ($F_{appl} = 270$N) showing the amplitude $y(t)$. Location of the different event times t_{j+1}, the waiting time Δt_{j+1}, and the energy radiated by each one of the events $E_{j+1}^{(AE)}$ (red circles), where the different sizes indicate the magnitude of the event. The black dashed line is the chosen amplitude threshold $A_{thres} = 1.48 \times 10^{-2}$. **b)** For two consecutive events, j and $j+1$, the identification of the respective parameters characterizing that event: the coda length $\Delta\tau_{j+1}$, the event time t_{j+1} (black square) and the energy $E_{j+1}^{(AE)} = \int_{\tau_{j+1}}^{\tau_{j+1}+\Delta\tau_{j+1}} y^2 dt$ (light red region).

(100 kHz) [119, 120]. The continuous AE signals are represented via the temporal evolution of the signal amplitude $y(t)$ (given in V) as shown in Fig. 6.5a.

As the creep experiment progresses, local microfracturing occurs in the form of intermittent bursts, similar to microseismic activity observed in rock mechanics or earthquake physics [77, 81]. It means that the continuous signal may be transformed into discrete events [117]. To define such discrete AE events, we first applied a thresholding method. The threshold y_{thr} was chosen in order to be above the noise level of the signal, i.e., $|y(t)| > y_{thr} \approx 1.48 \times 10^{-2}$ (black dashed line in Fig. 6.3a). At this point, we obtained portions of a continuous signal above y_{thr}, each portion defining an event $j+1$ ($j = 0, \ldots, \mathcal{N}$) (see Fig. 6.3b). Inside an individual event we could identify several parameters [81]: (i) the event time t_{j+1}, defined as the time at which the peak amplitude occurs (black square in Fig. 6.3b), (ii) the event duration $\Delta\tau_{j+1}$, also known as coda length and (iii) an estimate of the energy radiated by the event $E_{j+1}^{(AE)}$ (red circles in Fig. 6.3a light-red

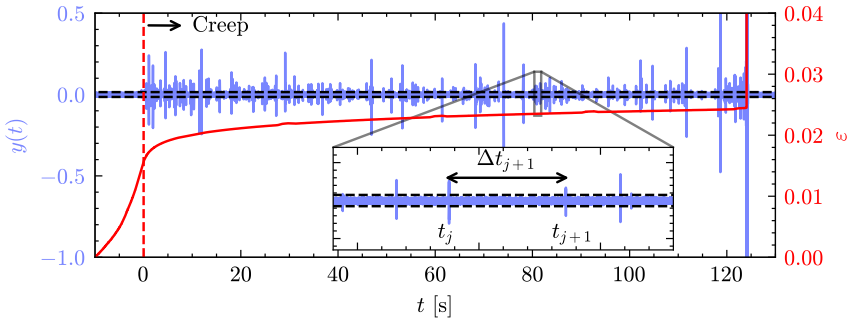


Figure 6.4. Example of the continuous signal obtained from the AE sensor (light blue) and evolution of the displacement (red) in one single creep test with $F_{\text{appl}} = 270\text{N}$. The black dashed line is the chosen amplitude's threshold $A_{\text{thres}} = 1.48 \times 10^{-2}$. Adapted from [2].

region in Fig. 6.3b), defined by:

$$E_{j+1}^{(\text{AE})} = \int_{\tau_{j+1}}^{\tau_{j+1}+\Delta\tau_{j+1}} y(t)^2 \mathrm{d}t, \tag{6.5}$$

with $\tau_{j+1} \leq t_{j+1} \leq \tau_{j+1} + \Delta\tau_{j+1}$. Finally, the pair $(t_{j+1},\ E_{j+1}^{(\text{AE})})$ defines a catalog of events, with the time between two successive events defining an inter-event time $\Delta t_{j+1} = t_{j+1} - t_j$ (see Fig. 6.3a).

The deformation and AE data are measured in close succession (AE acquisition is launched first). Nevertheless, they display a small time shift between the two signals, which comes from different initial and final acquisition times. To synchronize the two signals, we look for the time when the deformation rate and the AE rate diverge; i.e., the failure time, which is the same in both cases. Then, subtracting the initial acquisition time from the failure time yields the actual acquisition time for both signals. In this way, the two signals synchronize just by adding the time gap to the time of the AE signal, which is just the difference between the two real acquisition times (see Fig. 6.4).

Influence of threshold y_{thr} on the events counting–In the thresholding method used to obtain the events, we assumed the threshold was above the noise level. However, defining the threshold depends heavily on the experimentalist performing the data analysis; e.g., if one chooses a value below the noise level, the number of events $\mathcal{N}$ will be too large. In the opposite case, if the threshold is too conservative, one might miss events [121]. Then, how do we ensure that the chosen threshold is an adequate value? To solve this question, we implemented different values of y_{thr} to obtain the total number of events $\mathcal{N}$, i.e., $0.01 \leq y_{\text{thr}} \leq 0.02$ (see dashed lines for different cases in Fig. 6.5a). Across all experiments, we observed that $\mathcal{N}$ decreases as y_{thr} increases. We could identify two zones: a non-divergent zone and a divergent zone. When $0.014 < y_{\text{thr}} < 0.020$, the variation of $\mathcal{N}$

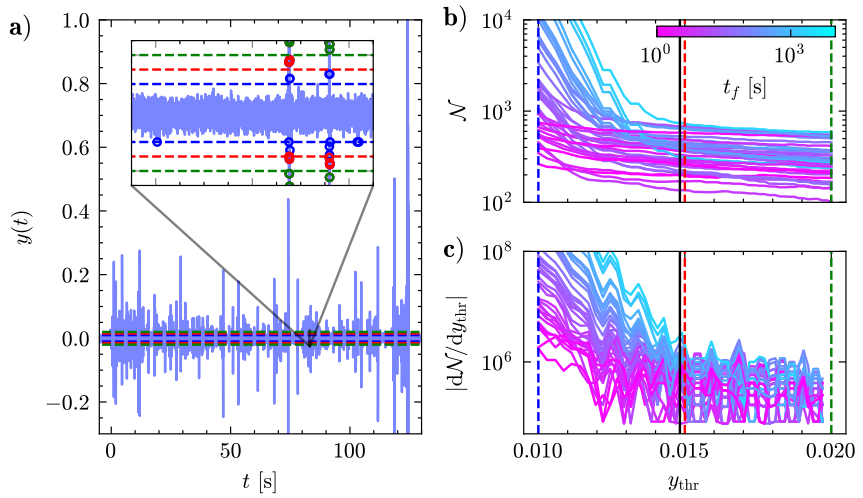


Figure 6.5. a) Example of AE signal $y(t)$ in an individual creep experiment. Inset plot: zoom-in of the signal in a time interval and identification of different amplitude thresholds y_{thr} (dashed lines), where the dots are the amplitudes $|y(t)| > y_{thr}$. **b)** Number of events $\mathcal{N}$ leading to failure as a function of y_{thr} for all the creep experiments and its **c)** derivative $d\mathcal{N}/dy_{thr}$ to identify y_{thr} leading to divergence of the number of events. The black continuous line is the threshold implemented to obtain the catalog of events.

is small (see Fig. 6.5b), where it looks like the decrease follows a linear shape, $\mathcal{N} \sim -10^5 y_{thr}$ ($|d\mathcal{N}/dy_{thr}| \approx 10^5$ in Fig. 6.5c). In the divergent region, $y_{thr} < 0.014$, the derivative $|d\mathcal{N}/dy_{thr}|$ rises exponentially as $y_{thr} \to 0$ (see Fig. 6.5c), which is the case when the threshold is inside the noise level. We see that the chosen value, $y_{thr} = 0.0148$ (black line on Figs.6.5b,c), is a suitable value for the thresholding method.

6.2 Thermal activation via a BKL–kMC algorithm

For Publication I and Publication II, we performed numerical simulations using PDM (see Section 2.2.1) or DFBM (see Section 3.1). We obtained data on the temporal evolution of stress, strain, and the number of events, among other variables. In order to describe the time-dependent deformation associated with creep behavior, we introduce thermal activation and a physical timescale via a Bortz–Kalos–Lebowitz kinetic Monte Carlo algorithm (BKL–kMC) [64, 84]. The goal is to thermally activate damage events at the local scale at rates corresponding to the relevant individual processes. The jump rate of each element n follows an Arrhenius expression [64, 84]:

$$\omega_{n,j+1} = \Omega_0 \exp\left[-\frac{E_{n,j}}{k_B T}\right]. \tag{6.6}$$

Eq. 6.6 represents the probability $p(E_{n,j+1})$ per unit time for element n to undergo the thermal activation during the $(j+1)$th transition, i.e.,

Test	F_{appl} [N]	t_f [s]	$\mathcal{N}$	Test	F_{appl} [N]	t_f [s]	$\mathcal{N}$
147	220.0	8.14	107	93	246.0	164.63	347
148	220.0	22.77	158	82	250.0	147.69	313
150	230.0	41.35	236	84	250.0	6.3	380
151	240.0	2.93	162	79	260.0	103.43	362
153	240.0	6.29	270	80	260.0	43.06	161
95	245.0	1.61	492	81	261.0	1.57	298
94	245.0	4.49	218	73	270.0	142.55	504
92	245.0	299.06	296	76	270.0	3.52	332
91	245.0	24.04	337	78	270.0	30.46	210
90	245.0	3.62	219	77	270.0	5.25	135
89	245.0	2200.87	583	75	270.0	25.03	544
88	245.0	1280.9	236	74	270.0	29.59	356
87	245.0	467.3	296	72	270.0	124.15	527
86	245.0	625.84	344	48	280.0	297.59	391
96	245.0	1.17	195	47	280.0	37.15	166
97	245.0	322.59	535	46	280.0	16.89	202
158	245.0	3.65	257	45	280.0	61.32	433
159	245.0	261.88	312	71	280.0	12.37	311
160	245.0	1.11	161	69	280.0	40.5	256
161	245.0	1723.11	283				

Table 6.1. Summary of relevant data obtained from the creep experiments: Test code, applied creep load F_{appl}, creep lifetime t_f, and the acoustic emission events $\mathcal{N}$.

$p(\boldsymbol{E}_{n,j+1}) = \omega_{n,j+1} Z_j^{-1}$, with the partition function Z_j given by Eq. 1.5, i.e., $Z_j = \Omega_0^{-1} \sum_{n=1}^{N} \omega_{n,j+1}$, and consequently the jump rate of the entire system at transition $j+1$ (Eq. 1.2) is given by $\omega_{j+1} = \Omega_0 Z_j = \sum_{n=1}^{N} \omega_{n,j+1}$.

In creep simulations, first the model is initially launched athermally up to the targeted uniaxial applied stress, σ_{appl}, which is a fraction of the athermal strength, i.e., $\sigma_{appl}/\sigma_{ath} < 1.0$. During this loading phase, some elements can be damaged (PDM) or eliminated (DFBM), possibly triggering avalanches. At the onset of the creep phase, we set $t = 0$. Later, during each transition $j+1$, just one element n is thermally activated. n is chosen at random, weighted by the local jump rates given by Eq. 6.6, i.e., $\left\{ n | \omega_{n,j+1} - u_{j+1} = 0 \right\}$, where u_{j+1} is a random number chosen from a uniform distribution, $0 < u_{j+1} < 1$. In a general case, when the local rates evolve with time during two successive transitions, $\omega_{n,j+1} = \omega_{n,j+1}(t')$, the waiting time Δt_{j+1} is obtained by solving $\int_0^{\Delta t_{j+1}} \sum_{n=1}^{N} \omega_{n,j+1}(t') \mathrm{d}t' = \Omega_0 \int_0^{\Delta t_{j+1}} Z_j(t') \mathrm{d}t' = -\ln u_{j+1}$. However, in

creep simulations, these rates are constant between 2 transitions, i.e., at any $j \in [0, \mathcal{N})$ time advances by an increment Δt_{j+1} following an exponential probability distribution (see Section 1.1.4) [84]:

$$\Delta t_{j+1} = -(\ln u_{j+1}) \langle \Delta t \rangle_{j+1} = -\frac{\ln u_{j+1}}{\Omega_0 Z_j}. \tag{6.7}$$

References

[1] Juan Carlos Verano-Espitia, Jérôme Weiss, David Amitrano, Tero Mäkinen, and Mikko Alava. Effect of quenched heterogeneity on creep lifetimes of disordered materials. *Phys. Rev. E*, 110:064133, Dec 2024. doi: 10.1103/PhysRevE.110.064133.

[2] Juan Carlos Verano-Espitia, Tero Mäkinen, Mikko J. Alava, and Jérôme Weiss. Creep failure in heterogeneous materials from the barrier landscape. *Phys. Rev. E*, 112:L063501, Dec 2025. doi: 10.1103/xbnt-6csz.

[3] Juan Carlos Verano-Espitia, Tero Mäkinen, Mikko J. Alava, and Jérôme Weiss. Early prediction of creep failure via bayesian inference of evolving barriers. *arXiv preprint*, 2026. doi: 10.48550/arXiv.2603.16419.

[4] Michael E Kassner. *Fundamentals of creep in metals and alloys*. Butterworth-Heinemann, Boston, 2015.

[5] Dominique François, André Pineau, and André Zaoui. *Mechanical behaviour of materials: Volume 1: Micro-and macroscopic constitutive behaviour*, volume 180. Springer Science & Business Media, Dordrecht, 2012.

[6] Zdenek P Bazant and Folker H Wittmann. *Creep and shrinkage in concrete structures*. Wiley New York, 1982.

[7] Luca Cipelletti, Kirsten Martens, and Laurence Ramos. Microscopic precursors of failure in soft matter. *Soft Matter*, 16(1):82–93, 2020. doi: 10.1039/C9SM01730E.

[8] Mathieu Leocmach, Christophe Perge, Thibaut Divoux, and Sébastien Manneville. Creep and fracture of a protein gel under stress. *Physical Review Letters*, 113(3):038303, 2014. doi: 10.1103/PhysRevLett.113.038303.

[9] Jari Rosti, Juha Koivisto, Lasse Laurson, and Mikko J Alava. Fluctuations and scaling in creep deformation. *Physical Review Letters*, 105(10):100601, 2010. doi: 10.1103/PhysRevLett.105.100601.

[10] Juha Koivisto, Markus Ovaska, Amandine Miksic, Lasse Laurson, and Mikko J Alava. Predicting sample lifetimes in creep fracture of heterogeneous materials. *Physical Review E*, 94(2):023002, 2016. doi: 10.1103/PhysRevE.94.023002.

[11] Tero Mäkinen, Juha Koivisto, Lasse Laurson, and Mikko J Alava. Scale-free features of temporal localization of deformation in late stages of creep failure. *Physical Review Materials*, 4(9):093606, 2020. doi: 10.1103/PhysRevMaterials.4.093606.

[12] Isaac Y Miranda-Valdez, Marie Sourroubille, Tero Mäkinen, Jesús G Puente-Córdova, Antti Puisto, Juha Koivisto, and Mikko J Alava. Fractional rheology of colloidal hydrogels with cellulose nanofibers. *Cellulose*, 31(3):1545–1558, 2024. doi: 10.1007/s10570-023-05694-8.

[13] Paul Duval, Maurine Montagnat, Fanny Grennerat, Jerome Weiss, Jacques Meyssonnier, and Armelle Philip. Creep and plasticity of glacier ice: a material science perspective. *Journal of Glaciology*, 56(200):1059–1068, 2010. doi: 10.3189/002214311796406185.

[14] N. Brantut, M.J. Heap, P.G. Meredith, and P. Baud. Time-dependent cracking and brittle creep in crustal rocks: A review. *Journal of Structural Geology*, 52:17–43, 2013. ISSN 0191-8141. doi: 10.1016/j.jsg.2013.03.007.

[15] J. C. Savage, J. L. Svarc, and Shui-Beih Yu. Postseismic relaxation and transient creep. *Journal of Geophysical Research: Solid Earth*, 110(B11), 2005. doi: 10.1029/2005JB003687.

[16] E.N.D.C. Andrade and F.T. Trouton. On the viscous flow in metals, and allied phenomena. *Proceedings of the Royal Society of London. Series A, Containing Papers of a Mathematical and Physical Character*, 84(567):1–12, 1910. doi: 10.1098/rspa.1910.0050.

[17] C. H. Scholz. Mechanism of creep in brittle rock. *Journal of Geophysical Research (1896-1977)*, 73(10):3295–3302, 1968. doi: 10.1029/JB073i010p03295.

[18] J.C. Jaeger and N.G.W. Cook. Fundamentals of rock mechanics. *Geological Magazine*, 117(4):401–401, 1979. doi: 10.1017/S001675680003274X.

[19] Chloé Braux, Antoine Bérut, and Loïc Vanel. Load-dependent power-law exponent in creep rupture of heterogeneous materials. *Phys. Rev. E*, 112: 065504, Dec 2025. doi: 10.1103/35tp-f364.

[20] AH Cottrell. The time laws of creep. *Journal of the Mechanics and Physics of Solids*, 1(1):53–63, 1952. doi: 10.1016/0022-5096(52)90006-9.

[21] Jérôme Weiss and David Amitrano. Logarithmic versus Andrade's transient creep: Role of elastic stress redistribution. *Physical Review Materials*, 7(3): 033601, 2023. doi: 10.1103/PhysRevMaterials.7.033601.

[22] FC Monkman and NJ Grant. *An empirical relationship between rupture life and minimum creep rate in creep rupture tests*, volume 56 of *in Proceedings of the ASTM presented at the 59th Annual Meeting of the ASTM*. ASTM Press, Philadelphia, 1957.

[23] C. H. Scholz. Experimental study of the fracturing process in brittle rock. *Journal of Geophysical Research (1896-1977)*, 73(4):1447–1454, 1968. doi: 10.1029/JB073i004p01447.

[24] J.-C. Anifrani, C. Le Floc'h, D. Sornette, and B. Souillard. Universal log-periodic correction to renormalization group scaling for rupture stress prediction from acoustic emissions. *Journal de Physique I France*, 5(6): 631–638, 1995. doi: 10.1051/jp1:1995156.

[25] Didier Sornette and Charles Sammis. Complex Critical Exponents from Renormalization Group Theory of Earthquakes: Implications for Earthquake Predictions. *Journal de Physique I*, 5(5):607–619, 1995. doi: 10.1051/jp1:1995154.

[26] Vincent Grenard, Thibaut Divoux, Nicolas Taberlet, and Sébastien Manneville. Timescales in creep and yielding of attractive gels. *Soft Matter*, 10: 1555–1571, 2014. doi: 10.1039/C3SM52548A.

[27] Johannes Weertman. Creep deformation of ice. *Annual Review of Earth and Planetary Sciences*, 11(Volume 11, 1983):215–240, 1983. ISSN 1545-4495. doi: 10.1146/annurev.ea.11.050183.001243.

[28] Stéphane Roux. Thermally activated breakdown in the fiber-bundle model. *Physical Review E*, 62:6164–6169, Nov 2000. doi: 10.1103/PhysRevE.62.6164.

[29] S. Ciliberto, A. Guarino, and R. Scorretti. The effect of disorder on the fracture nucleation process. *Physica D: Nonlinear Phenomena*, 158(1):83–104, 2001. ISSN 0167-2789. doi: 10.1016/S0167-2789(01)00306-2.

[30] Tero Mäkinen, Jérôme Weiss, David Amitrano, and Philippe Roux. History effects in the creep of a disordered brittle material. *Phys. Rev. Mater.*, 7:033602, Mar 2023. doi: 10.1103/PhysRevMaterials.7.033602.

[31] David Amitrano, Jean-Robert Grasso, and Didier Hantz. From diffuse to localised damage through elastic interaction. *Geophysical Research Letters*, 26(14):2109–2112, 1999. doi: 10.1029/1999GL900388.

[32] Didier Sornette. *Critical Phenomena in Natural Sciences: Chaos, Fractals, Selforganization and Disorder: Concepts and Tools*. Springer Berlin Heidelberg, 2006.

[33] H. Nechad, A. Helmstetter, R. El Guerjouma, and D. Sornette. Creep ruptures in heterogeneous materials. *Phys. Rev. Lett.*, 94:045501, Jan 2005. doi: 10.1103/PhysRevLett.94.045501.

[34] F. Omori. On the after-shocks of earthquakes. *The journal of the College of Science, Imperial University, Japan*, 7(2):111–200, 1895.

[35] H. Nechad, A. Helmstetter, R. El Guerjouma, and D. Sornette. Andrade and critical time-to-failure laws in fiber-matrix composites: Experiments and model. *Journal of the Mechanics and Physics of Solids*, 53(5):1099–1127, 2005. ISSN 0022-5096. doi: 10.1016/j.jmps.2004.12.001.

[36] A. Saichev and D. Sornette. Andrade, omori, and time-to-failure laws from thermal noise in material rupture. *Phys. Rev. E*, 71:016608, Jan 2005. doi: 10.1103/PhysRevE.71.016608.

[37] D. F. Castellanos and M. Zaiser. Avalanche behavior in creep failure of disordered materials. *Phys. Rev. Lett.*, 121:125501, Sep 2018. doi: 10.1103/PhysRevLett.121.125501.

[38] W. Weibull. *A statistical theory of the strength of materials*. Generalstabens Litografiska Anstalts Förlag, Stockholm, 1939.

[39] H.J. Herrmann and S. Roux. *Statistical models for the fracture of disordered media*. Random materials and processes. North-Holland, Amsterdam, 1990. ISBN 0-444-88551-X.

[40] Mikko J. Alava, Phani K. V. V. Nukala, and Stefano Zapperi. Statistical models of fracture. *Advances in Physics*, 55(3-4):349–476, 2006. doi: 10.1080/00018730300741518.

[41] Alex Hansen, Einar L Hinrichsen, and Stéphane Roux. Statistical models of breakdown and fracture. *Physica Scripta*, 1990(T33):20, jan 1990. doi: 10.1088/0031-8949/1990/T33/004.

[42] Paul Meakin. Models for material failure and deformation. *Science*, 252 (5003):226–234, 1991. doi: 10.1126/science.252.5003.226.

[43] Kiyoo Mogi. Study of elastic shocks caused by the fracture of heterogeneous materials and its relations to earthquake phenomena. *Bull. Earthquake Res. Int. Univ. Tokyo*, 40:125–173, 1962. URL https://cir.nii.ac.jp/crid/1573950399437050880.

[44] Kiyoo Mogi. Earthquake prediction research in japan. *Journal of Physics of the Earth*, 43(5):533–561, 1995. doi: 10.4294/jpe1952.43.533.

[45] Didier Sornette. Predictability of catastrophic events: Material rupture, earthquakes, turbulence, financial crashes, and human birth. *Proceedings of the National Academy of Sciences*, 99(suppl_1):2522–2529, 2002. doi: 10.1073/pnas.022581999.

[46] Jérémie Vasseur, Fabian B. Wadsworth, Yan Lavallée, Andrew F. Bell, Ian G. Main, and Donald B. Dingwell. Heterogeneity: The key to failure forecasting. *Scientific Reports*, 5:13259, Aug 2015. doi: 10.1038/srep13259.

[47] S. N. Zhurkov. Kinetic concept of the strength of solids. *International Journal of Fracture Mechanics*, 1:311–323, Dec 1965. doi: 10.1007/BF03545562.

[48] Véronique Dansereau, Vincent Démery, Estelle Berthier, Jérôme Weiss, and Laurent Ponson. Collective damage growth controls fault orientation in quasibrittle compressive failure. *Phys. Rev. Lett.*, 122:085501, Feb 2019. doi: 10.1103/PhysRevLett.122.085501.

[49] Srutarshi Pradhan, Alex Hansen, and Bikas K. Chakrabarti. Failure processes in elastic fiber bundles. *Reviews of Modern Physics*, 82:499–555, Mar 2010. doi: 10.1103/RevModPhys.82.499.

[50] A.A. Griffith. Vi. the phenomena of rupture and flow in solids. *Philosophical Transactions of the Royal Society of London, Series A: Containing Papers of a Mathematical or Physical Character*, 221(582-593):163–198, 01 1921. ISSN 0264-3952. doi: 10.1098/rsta.1921.0006.

[51] Barry Kean Atkinson. Subcritical crack growth in geological materials. *Journal of Geophysical Research: Solid Earth*, 89(B6):4077–4114, 1984. doi: 10.1029/JB089iB06p04077.

[52] A. Guarino, S. Ciliberto, A. Garcimartın, M. Zei, and R. Scorretti. Failure time and critical behaviour of fracture precursors in heterogeneous materials. *The European Physical Journal B - Condensed Matter and Complex Systems*, 26(2):141–151, 2002. ISSN 0167-2789. doi: 10.1140/epjb/e20020075.

[53] George H. Vineyard. Frequency factors and isotope effects in solid state rate processes. *Journal of Physics and Chemistry of Solids*, 3(1):121–127, 1957. ISSN 0022-3697. doi: 10.1016/0022-3697(57)90059-8.

[54] MJ Heap, P Baud, and PG Meredith. Influence of temperature on brittle creep in sandstones. *Geophysical Research Letters*, 36(19), 2009. doi: 10.1029/2009GL039373.

[55] Tao Xu, Chun-an Tang, Jian Zhao, Lianchong Li, and Michael J Heap. Modelling the time-dependent rheological behaviour of heterogeneous brittle rocks. *Geophysical Journal International*, 189(3):1781–1796, 2012. doi: 10.1111/j.1365-246X.2012.05460.x.

[56] MJ Heap, Patrick Baud, PG Meredith, Sergio Vinciguerra, AF Bell, and IG Main. Brittle creep in basalt and its application to time-dependent volcano deformation. *Earth and Planetary Science Letters*, 307(1-2):71–82, 2011. doi: 10.1016/j.epsl.2011.04.035.

[57] H Daniel Wagner, Peter Schwartz, and S Leigh Phoenix. Lifetime statistics for single Kevlar 49 filaments in creep-rupture. *Journal of Materials Science*, 21(6):1868–1878, 1986. doi: 10.1007/BF00547921.

[58] Pappu Murthy, John Thesken, S Phoenix, and Lorie Grimes-Ledesma. Stress rupture life reliability measures for composite overwrapped pressure vessels. In *48th AIAA/ASME/ASCE/AHS/ASC Structures, Structural Dynamics, and Materials Conference*, page 2150. AIAA Press, Honolulu, Hawaii, 2007.

[59] Ioannis Boumakis, Krešimir Ninčević, Jan Vorel, and Roman Wan-Wendner. Creep rate based time-to-failure prediction of adhesive anchor systems under sustained load. *Composites Part B: Engineering*, 178:107389, 2019. doi: 10.1016/j.compositesb.2019.107389.

[60] Yves Pomeau. Brisure spontanée de cristaux bidimensionnels courbés. *Comptes rendus de l'Académie des Sciences Paris*, 314(II):553–556, 1992.

[61] Yves Pomeau. Fundamental problems in brittle fracture: unstable cracks and delayed breaking. *Comptes Rendus Mécanique*, 330(4):249–257, 2002. doi: 10.1016/S1631-0721(02)01456-0.

[62] H. Eyring. Viscosity, plasticity, and diffusion as examples of absolute reaction rates. *The Journal of chemical physics*, 4(4):283–291, 1936. doi: 10.1063/1.1749836.

[63] Craig E. Maloney and Daniel J. Lacks. Energy barrier scalings in driven systems. *Physical Review E*, 73:061106, Jun 2006. doi: 10.1103/PhysRevE.73.061106.

[64] Peter Kratzer. Monte Carlo and kinetic Monte Carlo methods–A tutorial. In J. Grotendorst, N. Attig, S. Blügel, and D. Marx, editors, *Multiscale Simulation Methods in Molecular Sciences*, volume 42 of *NIC Series*, pages 51–76. Institute for Advanced Simulation, Forschungszentrum Jülich, 2009.

[65] Kristen A. Fichthorn and W. H. Weinberg. Theoretical foundations of dynamical Monte Carlo simulations. *The Journal of Chemical Physics*, 95(2):1090–1096, 07 1991. ISSN 0021-9606. doi: 10.1063/1.461138.

[66] R.H. Walpole, R.E.and Myers, S.L. Myers, and K. Ye. *Probability & Statistics for Engineers & Scientists*. Pearson Education Inc, New Jersey, 9 edition, 2007.

[67] D. M. Cruden. A theory of brittle creep in rock under uniaxial compression. *Journal of Geophysical Research (1896-1977)*, 75(17):3431–3442, 1970. doi: 10.1029/JB075i017p03431.

[68] R. K. Pathria and Paul D. Beale. *Statistical Mechanics*. Elsevier, Amsterdam, 3 edition, 2011.

[69] James P. Sethna. *Statistical Mechanics: Entropy, Order Parameters, and Complexity*. Oxford Master Series in Physics, Oxford, 2 edition, 2021.

[70] C. E. Shannon. A mathematical theory of communication. *The Bell System Technical Journal*, 27(4):623–656, 1948. doi: 10.1002/j.1538-7305.1948.tb00917.x.

[71] N. Yoshioka, F. Kun, and N. Ito. Time evolution of damage in thermally induced creep rupture. *Europhysics Letters*, 97(2):26006, jan 2012. doi: 10.1209/0295-5075/97/26006.

[72] Steven R Pride and Renaud Toussaint. Thermodynamics of fiber bundles. *Physica A: Statistical Mechanics and its Applications*, 312(1):159–171, 2002. ISSN 0378-4371. doi: 10.1016/S0378-4371(02)00816-6.

[73] David Amitrano. *Emission acoustique des roches et endommagement: Approches expérimentale et numérique, Application a la sismicité minière*. Theses, Université Joseph-Fourier - Grenoble I, January 1999. URL `https://theses.hal.science/tel-00173626`.

[74] David Amitrano and Agnès Helmstetter. Brittle creep, damage, and time to failure in rocks. *Journal of Geophysical Research: Solid Earth*, 111(B11), 2006. doi: 10.1029/2005JB004252.

[75] L Girard, D Amitrano, and J Weiss. Failure as a critical phenomenon in a progressive damage model. *Journal of Statistical Mechanics: Theory and Experiment*, 2010(01):P01013, jan 2010. doi: 10.1088/1742-5468/2010/01/P01013.

[76] Lucas Girard, Jérôme Weiss, and David Amitrano. Damage-cluster distributions and size effect on strength in compressive failure. *Physical Review Letters*, 108:225502, May 2012. doi: 10.1103/PhysRevLett.108.225502.

[77] Mervyn S. Paterson and Teng fong Wong. *Experimental Rock Deformation - The Brittle Field*. Springer Berlin, Heidelberg, 2 edition, 2005.

[78] David Amitrano. Émergence de la complexité dans un modèle simple de comportement mécanique des roches. *Comptes Rendus Geoscience*, 336(6): 505–512, 2004. ISSN 1631-0713. doi: 10.1016/j.crte.2003.11.023.

[79] Chi-Cong Vu, David Amitrano, Olivier Plé, and Jérôme Weiss. Compressive failure as a critical transition: Experimental evidence and mapping onto the universality class of depinning. *Physical Review Letters*, 122(1):015502, 2019. doi: 10.1103/PhysRevLett.122.015502.

[80] D. Lockner, JD Byerlee, V Kuksenko, A Ponomarev, and A Sidorin. Quasi-static fault growth and shear fracture energy in granite. *Nature*, 350(6313): 39–42, 1991. doi: 10.1038/350039a0.

[81] D. Lockner. The role of acoustic emission in the study of rock fracture. *International Journal of Rock Mechanics and Mining Sciences & Geomechanics Abstracts*, 30(7):883–899, 1993. doi: 10.1016/0148-9062(93)90041-B.

[82] Nicolas Brantut, Alexandre Schubnel, and Yves Guéguen. Damage and rupture dynamics at the brittle-ductile transition: The case of gypsum. *Journal of Geophysical Research: Solid Earth*, 116:B01404, 2011. doi: 10.1029/2010JB007675.

[83] David Amitrano. Brittle-ductile transition and associated seismicity: Experimental and numerical studies and relationship with the b value. *Journal of Geophysical Research: Solid Earth*, 108:2044, 2003. doi: 10.1029/2001JB000680.

[84] A.B. Bortz, M.H. Kalos, and J.L. Lebowitz. A new algorithm for Monte Carlo simulation of Ising spin systems. *Journal of Computational Physics*, 17(1): 10–18, 1975. ISSN 0021-9991. doi: 10.1016/0021-9991(75)90060-1.

[85] Kim Sneppen. Extremal dynamics and punctuated co-evolution. *Physica A: Statistical Mechanics and its Applications*, 221(1):168–179, 1995. ISSN 0378-4371. doi: 10.1016/0378-4371(95)00237-2. Proceedings of the Second IUPAP Topical Conference and the Third Taipei International Symposium on Statistical Physics.

[86] S. L. Miller, W. M. Miller, and P. J. McWhorter. Extremal dynamics: A unifying physical explanation of fractals, 1/f noise, and activated processes. *Journal of Applied Physics*, 73(6):2617–2628, 03 1993. doi: 10.1063/1.353079.

[87] Daniel J Korchinski, Dor Shohat, Yoav Lahini, and Matthieu Wyart. Thermal avalanches drive logarithmic creep in disordered media. *Physical Review X*, 15(3):031024, 2025. doi: 10.1103/x7rr-vxnr.

[88] H Daniel Wagner, S Leigh Phoenix, and Peter Schwartz. A study of statistical variability in the strength of single aramid filaments. *Journal of Composite Materials*, 18(4):312–338, 1984. doi: 10.1177/002199838401800402.

[89] A. De S. Jayatilaka and K. Trustrum. Statistical approach to brittle fracture. *Journal of Materials Science*, 12(7):1426–1430, 1977. ISSN 1573-4803. doi: 10.1007/BF00540858.

[90] K. Trustrum and A. De S. Jayatilaka. Applicability of Weibull analysis for brittle materials. *Journal of Materials Science*, 18(9):2765–2770, 1983. ISSN 1573-4803. doi: 10.1007/BF00547593.

[91] J. Andersons, R. Joffe, M. Hojo, and S. Ochiai. Glass fibre strength distribution determined by common experimental methods. *Composites Science and Technology*, 62(1):131–145, 2002. ISSN 0266-3538. doi: 10.1016/S0266-3538(01)00182-8.

[92] I. C. van den Born, A. Santen, H. D. Hoekstra, and J. Th. M. De Hosson. Mechanical strength of highly porous ceramics. *Physical Review B*, 43: 3794–3796, Feb 1991. doi: 10.1103/PhysRevB.43.3794.

[93] M. El Asloun, J. B. Donnet, G. Guilpain, M. Nardin, and J. Schultz. On the estimation of the tensile strength of carbon fibres at short lengths. *Journal of Materials Science*, 24(10):3504–3510, 1989. doi: 10.1007/BF02385732.

[94] D. S. Farquhar, F. M. Mutrelle, S. L. Phoenix, and R. L. Smith. Lifetime statistics for single graphite fibres in creep rupture. *Journal of Materials Science*, 24(6):2151–2164, 1989. doi: 10.1007/BF02385436.

[95] Mikko Alava and Kaarlo Niskanen. The physics of paper. *Reports on Progress in Physics*, 69(3):669, 2006. doi: 10.1088/0034-4885/69/3/R03.

[96] Chi Cong Vu. *Statistical size effects on compressive strength of concrete*. Theses, Université Grenoble Alpes, October 2018. URL `https://theses.hal.science/tel-04114469`.

[97] S. Redner. Random multiplicative processes: An elementary tutorial. *American Journal of Physics*, 58(3):267–273, 03 1990. doi: 10.1119/1.16497.

[98] Didier Sornette and Rama Cont. Convergent multiplicative processes repelled from zero: Power laws and truncated power laws. *Journal de Physique I*, 7(3):431–444, 1997. doi: 10.1051/jp1:1997169.

[99] David Marsan, Harry Stern, Ron Lindsay, and Jérôme Weiss. Scale dependence and localization of the deformation of Arctic sea ice. *Physical Review Letters*, 93. doi: 10.1103/PhysRevLett.93.178501.

[100] Tero Mäkinen, Alisa Halonen, Juha Koivisto, and Mikko J Alava. Wood compression in four-dimensional in situ tomography. *Physical Review Materials*, 6(7):L070601, 2022. doi: 10.1103/PhysRevMaterials.6.L070601.

[101] Ao Tang, Haiting Liu, Guisen Liu, Yong Zhong, Li Wang, Qi Lu, Jeff Wang, and Yao Shen. Lognormal distribution of local strain: a universal law of plastic deformation in material. *Physical Review Letters*, 124(15):155501, 2020. doi: 10.1103/PhysRevLett.124.155501.

[102] Jingwei Chen and Alexander M Korsunsky. Why is local stress statistics normal, and strain lognormal? *Materials & Design*, 198:109319, 2021. doi: 10.1016/j.matdes.2020.109319.

[103] Oriol Abril-Pla, Virgile Andreani, Colin Carroll, Larry Dong, Christopher J. Fonnesbeck, Maxim Kochurov, Ravin Kumar, Junpeng Lao, Christian C. Luhmann, Osvaldo A. Martin, Michael Osthege, Ricardo Vieira, Thomas Wiecki, and Robert Zinkov. PyMC: A modern and comprehensive probabilistic programming framework in Python. *PeerJ Computer Science*, 9(e1516), 2023. doi: 10.7717/peerj-cs.1516.

[104] Matthew D. Hoffman and Andrew Gelman. The No-U-Turn Sampler: Adaptively setting path lengths in hamiltonian monte carlo. *Journal of Machine Learning Research*, 15(47):1593–1623, 2014. URL `http://jmlr.org/papers/v15/hoffman14a.html`.

[105] Tero Mäkinen, Lumi Tuokkola, Joonas Lahikainen, Ivan V Lomakin, Juha Koivisto, and Mikko J Alava. Crack propagation by activated avalanches during creep and fatigue from elastic interface theory. *Physical Review Letters*, 134(9):098202, 2025. doi: 10.1103/PhysRevLett.134.098202.

[106] Hans Hersbach. Decomposition of the continuous ranked probability score for ensemble prediction systems. *Weather and Forecasting*, 15(5):559 – 570, 2000. doi: 10.1175/1520-0434(2000)015<0559:DOTCRP>2.0.CO;2.

[107] Qinghua Lei and Didier Sornette. A stochastic dynamical model of slope creep and failure. *Geophysical Research Letters*, 50(11):e2022GL102587, 2023. doi: 10.1029/2022GL102587.

[108] Qinghua Lei and Didier Sornette. Log-periodic power law singularities in landslide dynamics: Statistical evidence from 52 crises. *Geophysical Research Letters*, 52(15):e2025GL116379, 2025. doi: 10.1029/2025GL116379.

[109] Emanuele Intrieri, Tommaso Carlà, and Giovanni Gigli. Forecasting the time of failure of landslides at slope-scale: A literature review. *Earth-science reviews*, 193:333–349, 2019. doi: 10.1016/j.earscirev.2019.03.019.

[110] Qinghua Lei and Didier Sornette. Oscillatory finite-time singularities in rockbursts. *International Journal of Rock Mechanics and Mining Sciences*, 192:106156, 2025. doi: 10.1016/j.ijrmms.2025.106156.

[111] GB Crosta and F Agliardi. Failure forecast for large rock slides by surface displacement measurements. *Canadian Geotechnical Journal*, 40(1):176–191, 2003. doi: 10.1139/t02-085.

[112] Jerome Faillettaz, Martin Funk, and Didier Sornette. Icequakes coupled with surface displacements for predicting glacier break-off. *Journal of Glaciology*, 57(203):453–460, 2011. doi: 10.3189/002214311796905668.

[113] Jérome Faillettaz, Martin Funk, and Christian Vincent. Avalanching glacier instabilities: Review on processes and early warning perspectives. *Reviews of Geophysics*, 53(2):203–224, 2015. doi: 10.1002/2014RG000466.

[114] Jérome Faillettaz, Martin Funk, and Marco Vagliasindi. Time forecast of a break-off event from a hanging glacier. *The Cryosphere*, 10(3):1191–1200, 2016. doi: 10.5194/tc-10-1191-2016.

[115] Qinghua Lei and Didier Sornette. Log-periodic precursors to volcanic eruptions: Evidence from 34 events. *arXiv preprint*, 2025. doi: 10.48550/arXiv.2502.21277.

[116] Qinghua Lei and Didier Sornette. Unified failure model for landslides, rockbursts, glaciers, and volcanoes. *Communications Earth & Environment*, 6(1):390, 2025. doi: 10.1038/s43247-025-02369-z.

[117] J Rosti, J Koivisto, and M J Alava. Statistics of acoustic emission in paper fracture: precursors and criticality. *Journal of Statistical Mechanics: Theory and Experiment*, 2010(02):P02016, feb 2010. doi: 10.1088/1742-5468/2010/02/P02016.

[118] Leevi Viitanen, Markus Ovaska, Sumit Kumar Ram, Mikko J. Alava, and Pasi Karppinen. Predicting creep failure from cracks in a heterogeneous material using acoustic emission and speckle imaging. *Phys. Rev. Appl.*, 11:024014, Feb 2019. doi: 10.1103/PhysRevApplied.11.024014.

[119] Jacob Fraden. *Handbook of Modern Sensors*. Springer New York, NY, 4 edition, 2010.

[120] Tero Mäkinen. *Collective phenomena in deformation*. PhD thesis, Aalto University, Finland, 2020.

[121] Sanja Janićević, Lasse Laurson, Knut Jørgen Måløy, Stéphane Santucci, and Mikko J Alava. Interevent correlations from avalanches hiding below the detection threshold. *Physical Review Letters*, 117(23):230601, 2016. doi: 10.1103/PhysRevLett.117.230601.

Key terms of the doctoral thesis

Key term: creep

- Definition: time-dependent deformation of a material under a constant load
    - Explanation: A mechanical response shown by some materials, engineering structures or geophysical objects when subjected to a constant load.

Keskeinen käsite: viruminen

- Määritelmä: materiaalin aikariippuva muodonmuutos vakiokuormituksen alaisena
    - Selite: Joidenkin materiaalien, rakenteiden tai geofysikaalisten kohteiden mekaaninen vaste vakiokuormituksen alaisena.

Key term: heterogeneous material

- Definition: material whose local spatial properties vary
    - Explanation: Materials which exhibit variation of physical properties, such as the elastic properties or the electric response. Also known as disordered materials.

Keskeinen käsite: heterogeeninen materiaali

- Määritelmä: materiaali, jonka paikalliset ominaisuudet vaihtelevat
    - Selite: Materiaaleja, joiden fysikaaliset ominaisuudet, kuten elastiset ominaisuudet tai sähköinen vaste, vaihtelevat paikallisesti. Tunnetaan myös nimellä epäjärjestyneet materiaalit.

Aalto University

Université Grenoble Alpes

Business, Economy
Art, Design, Architecture
Science, Technology
Crossover
Doctoral Theses

Aalto DT 151/2026

ISBN 978-952-64-3231-1
ISBN 978-952-64-3230-4 (pdf)

Aalto University
School of Science
Department of Applied Physics
Complex Systems and Materials
aalto.fi